This is Chapter 8 "Fibre optic monitoring section: Data evaluation" including the related Appendix D "Fibre optic monitoring section: Data evaluation" from my PhD thesis

Kluckner, A. 2023. Tunnelling at greater depths: Study on the ground and system behaviour when passing a stiff rock block in a weak zone. PhD thesis. Graz University of Technology, Graz, Austria.

The full thesis can be downloaded from the TU Graz repository: LINK

If you have any questions or remarks, you can contact me on

ResearchGate: LINK

or on

LinkedIn: LINK.

Enjoy reading.

Best regards, Alexander Kluckner



Dipl.-Ing. Alexander Kluckner, BSc

Tunnelling at greater depths: Study on the ground and system behaviour when passing a stiff rock block in a weak zone

DOCTORAL THESIS

to achieve the university degree of Doktor der technischen Wissenschaften

submitted to

Graz University of Technology

Reviewers

Em.Univ.-Prof. Dipl.-Ing. Dr.mont. Wulf Schubert Faculty of Civil Engineering Sciences Graz University of Technology, Graz, Austria

Univ.-Prof. Dr. Nobuharu Isago Faculty of Urban Environmental Sciences Tokyo Metropolitan University, Tokyo, Japan

Contents

Li	st of	Figures	xxi
Li	st of	Tables	xxix
Li	st of	Acronyms, Symbols, and Notations	xxxv
1	Intr	roduction	1
	1.1	Research motivation	. 1
	1.2	Research questions	. 4
	1.3	Methodology	. 5
	1.4	Thesis structure and objectives	. 6
	1.5	Research limitations	. 7
2	Abo	out fault zones and block-in-matrix rocks	9
	2.1	Brittle fault zones	. 12
	2.2	Block-in-matrix rocks	. 14
3	Son	ne properties of rocks and rock masses	19
	3.1	Geometric properties of bimrock blocks	. 19
		3.1.1 Block shape	. 19
		3.1.2 Block location and orientation	. 21
		3.1.3 Block size	. 21
	3.2	Mechanical properties of rocks and rock masses	. 22
		3.2.1 Shear strength of the matrix material	. 22
		3.2.2 Uniaxial compressive strength of the matrix material	. 28
		3.2.3 Shear strength of the block material	. 28
		3.2.4 Uniaxial compressive strength of the block material $\ \ldots \ \ldots \ \ldots$. 28
		3.2.5 Tensile strength	. 30
		3.2.6 Dilation angle	. 32
		3.2.7 Poisson's ratio	. 33
		3.2.8 Density	. 36
		3.2.9 Young's modulus	. 36
		3.2.10 Block-matrix contacts	. 40
4	Son	ne characteristics of shotcrete	45
	4.1	Hardening of concrete	. 47
	4.2	Origin of strength and stiffness growth	. 47
	4.3	A note on the behaviour under pressure	. 48
	4.4	About strain in shotcreted tunnel linings	. 49
	15	Postroints	50

CONTENTS

	4.6	Strain	n components	51
		4.6.1	Elastic (instantaneous) strain	52
		4.6.2	Thermal elastic (instantaneous) strain	52
		4.6.3	Shrinkage (delayed) strain	54
		4.6.4	Creep (delayed) strain	57
		4.6.5	Plastic (instantaneous) strain	60
		4.6.6	Irrecoverable strain due to ageing	62
	4.7	Peak	strain	62
	4.8	Shotc	rete strength	63
	4.9	Shotc	rete deformability	66
		4.9.1	Poisson's ratio	67
		4.9.2	Empirical approximation	67
5	The	rmo-cl	nemo-mechanical shotcrete model	69
	5.1	Displa	acement and strain field	70
	5.2	Shote	rete model	71
		5.2.1	Chemo-thermal coupling	73
		5.2.2	Thermo-mechanical coupling	74
		5.2.3	Chemo-mechanical coupling	74
6	Stiff	f block	next to excavation (2D): Parametric study	81
	6.1		erical model setup	82
		6.1.1	Modelling of system features	82
		6.1.2	Modelling of material behaviour	84
		6.1.3	Mesh	86
		6.1.4	Model size	87
		6.1.5	Boundary conditions and initial state	87
		6.1.6	Solve criterion and damping	87
		6.1.7	Excavation method	88
	6.2	Nume	erical input parameters	89
		6.2.1	Tunnel shape and size	90
		6.2.2	Primary stress state	90
		6.2.3	Block shape	90
		6.2.4	Block location and orientation	90
		6.2.5	Distance of the block from the tunnel and block size	94
		6.2.6	Internal angle of friction of the matrix material	94
		6.2.7	Internal angle of friction of the block material	94
		6.2.8	Cohesion of the matrix material	95
		6.2.9	Uniaxial compressive strength of the matrix material	96
		6.2.10	Uniaxial compressive strength of the block material	97
		6.2.11	Cohesion of the block material	98
		6.2.12	Tensile strength	98
		6.2.13	Dilation angle	100
		6.2.14	Poisson's ratio	100
		6.2.15	Density	100
		6.2.16	Young's modulus	100
		6 2 17	Interface properties	101

CONTENTS xv

	6.3	Evalu	ation approach	103
		6.3.1	Angular deviation of in-plane tunnel displacement vectors	105
		6.3.2	Total in-plane tunnel displacements	107
		6.3.3	Shear strain increment along tunnel periphery	108
		6.3.4	Maximum in-plane block-matrix interface slip, and other interface related	
			variables	109
		6.3.5	Block bending	109
		6.3.6	Horizontal evaluation plane	
		6.3.7	Path of highest secondary in-plane major principal stresses	
		6.3.8	Parameter development with ongoing relaxation	
		6.3.9	Zone-by-zone comparison of different cases	
			Orientation of stresses along block periphery	
			Spalling limit and damage threshold	
			Work	
	6.4		ts: Summary	
	0.1	6.4.1	In-plane block-matrix interface slip	
		6.4.2	Shear strain increment	
		6.4.3	Block deformation	
		6.4.4	Block displacement	
		6.4.5	Path of the highest secondary in-plane major principal stresses	
		6.4.6	Shear strain increment along tunnel periphery	
		6.4.7	Displacement of the tunnel periphery	
		6.4.8	Yielded zones	
		6.4.9	Block failure	
			In-plane stresses	
			Orientation of in-plane stresses	
			Elastic work	
	6.5		pretation and discussion	
	0.0	6.5.1	The block-matrix interface rules	
		0.0.1		
		6.5.2	•	
		6.5.3	Small block distance: hazardous	
		6.5.4	Identification on site? It depends	
		6.5.5	Underestimation of the situation	
		6.5.6	About installing support	157
		6.5.7	On dynamic effects	
		6.5.8	Most probable scenario	158
7	Stiff	f block	next to excavation (3D): Supplementary study	159
	7.1		erical model setup	159
		7.1.1	Modelling of system features	159
		7.1.2	Mesh	160
		7.1.3	Model size	160
		7.1.4	Boundary conditions and initial state	
		7.1.5	Construction sequence and excavation method	
	7.2		erical input parameters	161
		7.2.1	Block shape	161
		7.2.2	Block location	
		_		

CONTENTS xvi

		7.2.3 Block distance from the tunnel	61
	7.3	Evaluation approach	61
	7.4	Results	62
	7.5	Interpretation and discussion	67
8	Fibi	re optic monitoring section: Data evaluation 1	69
	8.1	Distributed fibre optic sensing	
	8.2	Geological and hydrogeological conditions	
	8.3	Rock mass types	
	8.4	Primary stress state	
	0.1	8.4.1 General	
		8.4.2 Primary stress at the analysed section	
	8.5	Tunnelling method	
	0.0	8.5.1 Excavation sequence	
		8.5.2 Support	
		8.5.3 Work steps	
	0.6	•	
	8.6	Position of monitoring devices	
	8.7	Observed system behaviour: Geodetic measurements	
		8.7.1 Time-dependent displacements	
		8.7.2 Out-of-plane displacements	
		8.7.3 In-plane displacements	
	8.8	Observed system behaviour: DFOS	
		8.8.1 Strain in the circumferential and longitudinal direction	
		8.8.2 Evolution of strain with time	
		8.8.3 Strain rate	
	8.9	Observed system behaviour: Temperature	96
9	Fib	re optic monitoring section: Calibration case (3D)	01
	9.1	Limitations	02
		9.1.1 Time-dependent rock deformation	02
		9.1.2 Swelling	02
		9.1.3 Porewater pressure	02
	9.2	DFOS section: Strain components utilising a micromechanical model 2	03
		9.2.1 Neglecting thermal strain	04
		9.2.2 Neglecting shrinkage strain	05
	9.3	Burgers model	05
		9.3.1 Basic rheological models	207
		9.3.2 Combined rheological models	207
	9.4	•	10
		9.4.1 Modelling of system features	12
		9.4.2 Modelling of material behaviour	
		~	14
			15
			15
			15
		r o	16
		9.4.8 Creep time step	

CONTENTS xvii

	9.5	Numerical input parameters	20
		9.5.1 Tunnel shape and size	20
		9.5.2 Primary stress state	20
		9.5.3 Rock mass	20
		9.5.4 Backfill	25
		9.5.5 Shotcrete lining	25
		9.5.6 Rock bolts	33
	9.6	Evaluation approach	36
	9.7	Results	36
	9.8	Interpretation and discussion	40
10		,	43
	10.1	Limitations	
	10.2	Geological and hydrogeological conditions	
	10.3	Rock mass types	
	10.4	Primary stress state	
		10.4.1 General	
		10.4.2 Primary stress at the analysed section	
	10.5	Tunnelling method	
	10.6	Position of monitoring devices	
	10.7	Observed system behaviour: Geodetic measurements	
	10.8	Numerical model setup	
		10.8.1 Modelling of system features	
		10.8.2 Modelling of material behaviour	
		10.8.3 Mesh	
		10.8.4 Model size	
		10.8.5 Boundary conditions and initial state	
		10.8.6 Construction sequence	
	10.9	Numerical input parameters	
		10.9.1 Tunnel shape and size	
		v	60
			61
		9	67
			68
		**	68
			69
	10.12	Interpretation and discussion	71
11	Disc	ussion 2'	77
	11.1		77
	11.2	·	78
	11.3		79
	11.4		79
	11.5		81
	11.6		81
			81
		11.6.2 Tunnel support	
		* *	

CONTENTS xviii

	11.6.3 Tunnelling sequence	284
12 Con	clusion	285
Bibliog	raphy	287
Appen	dix A: Equations	317
A.1	Stress invariants	317
A.2	Strain invariants	317
A.3	Mohr-Coulomb failure criterion	318
A.4	Size of the yield zone in a homogeneous, isotropic rock mass	318
A.5	Elastic secondary tangential in-plane stresses around a circular opening in a	
	homogenous, isotropic medium	319
A.6	Elastic secondary tangential in-plane stresses around an elliptic opening in a	
	homogenous, isotropic medium	320
Appen	dix B: Some mechanical properties of rocks	321
B.1	Tensile strength	321
	B.1.1 Johnston (1985)	
	B.1.2 Kluckner (2012)	
	B.1.3 Rostami et al. (2016)	
B.2	Dilation angle	
	B.2.1 Terminology	
	B.2.2 Kluckner (2012)	
B.3	Poisson's ratio	326
B.4	Young's modulus	326
A	dia C. Stiff black mark to accounting (2D). Dominator at also	220
C.1	dix C: Stiff block next to excavation (2D): Parametric study Numerical model setup	329
0.1	C.1.1 Evaluation of constitutive model for matrix material	
	C.1.2 Evaluation of minimum in-plane model size	
	C.1.3 Evaluation of solve limit	337
	C.1.4 Evaluation of excavation method	342
C.2	Numerical input parameters	343
0.2	C.2.1 Mechanical properties of model features	343
	C.2.2 Evaluation of interface stiffnesses	350
C.3	Results: Details	355
	C.3.1 In-plane block-matrix interface slip	355
	C.3.2 Shear strain increment	370
	C.3.3 Block deformation: Bending	385
	C.3.4 Block deformation: Change in the block height	391
	C.3.5 Block deformation: Change in the block width	393
	C.3.6 Block displacement	396
	C.3.7 Path of the largest secondary in-plane major principal stresses	400
	C.3.8 Shear strain increment along tunnel periphery	405
	C.3.9 Displacement of the tunnel periphery	411
	C.3.10 Yielded zones	425
	C.3.11 Block failure	438

CONTENTS	xix
C.3.12 In-plane stresses	457
C.3.13 Orientation of in-plane stresses	472

C.3.14 Elastic work	485
Appendix D: Fibre optic monitoring section: Data evaluation	497

Chapter 8

Fibre optic monitoring section: Data evaluation

The Semmering Base Tunnel (SBT), a twin-tube single-track railway tunnel in Austria with a length of approx. 27 km is currently under construction. The geological and geotechnical conditions are challenging (cf., e.g., [171]). From chainage 1438.2 m to chainage 1440.2 m of track 1 of the tunnel Gloggnitz (construction lot SBT 1.1), the outer lining made of shotcrete is equipped with a distributed fibre optic sensing (DFOS) system. It allows for a direct, continuous, and autonomous monitoring of strain in the shotcrete lining along the DFOS cables. In this thesis, this tunnel section is termed DFOS section. Captions of some figures and tables below cite the abbreviation $SBT1.1 \mid Gloggnitz$ referring to track 1.

[416] describe the instrumentation at the construction site in detail. Section 8.1 in this thesis briefly describes the main specifications of the installed DFOS system. Section 8.2 lists relevant information about the geological and hydrogeological conditions at the DFOS section and tunnel sections behind and ahead. Relevant rock mass types are cited in Section 8.3 (p. 172). It follows a summary of the tunnelling method (Section 8.5 on p. 175), a description of the positioning of DFOS cables and other monitoring devices (Section 8.6 on p. 180), and a brief overview of the system behaviour observed with conventional geodetic measurements (Section 8.7 on p. 181). Section 8.8 (p. 186) outlines observed characteristics of the strain of the shotcrete lining monitored with the DFOS system.

8.1 Distributed fibre optic sensing

The DFOS interrogation unit makes use of the Rayleigh backscatter. If a light pulse is sent through the fibre core, it scatters at inhomogeneities of the glass. Such inhomogeneities can exist naturally (i.e., prior to installation) or form as the fibre is strained either mechanically or because of temperature changes. Chemical changes in the surrounding medium can also alter the glass. Anyway, referring to a reference measurement at the beginning of the monitoring period, the system can determine the relative frequency shift in the locally reflected frequency spectrum. The frequency shift is directly proportional to the change in strain or temperature. Using the signal runtime, it is possible to locate the particular point along the fibre core where this change occurred. Note that only about 85% of the natural attenuations in optical fibres are caused by Rayleigh scattering ([422] in [266, p. 2]). For more details about the working principles of DFOS systems, refer, e.g., to [148]. [266, p. 2]

Protective layers, which allow for an unbiased strain transfer from the outer sheath to the sensitive fibre core, surround the latter. The outer sheath features a structured surface to guarantee a proper bond with the shotcrete. The fibre core and all protective layers make up the DFOS cable approx. 7 mm in diameter. [266, p. 3, 8]

The strain values obtained are temperature compensated. This means that effects of temperature changes in the fibre core are eliminated from recordings to provide strain values that result only because of the straining of the shotcrete lining ([266, p. 4]). The latter, however, can be of mechanical origin (i.e., because of rock mass deformation) but also because of temperature changes in the shotcrete lining, and because of creep, shrinkage, and swelling of the shotcrete material. The fibre optic temperature values recorded at the DFOS section are influenced by systematic effects of the Rayleigh sensing unit and, thus, are not further considered in this thesis. Brillouin sensing results at another cross section at the same construction lot, however, show that appropriate temperature values can be obtained using the DFOS system (cf. [58]).

The sensing unit used to interrogate the installed fibre optic sensing cable network features a measurement repeatability of $1 \,\mu\text{m/m}$ and $0.1 \,^{\circ}\text{C}$ ([233] in [266, p. 3]). The spatial sampling is 2 cm with a physical spatial resolution of 5 cm. The sampling rate was set to 1 minute at the beginning of the monitoring period, but was reduced as soon as the deformation of the shotcrete lining tended towards a stable value. [266, p. 2, 8]

For further reading on the distributed fibre optic sensing at tunnelling projects in Austria, refer, e.g., to [268, 269].

8.2 Geological and hydrogeological conditions

The DFOS section is in the fault zone system called *Haltestelle Eichberg Seitenverschiebung*. It's a sinistral (i.e., left-lateral) strike-slip fault system dipping north ([407, p. 137]) comprising several faults, fault zones, and damages zones different in thickness and orientation. Fig. 8.1 shows the extent of the fault system. The tunnel heads through it for more than 150 m. The DFOS section is close to the end of the system. The main fault zone of the system starts approx. at chainage 1365 m. There, the fault zone dips to NNW–N at a moderate to high angle. Approx. at chainage 1435 m, it changes its orientation and steeply dips to S. The top heading exits the fault zone approx. at chainage 1475 m. According to the site mappings (cf. [104]), the core of the fault zone extends from the beginning of the main fault zone to approx. chainage 1450 m. A damage zone characterises the end of the fault zone (i.e., the last 25 m). It is assumed that the fault and damage zones visible in the rightmost part of the section view in Fig. 8.1 are also structures associated with the large-scale fault system.

Approx. up to chainage 1440 m, the mapped foliation planes dip to the right tunnel side, mainly against the direction of the drive (DOD), and at a low to moderate angle (cf. Fig. 8.2a, and Tab. 8.7 on p. 183). They align sub-parallel to the main fault zone. As the orientation of the fault zone changes, also the trend of the orientation of the foliation planes does. In the last 40 m of the fault zone, the mapped foliation planes mainly dip to the left tunnel side and against the DOD; also at a low to moderate angle (cf. Fig. 8.2b). They do not align with the fault zone.

Along the tunnel alignment, the main fault zone comprises schists and phyllites often tectonically strongly overprinted. Rocks and fault rocks different in the degree of fracturing and in the share of cataclasites alternate heterogeneously. Fault rocks of core zones are often clayey to sandy cataclasites. Zones with a high share of cataclasites often are fine-grained and cohesive.

¹The achievable spatial sampling and resolution usually depends on the total cable length: 0.5 cm or even better for lengths less than 70 m; min. 3 cm for lengths up to 2 km. It is similar for the accuracy. [232]

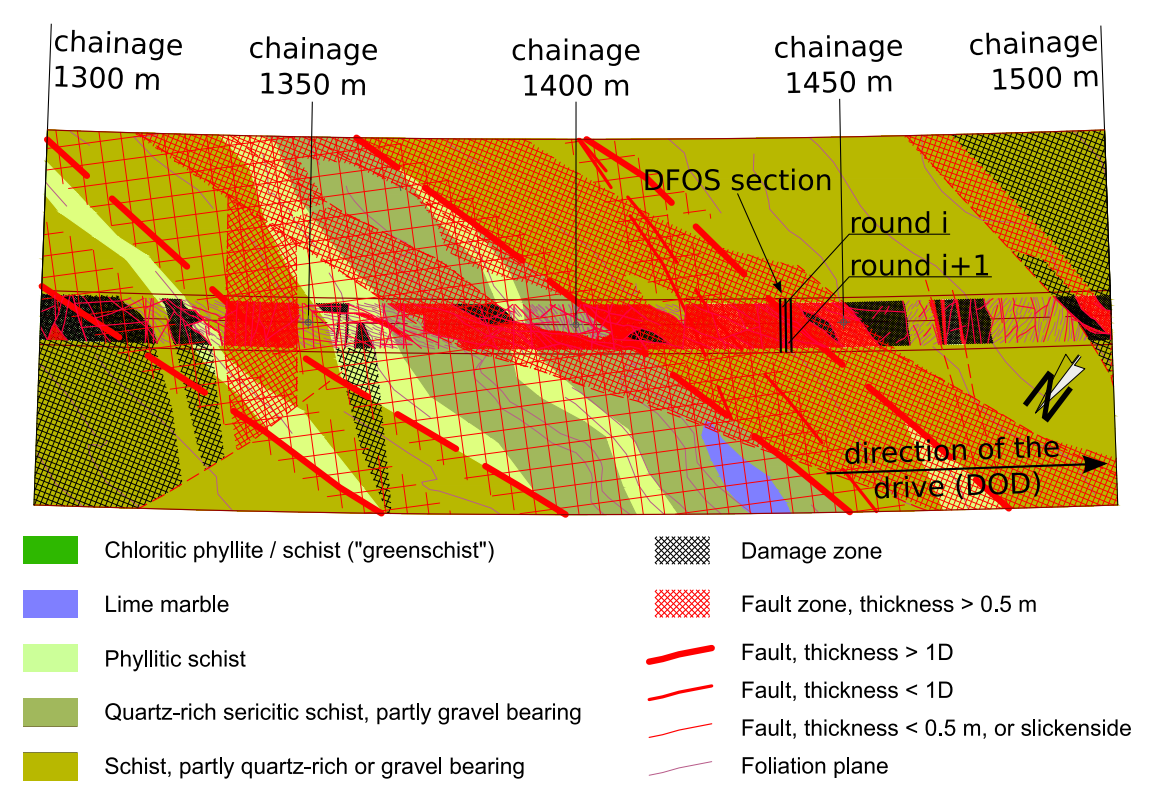


Figure 8.1: SBT1.1 \mid Gloggnitz: Plan view of the geological conditions from chainage 1300 m to chainage 1500 m, based on face mapping during excavation. The conditions outside the tunnel and large-scale structures are best estimates considering pre-excavation investigations and investigations during the heading.

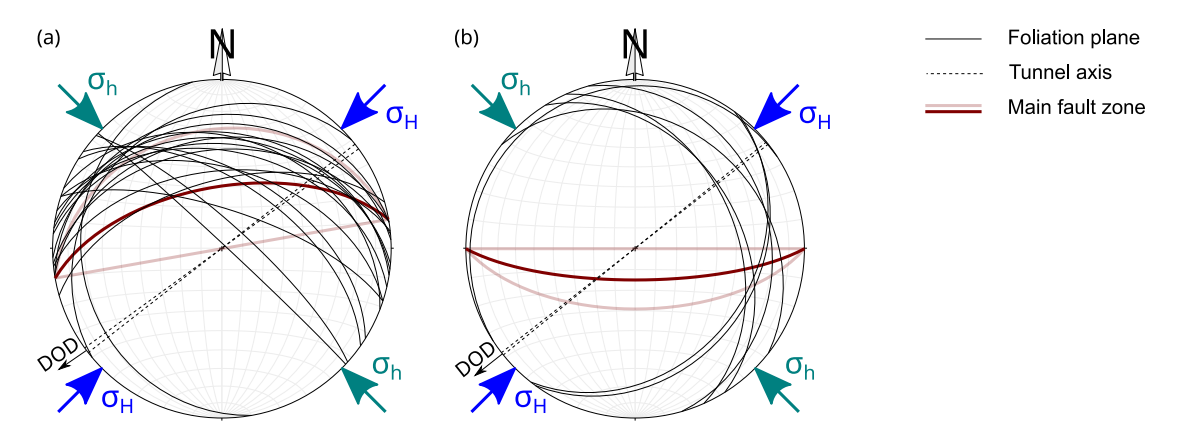


Figure 8.2: SBT1.1 | Gloggnitz: Schmidt net (equal area) plot of orientations of mapped foliation planes and of the main fault zone. (a) From chainage 1313.2 m to chainage 1439.2 m, and (b) from chainage 1450.2 m to chainage 1499.2 m; cf. Tab. 8.7 (p. 183). The light red great circles highlight the variation in the dip angle of the fault zone. The plots also include the direction of the tunnel drive and the approximate orientation of the minimum primary horizontal stress, σ_h , and of the maximum primary horizontal stress, σ_H . Graphs created with the free software Stereonet ([12, 13, 65]).

Less fractured fault rocks feature a lower share of cataclasites and the foliation is still observable. All of them are weak to very weak, but unweathered, and are moderately to highly anisotropic. More competent, less disintegrated shear bodies can feature a thickness of up to several metres. A reticular, secondary jointing usually characterises those shear bodies resulting in a small-sized fragmentation. The risk for large-scale caving is low because, overall, the interlocking between rock blocks is good and the number of geomechanically highly effective discontinuities is rather small. [105]

In the excavation area, the rock mass was dry or featured an inherent moisture. The amount of water ingress increases when approaching major faults, but usually remains below 0.1 l/s. Often, water trickles from drillings and rock bolts. [105]

From chainage 1432 m to chainage 1450 m, including the DFOS section, the strength of hand rock samples was classified to range predominantly between 1 and 5 MPa. Rocks are schists, sometimes quartz-rich, sericitic, or phyllitic, sericitic phyllites, and cataclasites. Minor shares of the tunnel face of less than 15% feature a strength of 5 to 25 MPa. Those areas usually comprise schists, which are often sericitic, chloritic, or phyllitic. [104]

The spacing of foliation planes, joints, faults, and slickensides is below 6 cm. Most discontinuities feature an undulated surface. Sometimes they are planar. The surfaces are usually smooth or polished. Fillings or gouges are often present. Their characteristics range from haematitic, clayey, silty, and sericitic to chloritic. Relative to the foliation planes, the orientation of all other discontinuities often differs strongly. [104]

At the DFOS section, the share of cataclasites is partly very high and the spacing of the discontinuities is below 2 cm. In immediate sections behind, the situation is similar. In those ahead, the mapped strength is a little higher and the fragmentation lower. The orientation of the foliation planes in the DFOS section is listed in Tab. 8.7 (p. 183). [104]

8.3 Rock mass types

Fig. 8.3 gives sketches of selected top-heading tunnel faces and some information on the identified rock mass types (RMT). Mapping the face, the geologist evaluates the rock strength for each characteristic area on hand rock samples using categories (e.g., $1 \dots 5$ MPa, $5 \dots 25$ MPa). Fig. 8.3 lists the maximum range for each face.

Tab. 8.1 lists the information on the RMT's shares for some more mapped tunnel faces. Approx. up to chainage 1455 m, RMT 8c often dominates. It is a fault material comprising phyllites and schists rich in phyllosilicates with a moderate share of cataclasites ([380, p. 32]). This type aims to describe a strongly anisotropic rock mass where more competent layers of parent rock (e.g., RMT 2b-2) alternate with heavily fractured cataclastic layers (i.e., RMT 8d or 8f) ([61, p. 65]).

Approx. from chainage 1455 m, the rock mass is dominated by RMT 2b-2 (cf. Tab. 8.1). It is a strongly fractured, sheared schist. RMT 8d is a fault material comprising phyllites and schists rich in phyllosilicates. And RMT 8f is a fault material comprising sericite phyllites. Both RMT 8d and 8f feature a high share of cataclasites. [380, p. 8, 33–34]

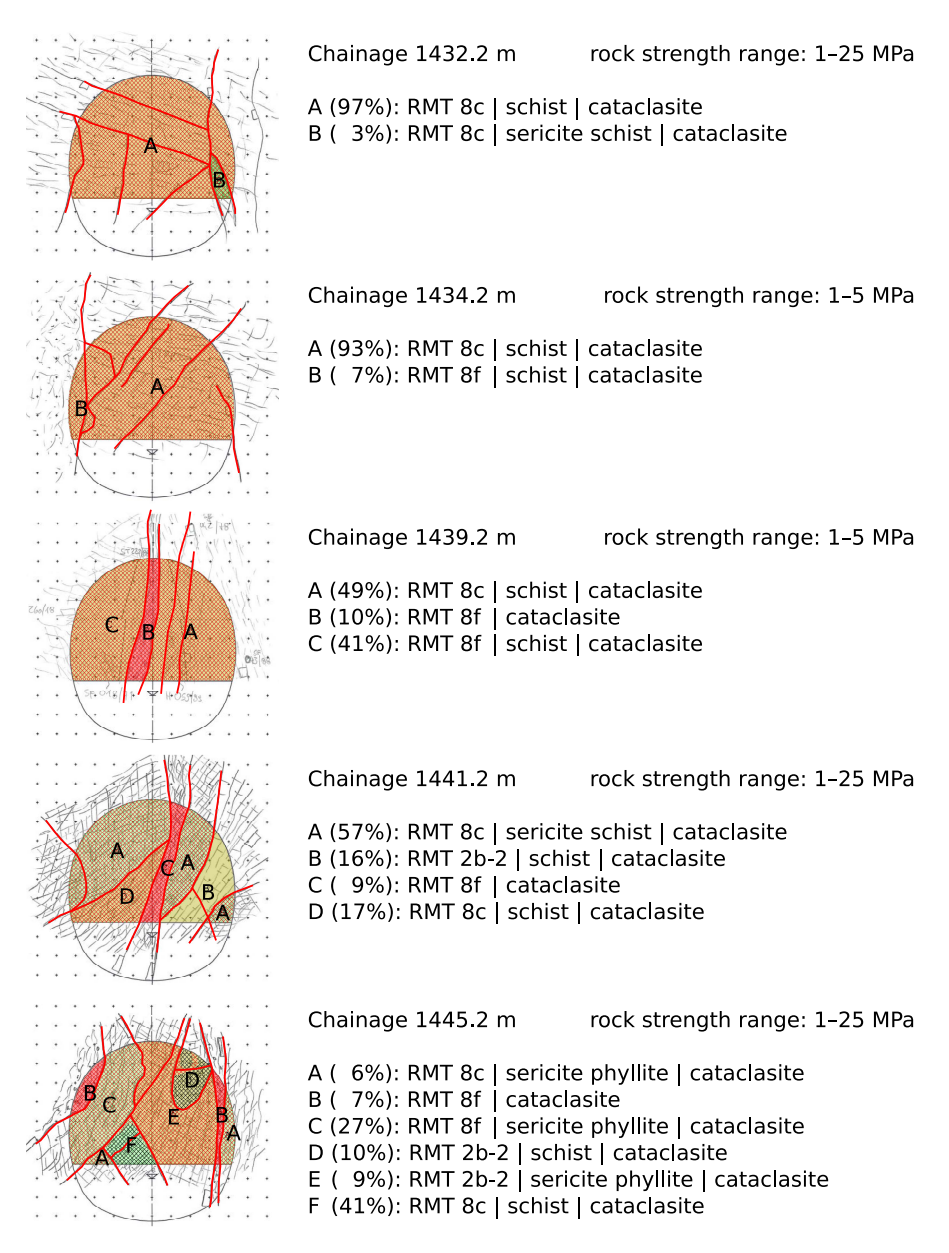


Figure 8.3: SBT1.1 | Gloggnitz: Sketches of the tunnel face at and close to the DFOS section including information on the areal share of the tunnel face by the rock mass types (RMT) (sketches and information from [104]).

Table 8.1: SBT1.1 | Gloggnitz: Areal share of the top-heading tunnel face by the rock mass types (RMT) in the DFOS section and sections nearby (information from [104]). Note that the distribution is similar at the mapped tunnel faces of the bench/invert heading (not listed).

	Are	al share o	of the top	-heading	tunnel fa	ce in per	cent
Chainage [m]	1407.2	1412.2	1418.2	1423.2	1432.2	1434.2	1439.2
RMT 2b-2	18	27	39	37	-	-	-
RMT 8c	48	55	61	43	100	93	49
RMT 8f	34	18	-	20	-	7	51
Chainage [m]	1441.2	1445.2	1450.2	1455.2	1459.2	1463.2	1471.2
RMT 2b-2	16	19	12	85	100	100	54
RMT 8c	74	47	28	_	-	-	45
RMT 8f	9	34	60	15	-	-	-

8.4 Primary stress state

The first of the two following subsections describes the primary stress state assumed to exist in the rock mass the underground constructions of the construction lot SBT 1.1 have to cope with. The second subsection draws conclusions about the primary stress state close to the DFOS section.

8.4.1 General

Considering results from hydraulic fracturing tests in boreholes, the tectonic setting (left-lateral strike-slip fault system), and the orientation of the rock mass structure on a regional scale, experts approximated the minimum primary horizontal stress, σ_h , to align with a NW to SE trend (cf. Fig. 8.2 on p. 171), and the maximum primary horizontal stress, σ_H , with a NE to SW trend. ([61, p. 83, 87])

Because of tectonic and topographic effects, the horizontal stresses increase disproportionately with depth. At great depths, tectonic effects will dominate. At shallow depths above the level of valley floors, the lack of lateral restraint probably results in reduced horizontal stresses. In particular, in sections of competent rock mass, the horizontal stresses are probably increased, and larger differences exist between the minimum and maximum component. On the tunnel level, for most parts, $\sigma_H > \sigma_v > \sigma_h$ where σ_v is the primary vertical stress. In major fault zones, to a large extent, a stress environment exists that is closer to being isotropic. Anyway, locally, differences may exist depending on the rock mass conditions. For σ_v , the overburden stress is used (cf. [103, p. 29]). Considering that, because of topographic effects, the vertical stress most likely is not equal to the overburden stress, the experts decided on the lateral pressure coefficients as follows: ([61, p. 83ff])

- Competent rock mass: $k_{0,h} = 0.7 \dots 1.0, k_{0,H} = 0.9 \dots 1.3;$
- Heavily fractured material, major fault zones: $k_{0,h} = k_{0,H} = 0.75...1.25$.

8.4.2 Primary stress at the analysed section

At the DFOS section, the overburden is approx. 135 m. It continuously decreases from approx. 140 m at chainage 1313.2 m to approx. 131 m at chainage 1499.2 m. RMT 8c predominates close to the DFOS section (cf. Tab. 8.1 on p. 173). Its unit weight is 25 kN/m³ (cf. Tab. 9.6 on p. 221). σ_v results in -3.4 MPa.

Because the azimuth of the DOD is 232° from N (cf. Tab. 8.7 on p. 183), the direction of σ_H deviates from it by 6° to 9° (cf. Fig. 8.2a on p. 171). Thus, σ_h almost matches with the primary horizontal in-plane stress.

The DFOS section is in the core and at the end of a fault zone (cf. Section 8.2 on p. 170 and Fig. 8.1 on p. 171). Even if it borders a more competent rock mass zone ahead, both are considered weak (cf. [407, p. 206]) compared to the host rock surrounding in large scale, also when referring to their capability for storing large differences in the primary principal stresses ([221]; cf. also [103, p. 29]).

That the side walls displace more than the crown (cf. Section 8.7.3 on p. 185 and Tab. 8.7) does not necessarily relate to a directed primary stress state. First, with approx. 6 cm (cf. Tab. 8.7), the displacements in the DFOS section are not that large given that the section is within the core of a fault zone. Consequently, the yield zone around the tunnel is probably relatively small. If the displacements of the side walls would be rather large, one could assume

higher vertical stresses. The latter lead to increased tangential stresses and a larger yield zone next to the side walls. Second, side wall displacements can exceed those of the crown even if the primary stress state is hydrostatic just because of the excavation geometry (cf. report on the UDEC calculations on p. 185). Thus, the in-plane horizontal stresses do not need to be increased at all.

In contrast, $k_{0,h}$ can be assumed < 1. The fault system crossing the analysed tunnel section is of strike-slip type (cf. Section 8.2 on p. 170). Supposing that Anderson's theory of faulting applies here (cf. Chapter 2 on p. 9) and recognising that the theoretical strike of the fault planes in Fig. 2.5c (p. 11) match well with the strike of the fault planes in Fig. 8.2 (p. 171) (both viewed relative to the orientation of the primary horizontal stresses), then one primary horizontal stress component at the analysed section is the minor principal stress, σ_3 . Note that the theory assumes an angle between the fault planes and the major principal stress, σ_1 , of $45^{\circ} - \varphi/2$. Here, it is between 35° (cf. Fig. 8.2a) and 45° (cf. Fig. 8.2b) relative to σ_H . Differences may be because of the theory's simplifications (cf. Chapter 2).

This study sets $k_{0,H} = 1$ and $k_{0,h} = 0.75$. Then, $\sigma_v = \sigma_H = \sigma_1 = \sigma_2$ and $\sigma_h = \sigma_3$. That $\sigma_1 = \sigma_2$ and not $\sigma_1 > \sigma_2$ (like it is in Fig. 2.5c) may explain why the main fault zone is not vertical but dips at a moderate to high angle (cf. Fig. 8.2). Note the different orientation of σ_1 and σ_2 in Fig. 2.5a and Fig. 2.5c, and the resulting orientation of the fault planes. Is it here a combination of both faulting types? Anyway, selecting $\sigma_h < \sigma_H$ is supported by a study performed by [216]. She analysed the influence of the orientation of the primary principal stresses on the displacement characteristics of a tunnel drive numerically and in three dimensions. In one case (cf. [216, p. A-58]), the orientation of the stresses is like it is here: σ_1 and σ_2 align with the vertical plane parallel to the tunnel axis, whereas σ_3 is perpendicular to it. In that case, $\sigma_1 > \sigma_2$. Here, $\sigma_1 = \sigma_2$. But in both cases, $\sigma_2 > \sigma_3$, and the ratio of σ_1 to the equivalent uniaxial peak compressive strength of the rock mass is close to -5. The numerical results suggest that the tunnel periphery displaces longitudinally against the DOD; the side walls more than the crown. And the same displacement characteristic was recorded at the DFOS section (cf. Fig. 8.8 on p. 182).

Because the overburden does not vary much, topographic effects can be excluded. And by neglecting differences in the rock mass density in the numerical model between Zone A, B, and C (cf. Section 9.4 on p. 210), the primary principal stress state at the tunnel level is the same in all zones:

- $\sigma_{v,A} = \sigma_{v,B} = \sigma_{v,C} = -3.4 \text{ MPa};$
- $\sigma_{h,A} = \sigma_{h,B} = \sigma_{h,C} = k_{0,h} \cdot \sigma_v = 0.75 \cdot (-3.4) = -2.55 \text{ MPa};$
- $\sigma_{H,A} = \sigma_{H,B} = \sigma_{H,C} = k_{0,H} \cdot \sigma_v = 1 \cdot (-3.4) = -3.4 \text{ MPa}.$

8.5 Tunnelling method

The DFOS section and close tunnel sections behind and ahead have been excavated with an excavator. The tunnel drive was separated into two headings: (1) the top heading (th), and (2) the bench/invert heading (bih). The round length of the top heading is 1 m, and of the bench/invert heading it is 2 m. The distance between the top heading and the bench/invert heading ranged between 8 m and 30 m ([267, p. 4]).

8.5.1 Excavation sequence

Fig. 8.4 graphs the construction sequence at and close to the DFOS section. Because of the installation of the DFOS system and related delays, the interruption in tunnelling at the DFOS section and the following top-heading round was longer than usual.

Note that at the DFOS section, before the second layer of shotcrete was applied, round i+1 got excavated. After applying the first layer of shotcrete at round i+1, a DFOS cable could be installed extending across both rounds (cf. Section 8.6 on p. 180). Then, the second shotcrete layer was applied at both round i and round i+1 (cf. time of shotcrete application highlighted in Fig. 8.4).

Tab. 8.2 lists the construction sequence in detail, the moment of the reference measurements, and time differences of actions related to the reference measurements of the DFOS system at the top heading. Particularly note the moment of ring closure.

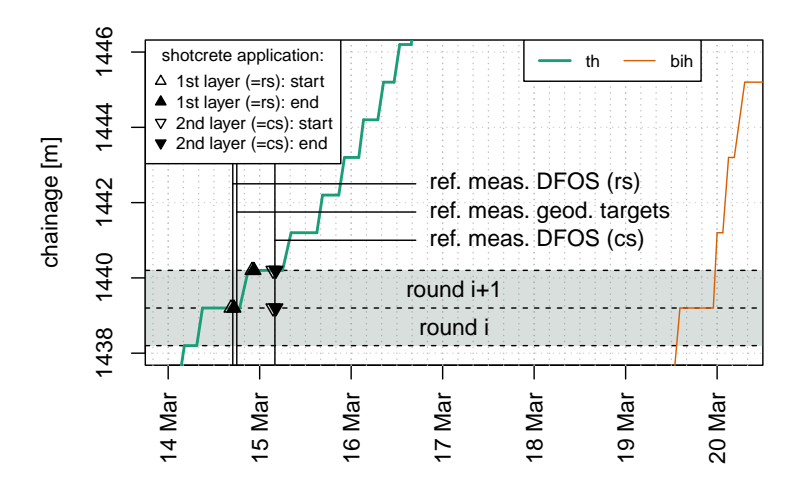


Figure 8.4: SBT1.1 | Gloggnitz: Construction sequence from chainage 1438.2 m to chainage 1446.2 m. The plot highlights the moment of reference measurements at the DFOS section. th ... top heading, bih ... bench/invert heading, rs ... rock side, cs ... cavity side. Information from personal notes and from [342].

8.5.2 Support

Tab. 8.3 and Tab. 8.4 list the installed support at the top heading and bench/invert heading, respectively, at and close to the DFOS section.

8.5.3 Work steps

Tab. 8.5 and Tab. 8.6 (both on p. 179) list the work steps for constructing the rounds of the top heading and bench/invert heading, respectively, at and close to the DFOS section. Particularly note the comment (d) in Tab. 8.5 on the installation of the radial rock bolts at the DFOS section of the top heading.

Table 8.2: SBT1.1 | Gloggnitz: Construction sequence of and ahead of the DFOS section, moments of reference measurements at the DFOS section, and time differences to the DFOS reference measurements. The time given for excavation includes excavations works and in case of partial face excavation (only at the top heading) the installation of temporary face support between. It does not include the installation of temporary support at the last partial face. Shotcreting times are only given for the DFOS section. The times for instrumentation (DFOS system, strain gauges, pressure cells) are not included. Information from personal notes and from [342].

	Time difference										
				Chainag	ge [m]	Date	Time	rel. to	th rs	rel. to	th cs
Action				from	to	[dd/mm/yy]	[hh:mm]	[h]	[d]	[h]	[d]
excav.	th	-	S	1438.2	1439.2	14/03/17	07:30	-9.45	-0.39	-20.50	-0.85
excav.	$^{ m th}$	-	\mathbf{E}	1438.2	1439.2	14/03/17	09:00	-7.95	-0.33	-19.00	-0.79
shoter.	$^{\mathrm{th}}$	rs	\mathbf{S}	1438.2	1439.2	14/03/17	16:30	-0.45	-0.02	-11.50	-0.48
0r DFOS	$^{\mathrm{th}}$	rs	-	-		14/03/17	16:57	0.00	0.00	-11.05	-0.46
shoter.	$^{\mathrm{th}}$	$_{\rm rs}$	\mathbf{E}	1438.2	1439.2	14/03/17	17:15	0.30	0.01	-10.75	-0.45
0r geod.	-	-	-	-		14/03/17	18:00	1.05	0.04	-10.00	-0.42
excav.	$^{\mathrm{th}}$	-	\mathbf{S}	1439.2	1440.2	14/03/17	18:45	1.80	0.08	-9.25	-0.39
excav.	$^{\mathrm{th}}$	-	\mathbf{E}	1439.2	1440.2	14/03/17	21:00	4.05	0.17	-7.00	-0.29
shoter.	$^{\mathrm{th}}$	cs	\mathbf{S}	1438.2	1439.2	15/03/17	03:30	10.55	0.44	-0.50	-0.02
0r DFOS	th	cs	-	-		15/03/17	04:00	11.05	0.46	0.00	0.00
excav.	$^{\mathrm{th}}$	cs	\mathbf{E}	1438.2	1439.2	15/03/17	04:15	11.30	0.47	0.25	0.01
excav.	$^{\mathrm{th}}$	-	\mathbf{S}	1440.2	1441.2	15/03/17	06:00	13.05	0.54	2.00	0.08
excav.	$^{ m th}$	-	\mathbf{E}	1440.2	1441.2	15/03/17	08:15	15.30	0.64	4.25	0.18
excav.	$^{\mathrm{th}}$	-	\mathbf{S}	1441.2	1442.2	15/03/17	15:00	22.05	0.92	11.00	0.46
excav.	$^{\mathrm{th}}$	-	\mathbf{E}	1441.2	1442.2	15/03/17	16:30	23.55	0.98	12.50	0.52
excav.	$^{ m th}$	-	\mathbf{S}	1442.2	1443.2	15/03/17	20:45	27.80	1.16	16.75	0.70
excav.	$^{\mathrm{th}}$	-	\mathbf{E}	1442.2	1443.2	15/03/17	22:15	29.30	1.22	18.25	0.76
				1	m	= round leng	th top head	ing			
excav.	bih	_	S	1435.2	1437.2	19/03/17	10:00	113.05	4.71	102.00	4.25
excav.	$_{ m bih}$	-	\mathbf{E}	1435.2	1437.2	19/03/17	11:30	114.55	4.77	103.50	4.31
excav.	$_{ m bih}$	-	\mathbf{S}	1437.2	1439.2	19/03/17	12:30	115.55	4.81	104.50	4.35
excav.	$_{ m bih}$	-	\mathbf{E}	1437.2	1439.2	19/03/17	14:15	117.30	4.89	106.25	4.43
0r DFOS	$_{ m bih}$	rs	-	-		19/03/17	20:39	123.70	5.15	112.65	4.69
shoter.	$_{ m bih}$	$_{\rm rs}$	\mathbf{E}	1437.2	1439.2	19/03/17	20:45	123.80	5.16	112.75	4.70
shoter.	$_{ m bih}$	cs	\mathbf{E}	1437.2	1439.2	19/03/17	23:00	126.05	5.25	115.00	4.79
					the ring	at round i is n	ow closed				
excav.	$_{\mathrm{bih}}$	-	\mathbf{S}	1439.2	1441.2	19/03/17	23:00	126.05	5.25	115.00	4.79
excav.	$_{ m bih}$	-	\mathbf{E}	1439.2	1441.2	20/03/17	00:00	127.05	5.29	116.00	4.83
excav.	$_{ m bih}$	-	\mathbf{S}	1441.2	1443.2	20/03/17	01:30	128.55	5.36	117.50	4.90
excav.	bih	-	\mathbf{E}	1441.2	1443.2	20/03/17	03:00	130.05	5.42	119.00	4.96
				2	m	= round leng	th bench/in	vert head	ling		

excav. ... excavation, shotcr. ... shotcreting, 0r DFOS ... zero reading (= reference measurement) DFOS system, 0r geod. ... zero reading (= reference measurement) geodetic monitoring targets, th ... top heading, bih ... bench/invert heading, rs ... rock side, cs ... cavity side, S ... Start, E ... End

Table 8.3: SBT1.1 | Gloggnitz: Specifications of the support of the top heading at and close to the DFOS section. Information from [346].

Primary suppo	Primary support of the side walls and the crown					
Shotcrete	SpC 20/25/J2/RV ([289, p. 26ff]: minimum characteristic compressive strength $f_{ck,min} = 25$ MPa for cores with $h/d = 1$, early strength class J2, RV reduced leaching behaviour), thickness $t = 25$ cm					
Wire mesh	AQ 60 (in both directions: cross-sectional area $A=2.83~\mathrm{cm^2/m}$), one layer of wire mesh in each shotcrete layer					
Lattice girder	3 bar type 95/20/30 (distance between upper and lower bar [mm]/diameter of lower bar [mm]/diameter of upper bar [mm]), cross-sectional area $A = 13.35 \text{ cm}^2/\text{m}$, section modulus $S_x = 66 \text{ cm}^3$ and area moment of inertia $I_x = 485 \text{ cm}^4$ with x in the direction of the tunnel drive					
Bolts	12–13x grouted IBO self-drilling rock bolts with hollow bars installed radially, length $L=6$ m, maximum tensile force (or nominal ultimate load) $F_{t,max}=250~\rm kN$					
Temporary face	e support					
Shotcrete	same as for side walls (see above), 90% of face area with thickness $t = 10$ cm and wire mesh, 10% of face area with thickness $t = 5$ cm and unreinforced					
Wire mesh Bolts	AQ 50 (in both directions: cross-sectional area $A=1.96~\rm cm^2/m$), one layer 8x grouted IBO self-drilling rock bolts with hollow bars installed ahead of the tunnel face and interlocked with the tunnel face by load distribution plates, length $L=12~\rm m$, maximum tensile force (or nominal ultimate load) $F_{t,max}=350~\rm kN$					
Primary suppo	rt ahead of the tunnel face					
Spiles	approx. 25x non-grouted tube spiles, outer diameter $OD=38$ mm, wall thickness $t=4$ mm, length $L=4$ m, circumferential spacing $e<30$ cm					

Table 8.4: SBT1.1 | Gloggnitz: Specifications of the support of the bench/invert heading at and close to the DFOS section. Information from [346].

Support of t	Support of the side walls and the invert							
Shotcrete	SpC $25/30/J2/RV$ ([289, p. 26ff]: minimum characteristic compressive							
	strength $f_{ck,min} = 30$ MPa for cores with $h/d = 1$, early strength class							
	J2, RV reduced leaching behaviour), thickness $t = 30$ cm							
Wire mesh	AQ 60 (in both directions: cross-sectional area $A = 2.83 \text{ cm}^2/\text{m}$), one layer							
	of wire mesh in each shotcrete layer							

Table 8.5: SBT1.1 | Gloggnitz: Work steps at the top heading at and close to the DFOS section. For the chainages of the rounds, c.f. Fig. 8.4 (p. 176). Information from personal notes and from [342].

Nor	mal sequence close to DFOS section	Sea	uence at DFOS section (incl. round after)
#	Action	#	Action
01	round i, alternately ^a : mechanical excavation, mucking, face support ^b	01	round i, alternately ^a : mechanical excavation, mucking, face support ^b
02	round i, 1st layer wire mesh	02	round i: 1st layer wire mesh
03	round i, lattice girder	03	round i: lattice girder
04	round i-1, 2nd layer wire mesh	04	round i, 1st layer: DFOS cables, strain gauges, pressure cells
05	round i, 1st layer shotcrete	05	round i, 1st layer: shotcrete
06	round i-1, 2nd layer shotcrete	06	round i: spiles
07	round i, spiles	07	round i+1, alternately ^a : mechanical excavation, mucking, face support ^b
08	round i-1, radial rock bolts; round i, each 7th round rock bolts ahead of the tunnel face	08	round i+1: lattice girder
		09	round i and i+1, 2nd layer: wire mesh
		10	round i, 2nd layer: strain gauges, pressure cells
		11	round i+1: spiles
		12	round i, 2nd layer: DFOS cables ^c
		13	round i and i+1, 2nd layer: shotcrete
		14	rock bolts ahead of the tunnel face
		15	radial rock bolts ^d

^a Partial face excavation: at and close to the DFOS section two partial faces

Table 8.6: SBT1.1 | Gloggnitz: Work steps at the bench/invert heading at and close to the DFOS section. For the chainages of the rounds, c.f. Fig. 8.4 (p. 176). Information from personal notes and from [342].

Nor #	rmal sequence close to DFOS section Action	Sequence at DFOS section # Action							
01	round i, alternately: mechanical excavation, mucking	01	round i, alternately: mechanical excavation, mucking						
02	round i, face support ^a	02	round i, face support ^a						
03	round i, 1st layer wire mesh	03	round i: 1st layer wire mesh						
04	round i, 1st layer shotcrete	04	round i, 1st layer: DFOS cables, strain gauges, pressure cells round i, 1st and 2nd layer: strain gauges,						
05 06	round i, 2nd layer wire mesh round i, 2nd layer shotcrete	05 06 07 08	pressure cells round i, 1st layer: shotcrete round i: 2nd layer wire mesh round i, 2nd layer: DFOS cables round i, 2nd layer: shotcrete						

^a A thin base layer of shotcrete, also at the side walls and the invert

^b Includes a thin base layer of shotcrete at the side walls and the crown

 $^{^{\}rm c}$ DFOS cables extent into the 2nd shotcrete layer of round i+1

 $^{^{\}rm d}$ After excavation and shot creting of round i+2, installation of rock bolts at round i and round i+1

8.6 Position of monitoring devices

The top heading is equipped with five bi-reflex targets for standard monitoring of the tunnel displacements with geodetic total stations. The monitoring targets (MT) are next to the crown, at the shoulders, and at the side walls (cf. Fig. 8.5). It's a usual setup at conventional tunnel drives. The DFOS section is additionally equipped with the DFOS system, and for evaluation purposes with vibrating wire strain gauges (SG) and pressure cells (PC). For the latter, refer to [266, 415, 416].

At the top heading, both the rock-side shotcrete layer and the cavity-side shotcrete layer comprise DFOS cables. At the bench/invert heading, only the rock-side shotcrete layer does.² DFOS cables are aligned straight in the circumferential direction perpendicular to the tunnel axis (cf. cables 'circ' in Fig. 8.6). Other cables or cable segments are also guided in a loop configuration being alternately aligned parallel and perpendicular to the tunnel axis (cf. cables 'long' and 'long2' in Fig. 8.6). The latter allows to monitor strain also in the longitudinal direction (i.e., in the direction of the tunnel drive).

At the rock-side layer of the top-heading lining, the DFOS cables in the loop configuration cross only parts of one shotcrete round (cf. Fig. 8.7). At the cavity-side layer, the cable 'long2' extends also to the round ahead. The reader is asked to imagine the rock-side layer in Fig. 8.6 lying on top of the cavity-side layer to get an idea about the relative distances between cable segments, monitoring devices, etc.

The alignment of the DFOS cables in the rock-side shotcrete layer of the bench/invert heading is not sketched here. The thesis focuses on the short-term prediction of stiff blocks ahead of the tunnel face using data from geodetic measurements. The latter is available only at the top heading. For the alignment of the DFOS cables at the bench/invert, refer to [415, 416].

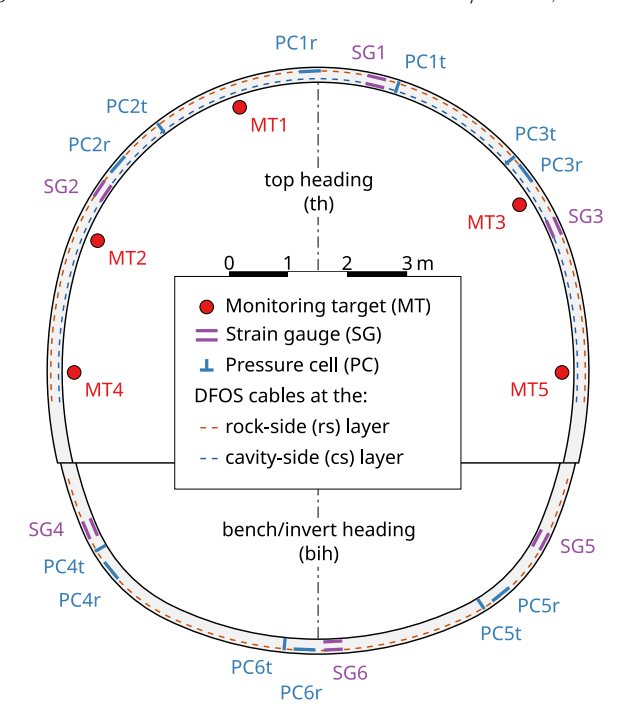


Figure 8.5: DFOS section: Schematic cross section of the tunnel, including the location of the monitoring targets (MT), of strain gauges (SG), and of pressure cells (PC) (modified from [415, Fig. 5.5, p. 36]). The view is in the direction of the drive (DOD).

²Note that the bench/invert heading also comprises cables in the cavity-side shotcrete layer. However, after shotcreting the DFOS interrogation unit could not establish a connection with them anymore. Thus, no information is available from those cables.

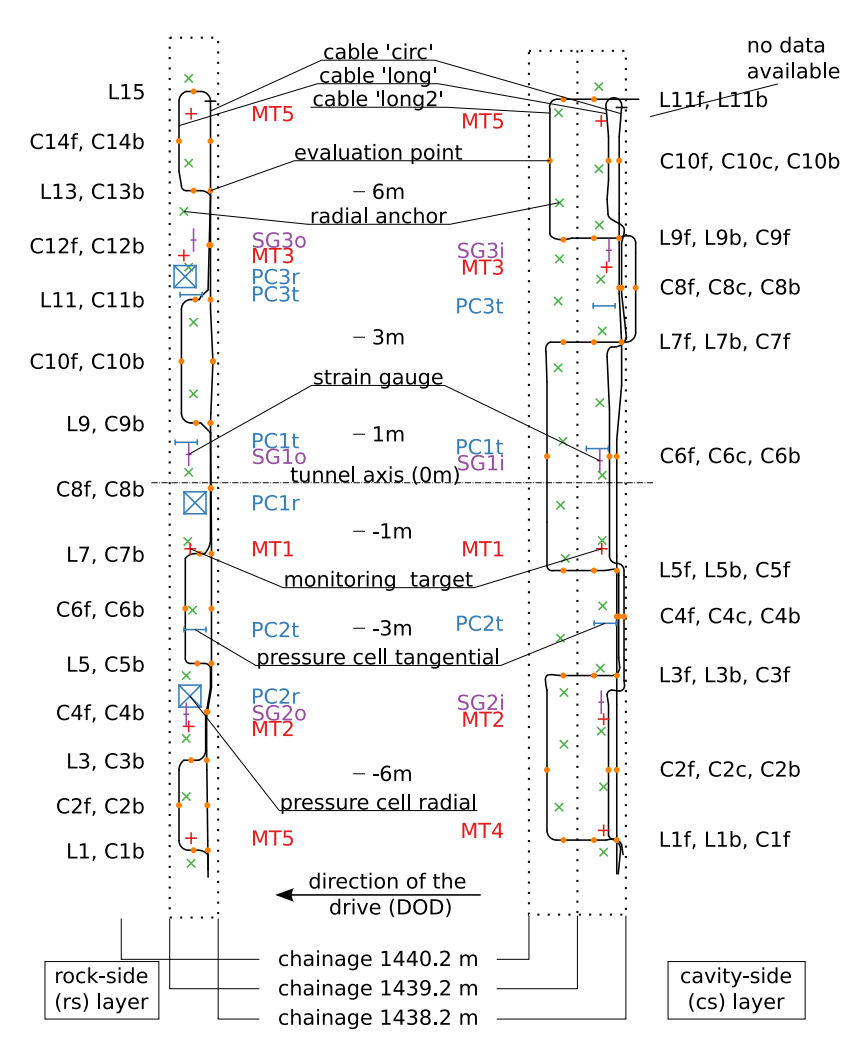


Figure 8.6: DFOS section | top heading: Routes of DFOS cables (developed top view) and positioning of DFOS evaluation points (Cix, Li, Lix: b...back = farther away from the current tunnel face, f...front = closer to the current tunnel face), geodetic monitoring targets (MTi), strain gauges (SGix: o...outer = rock-side layer, i...inner = cavity-side layer), pressure cells (PCix: r...radial, t...tangential), and radial rock bolts. The symbol size does not match with the individual actual instrument size. Thus, symbols may overlap here, but do not in reality. The evaluation points are used for the graphs in Fig. 8.12 (p. 189), Fig. 8.13 (p. 192), and Fig. 8.14 (p. 193).

8.7 Observed system behaviour: Geodetic measurements

Fig. 8.8 plots the development of the monitored displacements of five targets mounted on the shotcrete lining between chainage 1438.7 m and chainage 1438.9 m. Within the first days, because of the top-heading advance, the displacements increase significantly in all directions. Shortly after the ring closure (i.e., bench/invert heading has passed round i), the displacements in the horizontal direction—in-plane (i.e., perpendicular to the tunnel axis)—come close to their ultimate level. However, the advance of the top heading still effects the displacement components in the other directions, although to a lower amount than before the ring closure. The increase in the vertical and longitudinal displacements reduces significantly after day 10. Note that nine hours pass between the end of the excavation of round i and the geodetic reference measurement (cf. Tab. 8.2 on p. 177). The displacements developing during this time are not recorded.

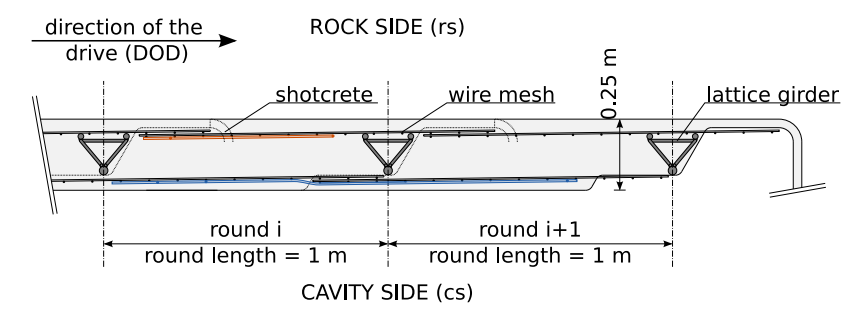


Figure 8.7: DFOS section | top heading: Schematic cross section of the shotcrete lining, including the DFOS cables (modified from [415, Fig. 5.3, p. 34]).

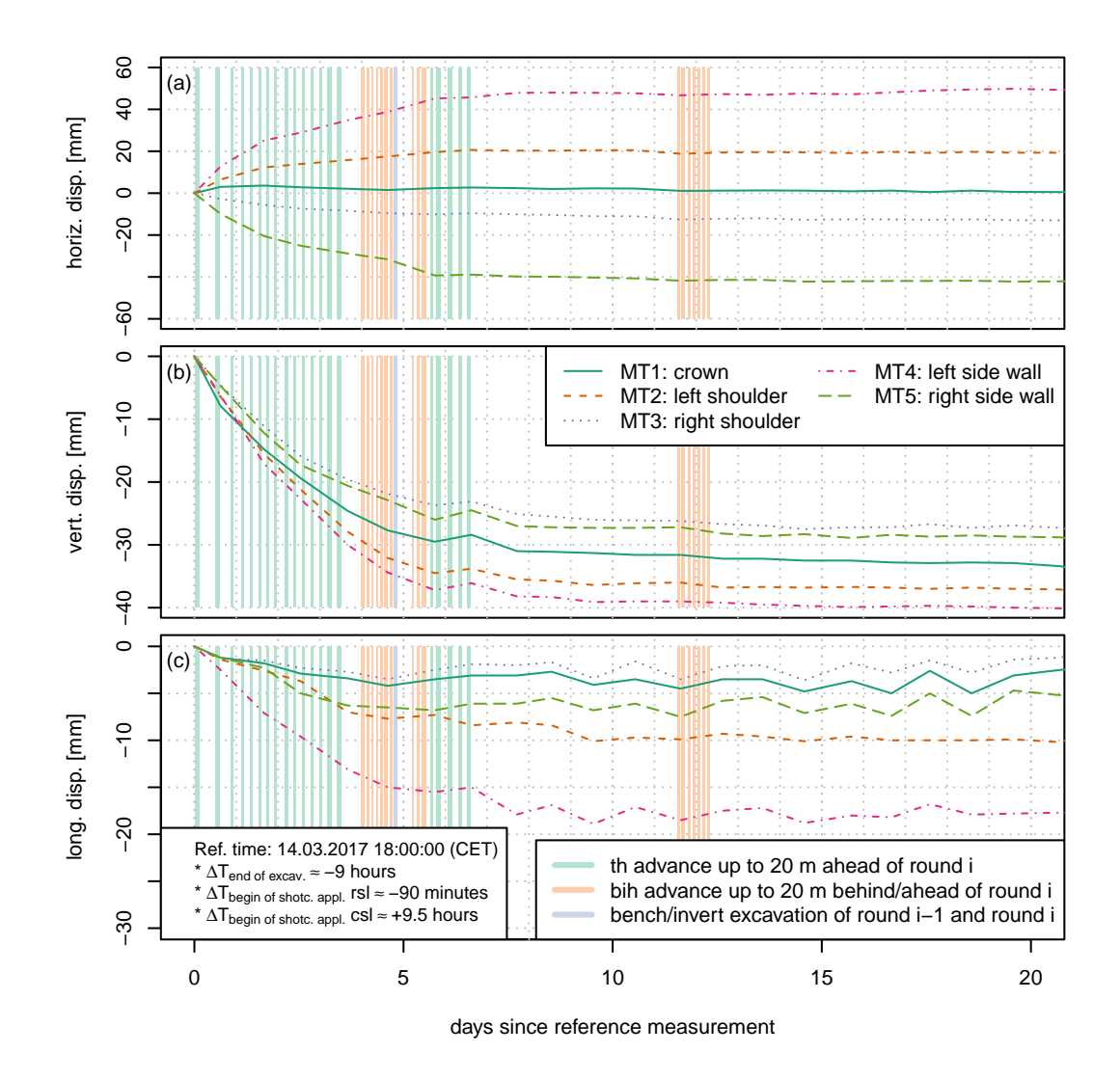


Figure 8.8: DFOS section | top heading: Development of the tunnel displacements monitored with five geodetic targets (cf. Fig. 8.5 on p. 180). (a) horizontal displacements (displacement to the left: negative value); (b) vertical displacements (displacement downwards: negative value); (c) longitudinal displacements (displacement against the direction of the drive: negative value). Note the different scaling of the ordinate axes. th...top heading, bih...bench/invert heading, csl...cavity-side layer, rsl...rock-side layer, MT...monitoring target.

Table 8.7: SBT1.1 | Gloggnitz: Evaluation and categorisation (CAT) of monitored displacements (a) and of mapped orientations of foliation planes (b) between chainage 1300 m and chainage 1500 m. For visualisation, Fig. 8.9 plots the displacements at four selected monitoring cross sections.

(a)								Displa	cement	s at mor	nitoring o	cross-se	ections							
Chainage [m]	1312	1321	1331	1340	1350	1359	1370	1379	1389	1401	1412	1422	1432	1439	1449	1459	1470	1482	1491	1498
							<		mai	n fault z	one app	rox. fror	n 1365 ı	m to 147	75 m		>			
CAT of horiz. disp.*	1	1	1	3	2	2	2	3	1	1	3	2	3	2	3	1	1	3	3	1
CAT of vert. disp.*	1	1	1	1	2	2	3	1	1	1	3	3	1	2	2	2	1	3	3	1
CAT of long. disp.*, **	2	2	2	2	2	2	2	2	2	2	2	2	2	2	2	2	1	3	3	3
max. rad. disp. [mm]	42	30	42	41	72	57	52	45	42	50	67	45	57	57	67	69	70	56	50	49
mean rad. disp. [mm]	20	22	29	32	42	35	33	36	31	33	42	30	43	39	54	47	50	45	38	38
	1	R > L		2	L>R		3	L≈R		R righ	nt tunnel	side		L left	tunnel s	side				
	* Our literity and a spiration (CAT) associated by the associated by the side well and at the absoluter																			
	* Qualitative categorisation (CAT) considering the monitoring targets at the side walls and at the shoulders																			
	** Categorisation of the displacements against the direction of the drive (DOD)																			
Dian valationas	(m			احد الدد ،																
Disp. relations: V _{MT1} /max(H _{MT4} ; H _{MT5})	0.3	0.5	0.5	; cell col 0.7	0.3	0.4	0.5	0.7	0.5	0.4	0.4	0.5	0.5	0.7	0.8	0.6	0.6	0.6	0.8	0.7
$V_{MT1}/Max(\Pi_{MT4}; \Pi_{MT5}) $ $V_{MT1}/max(V_{MT4}; V_{MT5})$	0.5	0.6	0.6	0.7	0.5	0.4	0.8	0.7	0.5	0.4	0.4	0.9	0.5	0.7	0.8	0.6	0.8	0.6	0.8	0.7
	0.5	0.6	0.8	1.0	1.5	1.8	1.5	1.1	0.5	0.6	1.2	1.4	1.1	1.3	1.0	0.7	0.8	1.1	0.9	0.9
H _{MT4} /H _{MT5}	0.4	0.9	0.0	1.0	1.5	1.0	1.0	1.1	0.7	0.9	1.2	1.4	1.1	1.3	1.0	0.0	0.7	1.1	0.0	0.0
	V vertical displacements MT1: monitoring target at the crown MT4: monitoring target at the left side wall																			
		rizontal c				With monitoring target at the crown						MT5: monitoring target at the right side wall								
														g g		9				
(b)						C	Prientation	on of foli	ation pl	anes ma	pped at	top-hea	ading tur	nel face	es					
Chainage [m]	1313.2	1322.2	1332.2	1341.2	1351.2	1360.2	1371.2	1380.2	1389.2	1402.2	1412.2	1423.2	1432.2	1439.2	1450.2	1459.2	1471.2	1483.2	1492.2	1499.2
							<		mai	n fault z	one app	rox. fror	n 1365 i	m to 147	75 m		>			
DOD [°]	234	234	234	234	234	233	233	233	233	233	232	232	232	232	232	232	231	231	231	231
DD/dip foliation [°]	013/42	018/51	354/52	005/38	351/35	351/22	355/41	021/35	320/21	035/58	357/27	007/35	032/53	018/71	128/31	074/21	126/28	066/40	058/38	327/05
		009/32		344/57										042/78	308/68					038/25
														043/88						
	DOD	direction	n of the	drive		DD d	ip direct	ion		dip di	p angle			260/18						
				ht tunnel	side	Dip to the righ						side			Dip to the left tunnel side					
	and against the DOD					and in the D					טי				and against the DOD					
CAT of dia angle.																				
CAT of dip angle:						~					~									WW
CAT of dip angle: low (0–30°) moderate (30–60°)	х	XX	x	XX	x	Х	x	X	Х	x	Х	x	х	Х	х	Х	х	х	Х	XX

8.7.1 Time-dependent displacements

Because the foliation planes in the rock mass ahead of the DFOS section dip against the DOD at a low to moderate angle (cf. Tab. 8.7b), they allow for a redistribution of stresses towards the DFOS section when rounds ahead are excavated. They would not, or the amount of redistributed stresses would be significantly lower, if the planes, for example, strike perpendicular to the tunnel axis and dip steeply. Here, the redistributed stresses from ahead cause further vertical and longitudinal displacements at the DFOS section after the ring closure.

After the top-heading round from chainage 1432.2 m to chainage 1433.2 m was excavated, no excavation has taken place close to this section for almost 42 hours. During this time, the bench/invert heading continued far behind. Anyway, the displacement of the lining at the monitoring cross section approx. at chainage 1432 m still increased, first at a high rate, then at a lower rate (not shown). Thus, even though no advance is made, ongoing stress redistribution and local failure in the rock mass close-by results in delayed displacements. Similar long-term effects probably contribute also to the displacements recorded at the DFOS section.

8.7.2 Out-of-plane displacements

Interestingly, the displacement of the left tunnel side against the DOD is always larger than the displacement of the right tunnel side at all analysed monitoring cross sections before the DFOS section (cf. Tab. 8.7a and Fig. 8.9a/b). This directly relates to the orientation of the foliation planes and of the fault zone (cf. Section 8.2 on p. 170 and Tab. 8.7b). As soon as the orientation changes, also the displacement characteristics change.

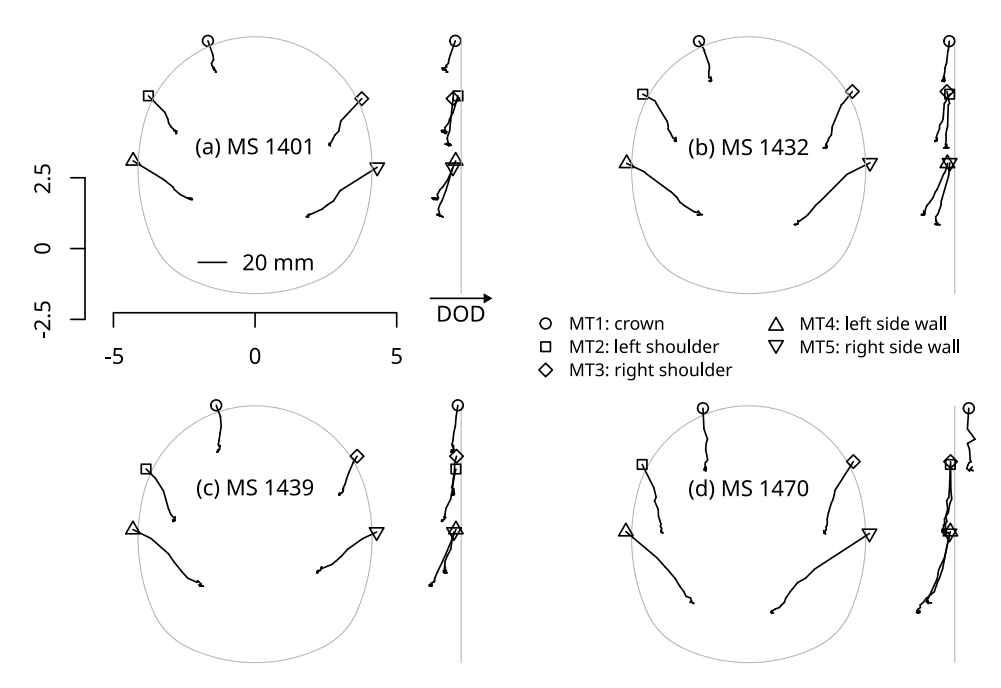


Figure 8.9: SBT1.1 | Gloggnitz: Displacement vector plots in the cross and longitudinal section view for the monitoring cross sections (MS) at chainage $1401 \, \text{m}$, $1432 \, \text{m}$, $1439 \, \text{m}$, and $1470 \, \text{m}$. Displacement vectors are scaled up by a factor of 50. The graphs show the displacements development within 20 days after the reference measurement at the individual monitoring cross section.

In [200], the first 1 km of the same tunnel has been analysed regarding the displacement characteristics. The authors show that, for example, whether the left tunnel side displaces more, or the right one, not only depends on the orientation of weakness planes such as foliation planes, but also on the mechanical significance of the planes, on the strength-stress ratio of the surrounding rock³, and on the primary stresses. One influencing factor can overrule another, locally or on a larger scale. If, for example, the primary stresses are directed and the strength-stress ratio of the rock is very low, yield zones may get quite large at particular locations around the tunnel and there result in increased tunnel displacements. This could be misinterpreted as the major primary stresses being aligned with the direction of the largest displacements. Anyway, any natural feature (e.g., residual tectonic stresses at faults, mechanically highly effective slickensides, weak shear bands) or significant changes in the support or excavation method (in particular local ones) alter the characteristics of monitored displacements. Consider also the difference between total and monitored displacements (cf., e.g., [291, Fig. 37, p. 42]).

That the left tunnel side displaces more against the DOD than the right tunnel side matches with the findings by [92]. The author performed three-dimensional numerical analyses using the Ubiquitous Joint model and simulated tunnel drives in transversely isotropic rock masses. For a case where the foliation dips at an angle of 75° to the left tunnel side and against the DOD, the right side wall displaces against the DOD, whereas the left side wall displaces in the DOD (cf. [92, Fig. 60 on p. 67]). In the case studied here, at, close to, and before the DFOS section, the situation is kind of mirrored around the tunnel axis. The foliation dips to the right tunnel side, mainly at a moderate angle. Both the left and right side walls displace against the DOD, but the right side wall to a (much) lower amount.

³For example, the ratio of the uniaxial compressive rock strength to the maximum elastic tangential in-plane stresses around a circular opening according to [197]. For the latter, cf. Section A.5 on p. 319 in the appendix.

Note that

- the dip angle strongly determines the displacement characteristics (cf. [92, Fig. 60 on p. 67]),
- the primary and, thus, the secondary stresses determine the stresses acting on weakness planes either preventing shear failure, or promoting it,
- in the case of [92] cited here, the absolute value of the minimum strength-stress ratio at the tunnel periphery is 2.2 (i.e., rock is far from failure).

8.7.3 In-plane displacements

At the DFOS section, the left tunnel side displaces in all directions more than the right tunnel side (cf. Fig. 8.8, Tab. 8.7a, and Fig. 8.9c). In tunnel sections before the DFOS section, it is often also the opposite regarding the horizontal and vertical displacements. The in-plane displacements strongly depend on the stiffnesses and strengths of geological features at the particular chainage (cf. [415, p. 63]); but also on the shape of the excavation, on the support (in particular on its degree of asymmetry), and on the primary stresses. Now here, at the beginning, immediately after the shotcrete has been applied to the rock surface, the lining feet are not in contact with the open (i.e., unsupported) top-heading invert. With ongoing deformation of the surrounding rock mass, the size of the cavity reduces and the lining is compressed to some extent. Because the lining is much stiffer than the rock mass, and as long as the ring is not closed, the lining is forced to shear along the excavation boundary. The tunnel walls need to displace downwards. Because of the curved shape of the side walls, they also displace towards the cavity. At any one moment, the lining feet may touch or squeeze into the rock mass. Further shearing of the lining along the excavation boundary but also vertical displacements of the top-heading invert contribute to the inward displacement of the lining feet. Note that at the DFOS section but also in analysed sections before and ahead, one of the side walls always displaces vertically more than the crown $(|V_{\text{MT1}}| \max (H_{\text{MT4}}; |H_{\text{MT5}}|)| < 1$; cf. Tab. 8.7a); the same applies to the horizontal displacement of the side walls compared to the vertical displacement of the crown $(V_{\text{MT1}}/\max(V_{\text{MT4}}; V_{\text{MT5}}) < 1)$. ([267, p. 6])

With simple UDEC ([176]) simulations, [200, Tab. 2, p. 4] could show that the side walls can displace radially more than the crown even if the primary stresses are hydrostatic. The considered excavation profile is identical to the one of the top heading in the tunnel section evaluated here. The side walls are rather high and the roof arch is short (cf. Fig. 8.5 on p. 180), and the top-heading invert remains unsupported. The excavation profile and the support are asymmetric regarding any horizontal plane. In the UDEC simulations where parts of the rock mass surrounding the tunnel yield, a larger zone yields below the unsupported top-heading invert than above the supported crown. The displacing invert drags the top-heading lining feet towards the cavity ([200, p. 4]). Circumscribing the top-heading excavation profile with a vertical ellipse (axial ratio equals 1.13), for the plastic case 'p2_a' in [200], with $k_0 = 1$, the maximum elastic tangential stress according to Bray's equations (cf. Section A.6 on p. 320 in the appendix) results above the crown with -8.8 MPa (compression). The rock mass strength is 2.6 MPa. Thus, the absolute value of the minimum strength-stress ratio is approx. 0.3. In the simulation case with a shotcrete lining and radial rock bolts, the ratio of the radial displacement of the crown to the radial displacement of the side walls results in 0.77.

The displacement characteristics of the lining in the tunnel section evaluated here are similar. The ratio of the vertical displacement of the crown to the maximum horizontal displacement of the side walls is always below 1 (cf. text above). At the DFOS section, it is 0.7 and, thus, very close to the value from the UDEC simulation. Considering an overburden stress of -3.4 MPa, the same axial ratio of the ellipse, and $k_0=1$, the elastic tangential stress above the crown is -7.7 MPa. Using an average rock strength of 2.5 MPa, the absolute value of the minimum strength-stress ratio is 0.32 (i.e., extensive yielding must be assumed to occur). If $k_0 > 1$, then the displacement ratio is even lower (cf. Tab. 2 in [200, p. 4]). Increased horizontal stresses can be a reason for the lower displacement ratio in some sections before and ahead of the DFOS section.

Anyway, also weakness planes like foliation planes strongly determine the in-plane displacements. [92, Fig. 59, p. 66] (introduced in Section 8.7.2 on p. 183) shows that the right side wall displaces radially slightly more than the left side wall in case the foliation planes steeply dip against the DOD and to the left. At the DFOS section, most foliation planes dip to the right and the left side wall displaces horizontally more than the right one.

[200] got similar results when simulating a top-heading drive in FLAC3D ([177]). The cross section is identical to the one in the UDEC simulations (cf. text above) and of the DFOS section. The overburden stress is -3.6 MPa, the rock mass strength is 1.7 MPa, the elastic tangential stress above the crown is -8.3 MPa, and the absolute value of the strength-stress ratio results in 0.2. Considering the foliation planes, which strike sub-parallel to the tunnel axis and dip against the DOD and to the right at a moderate angle, with $k_0 = 1$ and using the Ubiquitous Joint model, the left side wall displaces radially more than the right side wall (cf. Fig. 2 in [200, p. 5]). Anyway, when considering a rotated, anisotropic stress state ($k_{0,h} = 0.8$, $k_{0,H} = 1.2$; σ_H deviates to the left by 24° from north with north = DOD), the trend reverses: the right side wall displaces more than the left one. Note that the orientation of the principal horizontal stresses here and at the DFOS section is similar (cf. Fig. 8.2 on p. 171). However, this example and evaluations above highlight that lots of factors determine the final displacement characteristics.

8.8 Observed system behaviour: DFOS

When studying results and graphs cited in this section, recall the location of the DFOS cables in the shotcrete lining plotted in Fig. 8.6 (p. 181).⁴ Further note that variations in the local conditions along the DFOS cables can cause an inhomogeneous strain pattern. Such variations can, for example, relate to ([266, p. 7])

- the shotcrete mix and structure,
- the bond between the DFOS cable and the surrounding shotcrete material, or
- the interaction between the different protection layers of the sensing cable.

Recorded maxima and minima may relate, e.g., to the fixation of the DFOS cables to the wire mesh, to inhomogeneities mentioned above, or to cracking of the shotcrete.

The strain within the shotcrete lining results because of mechanical loading as the rock mass deforms and because of temperature changes, but also because of shotcrete-specific effects like shrinkage or creep. Without a proper material model for the shotcrete, it is not possible to tell the share of each effect. Interpretations in the following sections focus on the mechanical loading.

⁴Because of the revision of the positioning of the DFOS cables, plots in this section may slightly differ from plots in previous publications (i.e., in [266, 267, 415, 416]). Chapter C.3.14 (p. 497) in the appendix evaluates the revised positioning.

8.8.1 Strain in the circumferential and longitudinal direction

Fig. 8.10 plots the <u>strain in the circumferential direction</u> (i.e., perpendicular to the tunnel axis) along the cable 'circ' within the rock-side layer of the shotcrete lining (cf. left developed top view in Fig. 8.6 on p. 181) for six distinct moments after the reference measurement. Most parts of the rock-side layer are compressed at all moments. The central part (i.e., between the shoulders) is compressed most. At early stages, some points at the side walls experience tension. The strain pattern is approximately symmetric around the y-axis. Note that eight hours pass between the end of the excavation of round i (cf. Fig. 8.7 on p. 182) and the reference measurement (cf. Tab. 8.2 on p. 177). The strain developing during this time is missing in the plot.

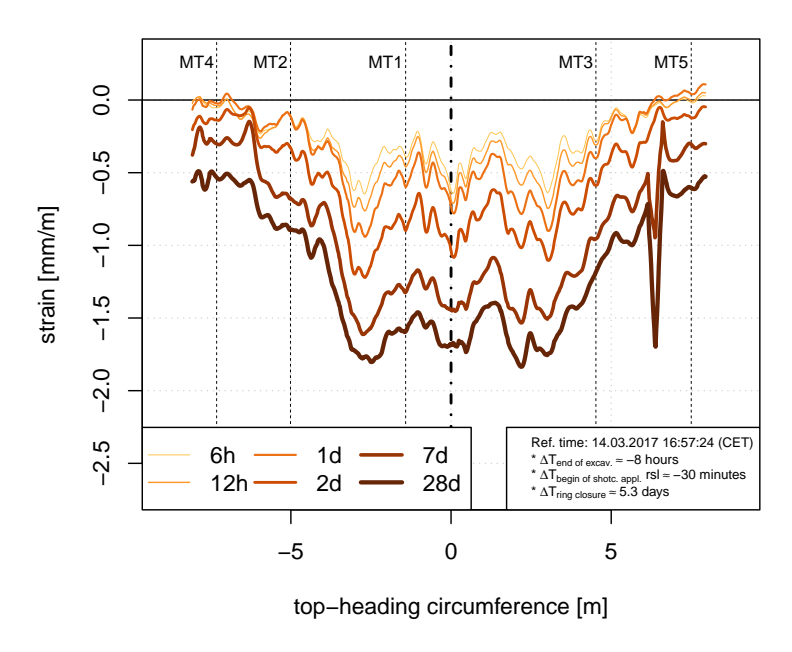


Figure 8.10: DFOS section | top heading | rock-side layer (rsl): Strain in the circumferential direction of the DFOS cable 'circ' (cf. left developed top view in Fig. 8.6 on p. 181) at $\{0.25; 0.5; 1; 2; 7; 28\}$ days after the reference measurement at the rock-side layer. Negative strain: compression; positive strain: elongation.

Fig. 8.11 is a similar plot for the cable 'circ' within the cavity-side layer (cf. right developed top view in Fig. 8.6). The moments plotted relate to the reference measurement of the DFOS cables at the rock side.⁵ This allows for a direct comparison of Fig. 8.10 and Fig. 8.11. Note that approx. 19 hours pass between the end of the excavation of round i and the reference measurement of the DFOS cables at the cavity side (cf. Tab. 8.2). In the meantime, top-heading round i+1 is excavated. This results in additional deformation the rock-side layer must fully cope with (cf. strain at 6h in Fig. 8.10) but the cavity-side layer only partly (this applies also to the longitudinal direction; cf. text below). Thus, overall, the cavity-side layer is less stressed than the rock-side layer (cf. also the figures in Section 8.8.2 on p. 190). Still, strain at the cavity side is small at the beginning (cf. strain at 12h in Fig. 8.11) but increases fast in the following days. Consider that the installation of the cavity-side layer results in a shift of the neutral axis of the lining (cf. text below). At the cavity side, the strain pattern is non-symmetrical. The largest compression occurs to the left of the monitoring target MT1. However, overall, the right tunnel side is compressed more than the left tunnel side. Like for the rock-side layer, at the beginning, some points at the side walls experience tension. As soon as the ring is closed (cf. legend text in

 $^{^5}$ Subtract 11 hours from the moments given in Fig. 8.11 to get the moments relating to the reference measurement at the cavity side (e.g., 12-11=1 hour).

the graph), also the side walls get significantly compressed; at the rock side and at the cavity side. Exception here is the left side wall at the cavity side.

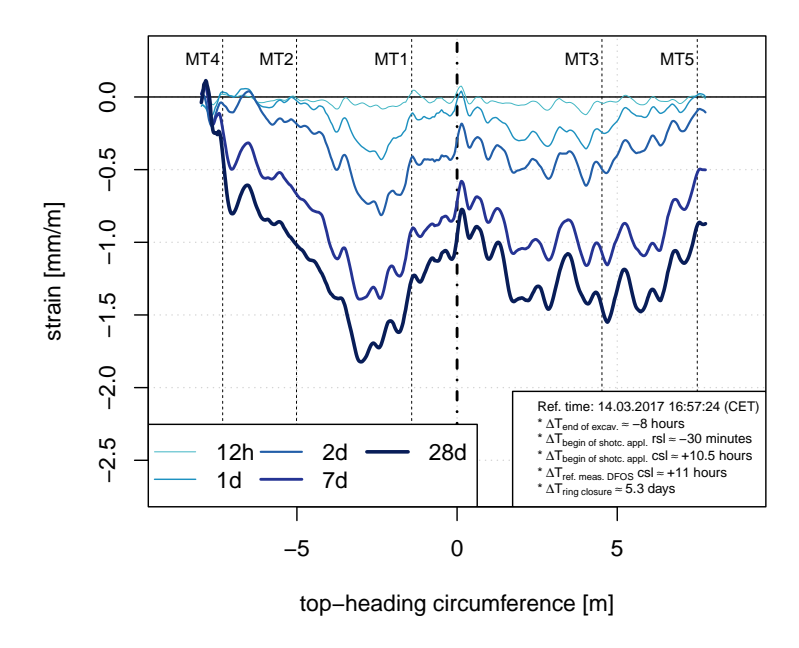


Figure 8.11: DFOS section | top heading | cavity-side layer (csl): Strain in the circumferential direction of the DFOS cable 'circ' (cf. right developed top view in Fig. 8.6 on p. 181) at $\{0.5; 1; 2; 7; 28\}$ days after the reference measurement at the rock-side layer (rsl). For the time difference between the reference measurement at the rock-side layer and at the cavity-side layer, refer to Tab. 8.2 (p. 177). Negative strain: compression; positive strain: elongation.

That the top-heading lining feet experience compression even before ring closure shows that both ends of the lining have a good contact with the rock mass and that they contribute to the overall resistance of the system ([267, p. 5]).

Fig. 8.12 plots the strain in the longitudinal direction (i.e., parallel to the tunnel axis) along the cable 'long' within the rock-side layer and along the cable 'long2' within the cavity-side layer. Here, too, the moments plotted relate to the reference measurement of the DFOS cables at the rock side. Overall, at the rock and cavity side, the left tunnel side experiences more compression than the right side. Below the right shoulder, even at later stages, some DFOS points experience tension. To the left of the right shoulder, at the cavity-side layer, the largest increase in compression occurs between the first and the second plotted epoch. During this time, round i+2 of the top heading and the round after are excavated (cf. Tab. 8.2 on p. 177). To the right of the right shoulder, the top-heading advance (and shrinkage, creep, etc.) results in an increase in tensile strain. Otherwise, compression increases most when the bench/invert heading approaches and passes the DFOS section during which also the ring is closed. Note that the right side wall displaces longitudinally much less against the DOD than the left side wall (cf. bottom graph in Fig. 8.8 on p. 182). This may be the reason for less compression (or even tension) in the longitudinal direction at the right side wall. Here, at some points and at some moments, elongating effects outweigh compressing effects.

Looking at all three graphs in this section, it gets clear that the magnitude (or range) of compressional strain is similar in the circumferential and longitudinal direction, both at the rock-side and cavity-side shotcrete layer.

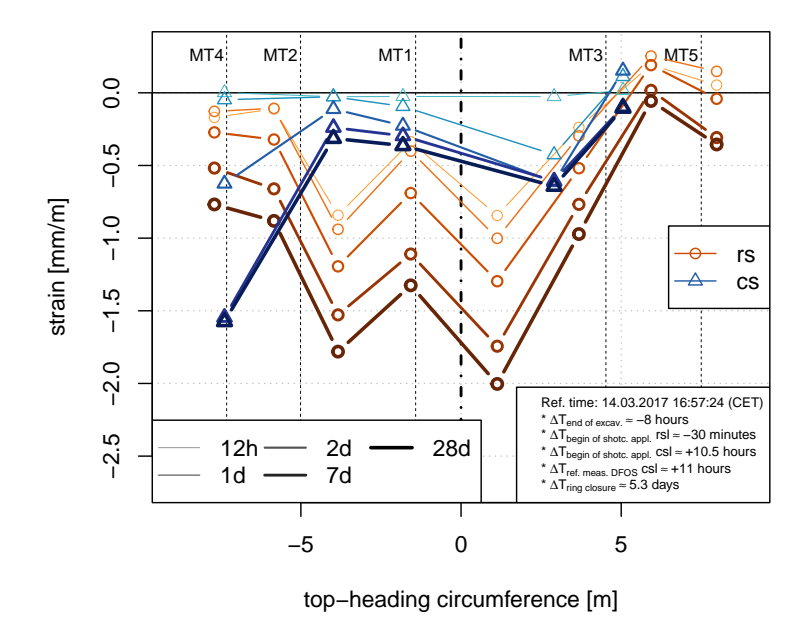


Figure 8.12: DFOS section | top heading: Strain in the longitudinal direction of the DFOS cables 'long' at the rock-side layer (rsl) and of the DFOS cables 'long2' at the cavity-side layer (csl) at {0.5; 1; 2; 7; 28} days after the reference measurement at the rock-side layer. Evaluation points at the rock-side layer: L1, L3, L5, L7, L9, L11, L13, L15. Evaluation points at the cavity-side layer: L1b, L3b, L5b, L7b, L9b. For the location of the cables and of the evaluation points, refer to Fig. 8.6 (p. 181). Negative strain: compression; positive strain: elongation.

The cause of having more compression in the longitudinal direction and less compression in the circumferential direction at the left tunnel side may be its large displacement in the longitudinal direction against the DOD (cf. Fig. 8.8c). The longitudinal displacement of the left side wall differs significantly from the displacement of the other monitoring targets beginning approx. with day 1 after the reference measurement. At the same moment, the compression of the left side wall in the longitudinal direction increases disproportionately (cf. Fig. 8.12). Whereas overall the compression of the lining in the circumferential direction increases as the heading of the top and bench/invert continues, the increase is less pronounced at the left tunnel side. There, the large displacement in the longitudinal direction results in an increase in the compression in the longitudinal direction but in a relative decrease in the compression in the circumferential direction.

Note that the left tunnel side displaces most also in the vertical direction (cf. Fig. 8.8b). Both the increased displacements in the longitudinal and in the vertical direction are due to the orientation of the foliation planes in rock masses near the DFOS section (cf. Section 8.7.2 on p. 183 and Section 8.7.3 on p. 185), at least for some part.

The resulting lining behaviour, in particular of the side walls, depends on the deformation of the top-heading lining feet prior ring closure, and on the characteristics of the connection of the feet with the bench/invert-heading lining (e.g., eccentricity of the neutral axes). [366, 367, 381] discuss on the problem and give suggestions for constructional improvements.

Consider also that the shotcrete of the rock-side layer is already 11 hours old when the cavity-side layer is installed. A stiffness contrast exists between the two layers from the beginning on. The contrast decreases with ongoing ageing. It is largest at early ages and determines the depth of the stiffness neutral axis and the bending stiffness. The cavity-side layer is in direct contact with the tunnel environment and probably more subjected to variations in temperature and humidity. It probably also dries up faster. Inhomogeneous conditions arise locally because of

the heat of engines and exhaust gases of any machinery, and also because of the air supply. In contrast, the rock-side layer may dry up much slower because the surrounding rock mass provides for water. Differences in thermal strain, creep, shrinkage, and swelling must arise. Many effects interact, some may compensate for each other. Considering that the initial curvature of the built lining deviates from the design, and that also some rock bolts installed perform better than others—depending on the geological conditions and the quality of installation—, local variations in the bending and, thus, in the change of the curvature (cf. Fig. 5 in [267, p. 7]) and in the shortening or elongation of the individual shotcrete layer result.

Anyway, it is assumed that, in general, the lining is compressed in the circumferential direction because the cavity size decreases with ongoing rock mass deformation. The top-heading lining feet can displace more freely than the central part of the lining as long as the ring is not closed. The tunnel side walls relax in compression to some extent as the rock mass shears along them, dragging them downwards (cf. description of the system behaviour in Section 8.7 on p. 181).

When evaluating strain in two directions perpendicular to each other (e.g., in the circumferential and longitudinal direction of a tunnel lining), it must be considered that compression in one direction causes an elongation in the other direction, and vice versa. If the deformation is fully or partly restrained by, for example, the bonding with the surrounding rock mass, or by adjacent lining segments, stresses increase. Changes in stress, however, alter the creep characteristics and, thus, the deformational behaviour of the shotcrete.

In the DFOS section, the foliation planes dip to the right and against the DOD (cf. Section 8.2 on p. 170). At the right tunnel side, considering the orientation of the foliation planes, shearing along those planes towards the cavity can only direct upwards and against the DOD ([267, p. 6]). At the left tunnel side, shear direction is downwards and in the DOD. Thus, at the right side, any shearing favours compression of the lining in the circumferential direction but elongation in the longitudinal direction. At the left side, it rather favours elongation in the circumferential direction and compression in the longitudinal direction. Fig. 8.10–8.12 support this hypothesis. Compression in the circumferential direction is larger at the right side. It is larger in the longitudinal direction at the left side.

Bending of the side walls about an axis at the cavity side parallel to the tunnel axis probably reduces compression or even increases tension of the rock-side shotcrete layer, and increases compression of the cavity-side layer. This either intensifies effects mentioned in previous paragraphs, or it compensates some of them.

As soon as the ring is closed, the system can bear higher loads with little deformation. The reduction in the degrees of freedom results in a stiffer response and, overall, in an increase in compression, both in the circumferential and longitudinal direction. With the closure of the supporting ring, the pattern of strain increments is more homogeneous ([267, p. 9]). Note that the latter can occur only if the lining remains more or less intact.

Finally, the bending in the circumferential direction is quite large close to the left shoulder and above the right side wall (cf. Fig. 5 in [266, p. 7]). At the crown, the bending is almost zero. Here, the strain at the rock side and at the cavity side accumulate proportionately ([416, p. 5]). At 0 m of the top-heading circumference in Fig. 8.10 and in Fig. 8.11, between the moment 12h and 28d, both at the rock and cavity side compression increases by approx. 1.1 mm/m.

8.8.2 Evolution of strain with time

Fig. 8.13 and Fig. 8.14 plot the evolution of the strain of selected evaluation points along the cables in the rock-side layer and in the cavity-side layer, respectively, with time. For the positioning of the evaluation points, refer to Fig. 8.6 (p. 181).

First, much of the strain (tension, or compression) already occurs within the first days after shotcrete application. At some evaluation points, the strain value exceeds 50% of its maximum value within the first 24 hours (cf. Fig. 8.13b and Fig. 8.14b). At the end of the initial continuous monitoring campaign, all evaluation points experience compression (i.e., negative strain values; cf. Fig. 8.13a and Fig. 8.14a). Of the selected evaluations points, at the rock side, the points C10f (in the circ. dir., to the right of the crown), C6f (in the circ. dir., to the left of the crown), and L9 (in the long. dir., to the right of the crown) are compressed most. In the cavity-side layer, it's C4f, C4C, and C4b, all in the circ. dir. and all between the crown and the left shoulder. Anyway, the difference in strain of those three points compared to other points in the cavity-side layer is not that large. The point L13 at the rock side and the point L9b at the cavity side, both being above the right side wall, are compressed least (in the long. dir.). From all DFOS points, not only those highlighted in Fig. 8.6 (p. 181), a point at the rock side next to L9 after the loop towards C10f (to the right of the crown) is compressed most featuring a strain value of -2.72 mm/m at approx. 35.5 days after the reference measurement.

At the rock and cavity side, the accumulating tensile strains are similar in magnitude. Of the evaluation points at the rock side, maximum tensile strain occurs within the first 20 hours. At the cavity side, it's within the first 38 hours; each after the reference measurement of the individual layer. From all DFOS points, a point at the rock side next to L11 after the loop towards C10f (to the right of the crown) elongates most. It features a strain value of 0.47 mm/m at approx. 1.1 days after the reference measurement. Of the selected evaluation points, they show tensile strain (if any) mostly up to 1.8 days after the reference measurement at the rock side and up to 0.9 days at the cavity side. Exceptions are the point L13 at the rock side with tension up to 8 days after the reference measurement, and the points C2f and L9b at the cavity side up to 2.2 days.

[416, p. 5] analysed the accumulation of strain within three months after the reference measurement with a follow-up measurement (single reading approx. two months after the initial continuous monitoring campaign). The increase in strain was up to 0.1 mm/m. This shows that local failure and related stress redistribution within the rock mass were still ongoing. Measurement data from the strain gauges suggest that the lining reaches its final deformation state approx. 200 days after the excavation of the DFOS section by the top heading.

The following subsections give some more interpretations of the system behaviour.

More compression in the circumferential direction than in the longitudinal direction?

Comparing the strain values of {Li; Cib} pairs at the rock side (DFOS points of the 'circ' cable and of the 'long' cable are very close to each other; cf. left developed top view in Fig. 8.6 on p. 181) shows that compression in the circumferential direction is not necessarily larger than in the longitudinal direction. At the left side wall, close to the left shoulder, and to the right of the crown, compression at the end of the initial monitoring campaign (i.e., approx. 35 days after the reference measurement) is larger in the longitudinal direction. Otherwise, it is larger in the circumferential direction. A similar comparison of strain values of {Lib; Cif} pairs at the cavity side (cf. right developed top view in Fig. 8.6) reveals that only at the left side wall the compression is larger in the longitudinal direction. At all other pairs, it is, again, larger in the circumferential direction. Longitudinally, the left tunnel side displaces more against the DOD than the right side (cf. Section 8.7.2 on p. 183). Analysing the displacement of the monitoring targets at the DFOS section relative to the displacement of the targets at the monitoring cross section approx. 10 m behind shows that the targets approach each other in the longitudinal direction (not shown). Thus, the lining section between is compressed. The shortening is largest at the left side wall ($|\Delta L_{max}| = 9 \text{ mm}$).

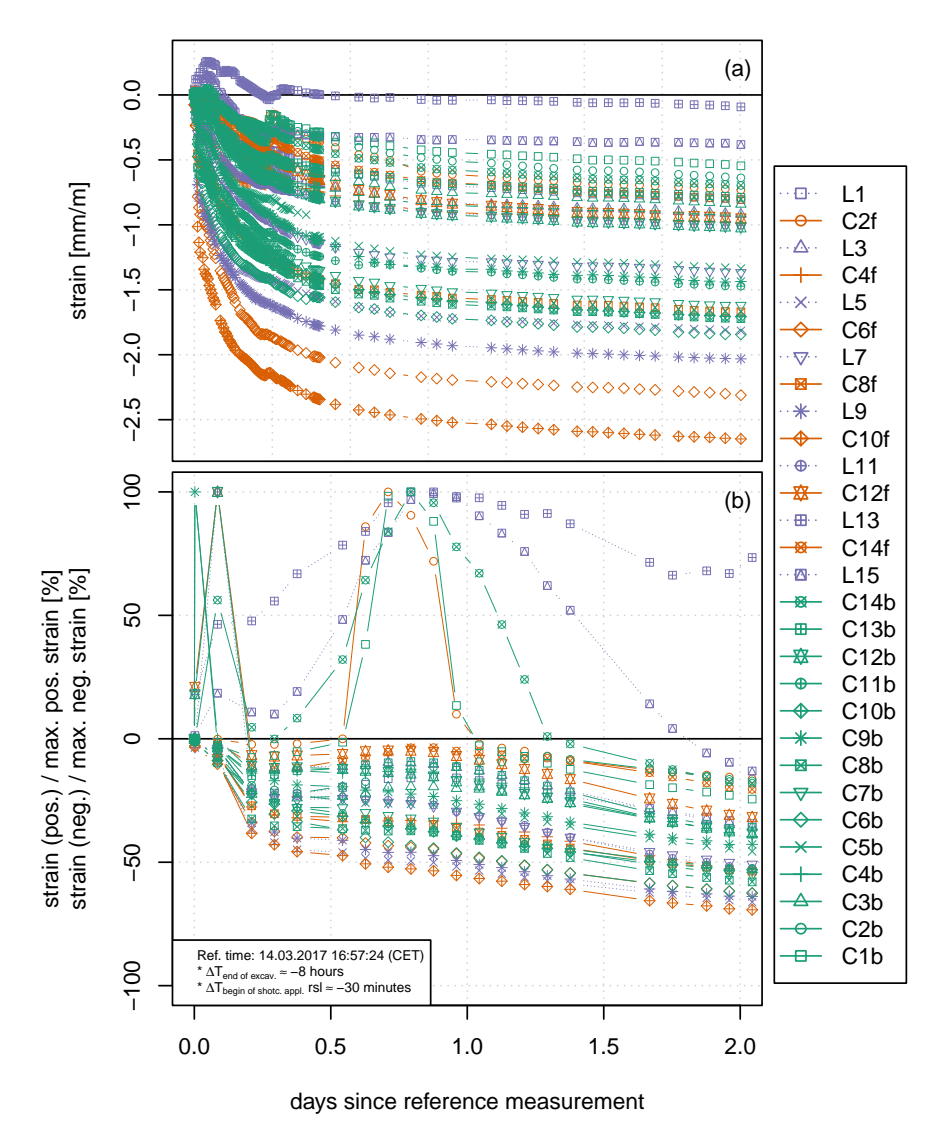


Figure 8.13: DFOS section | top heading | rock-side layer (rsl): Evolution of the strain at selected evaluation points (cf. left developed top view in Fig. 8.6 on p. 181) with time. (a) absolute strain; (b) ratio of the positive (negative) strain (cf. graph (a)) to the maximum positive (negative) strain that has developed within 35 days after the reference measurement.

Bending in the longitudinal direction

Three pairs of evaluation points allow for an assessment of the bending in the longitudinal direction (i.e., about the horizontal in-plane axis) because points are close to each other. It's {L1; L1b} (left side wall), {L5; L3b} (above the left shoulder), and {L7; L5b} (to the left of the crown). The first point of each pair is at the rock side, the second point at the cavity side. The cable segments along which the points are align parallel to the tunnel axis (cf. Fig. 8.6 on p. 181). Of points at the rock side, only strain is considered which accumulated since the reference measurement at the cavity side. At the left side wall, the cavity-side layer compresses longitudinally more than twice as much as the rock-side layer. Thus, the lining bends about an in-plane axis at the cavity side tangential to the side wall. This complies well with the fact that the targets at the DFOS section displace horizontally less than the targets approx. 10 m behind ($|\Delta H_{max}| = 25$ mm at the side walls; not shown). Anyway, between the left side wall and the crown the situation is completely different. Here, the compression of the rock-side layer is approx. three times larger than of the cavity-side layer (but only two-thirds of the compression

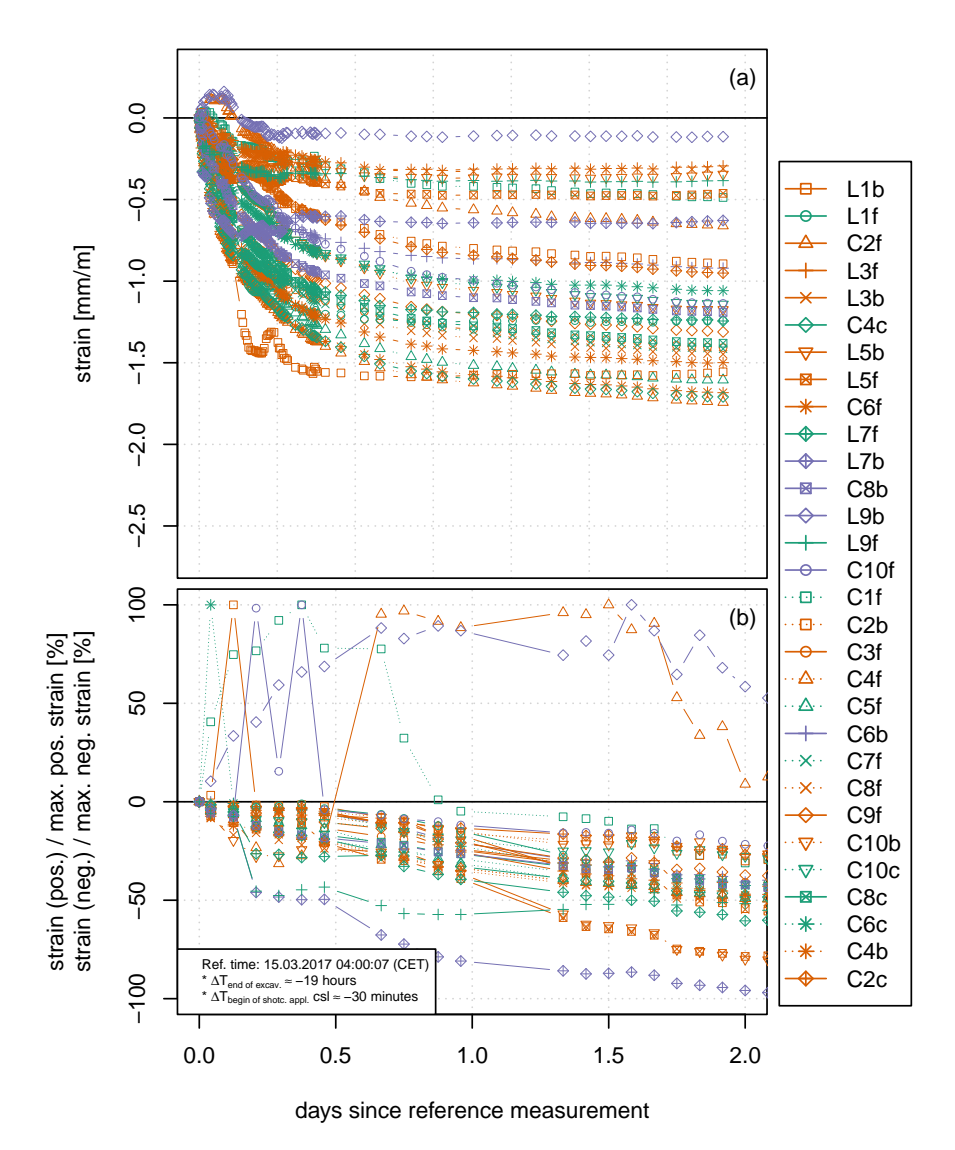


Figure 8.14: DFOS section | top heading | cavity-side layer (csl): Evolution of the strain at selected evaluation points (cf. right developed top view in Fig. 8.6 on p. 181) with time. (a) absolute strain; (b) ratio of the positive (negative) strain (cf. graph (a)) to the maximum positive (negative) strain that has developed within 35 days after the reference measurement.

of the cavity-side layer at the side wall). The lining bends about an in-plane axis at the rock mass side tangential to the tunnel roof. And this does not comply with the relative displacement of the monitoring cross sections. The targets at the DFOS section displace vertically more than the targets approx. 10 m behind (left tunnel side: $|\Delta V_{max}| = 23$ mm; right tunnel side: $|\Delta V_{max}| = 11$ mm). This discloses the disadvantage of a large distance between monitoring cross sections. Much of what happens between them is not monitored. A possible scenario is that the lining in the DFOS section displaces as a whole vertically more than the lining in sections farther behind, but locally it forms a trough (e.g., in the longitudinal direction between two lattice girders). That the cavity-side layer is compressed more in the longitudinal direction along cable segments which are farther ahead in the DOD (cf. next subsection) supports this hypothesis.

More compression at the front than at the back?

Four pairs of evaluation points on each side allow to address the question whether the rear part of the lining is compressed more in the circumferential direction. The points of a pair feature

approx. the same angular coordinate along the top-heading circumference and approx. the same radial coordinate, but one point is considerably farther ahead in the DOD.

At the rock side, it's {C2f; C2b} (above the left side wall), {C6f; C6b} (above the left shoulder), {C10f; C10b} (above the right shoulder), and {C14f; C14b} (above the right side wall). The distance between the points at the front (Cif) and the points at the back (Cib) ranges between 0.54 m and 0.65 m. At all pairs, the points farther ahead experience more compression. Above the shoulders, the absolute difference is {0.47; 0.94} (in millimetre per metre). Between the shoulders and the side walls, it is {0.09; 0.11} (in millimetre per metre).

At the cavity side, it's {C2f; C2b} (between the left side wall and the left shoulder), {C6f; C6b} (to the right of the crown), {C8f; C8b} (above the right shoulder), and {C10f; C10b} (between the right side wall and the right shoulder). The distance of the points in the longitudinal direction is approx. 1.44 m, except for {C8f; C8b} where it is 0.34 m. Here, only the pair at the left tunnel side experiences more compression at the back (the absolute difference is 0.23 mm/m). The pairs at the right tunnel side show more compression at the front (cf. also Fig. 9 in [266, p. 11]). The absolute difference ranges between 0.04 mm/m (close to the side wall) and 0.58 mm/m (close to the crown).

Overall, the front part of the lining compresses in the circumferential direction more than its rear part. Consider here that the rear part is connected with older lining segments behind, which feature already a higher stiffness. In contrast, the front part is closest to the tunnel face and to new excavations and must cope with redistributed stresses more or less alone. At the beginning, before the lining segments of rounds ahead are installed, because the ring is not closed, the lining segment closest to the tunnel face acts like a cantilever with the old lining segments behind being the fixation.

In the longitudinal direction, five point pairs at the cavity side are evaluated. It's {L1b; L1f} (left side wall), {L3b; L3f} (above the left shoulder), {L5b; L5f} (to the left of the crown), {L7b; L7f} (to the right of the crown), and {L9b; L9f} (below the right shoulder). The points of each pair are 0.63 m apart from each other. At the left side wall, the rear part compresses more in the longitudinal direction (the absolute difference is 0.31 mm/m). At the left shoulder, the compression at the back and at the front is similar. At all other pairs, the front part compresses more. The absolute difference ranges from 0.12 mm/m to 0.62 mm/m.

Remember from the previous subsection that at the DFOS section, the side walls displace horizontally less than at the section 10 m behind. Assuming that the lining at the left side wall features a deformed shape in the longitudinal direction that follows a concave path starting tangentially at the DFOS section, the rear part of the cavity-side layer compresses more. This complies with the evaluated strain pair (cf. previous paragraph). In contrast, at the right side wall, the deformation path must be convex to have the front part compress more longitudinally. For the tunnel roof, it must be also convex, which supports the hypothesis of the trough (cf. previous subsection).

The evaluations here highlight that strain values can differ strongly depending on the location of the DFOS point in the circumferential and longitudinal direction.

8.8.3 Strain rate

Fig. 8.15 plots the evolution of the strain rate of all DFOS points at the rock side with time. A few distinct peaks exist. Interestingly, not all peaks of the cable 'circ' (cf. Fig. 8.15a) are visible in the graph for the cable 'long' (cf. Fig. 8.15b). The first peaks exist at the moment of the reference measurement and within three hours after. The increased strain rate at the beginning

must be because of the ongoing deformation of the rock mass as a result of the excavation of round i (i.e., the first round of the DFOS section). Compressive strain and tensile strain accumulate at different locations along both cables. Consider that a positive strain rate value in the graphs relates to a positive strain increment. This can be either an increase in tensile strain, or a decrease in compressive strain. A negative strain rate value relates to a negative strain increment (i.e., a decrease in tensile strain, or an increase in compressive strain). 1.8 hours after the reference measurement, miners start to excavate round i+1 (i.e., from chainage 1439.2 m to chainage 1440.2 m; cf. Tab. 8.2 on p. 177). At both cables, this results in a significant increase in the compressive strain rate. Note here that the peak is only on the negative side of the y-axis in both graphs. Anyway, this does not imply that no DFOS point experiences tension (or relaxation in compression). No significant increase in the strain rate occurs approx. 13 hours after the reference measurement when the excavation of the top-heading round i+2 starts. The next significant peaks occur after four days. They exist only at the cable 'circ'. 4.7 days after the reference measurement, the bench/invert heading continues at chainage 1435.2 m. The heading has excavated round i of the DFOS section approx. 4.3 hours later. After the installation of the DFOS devices and after the ring closure, then bench/invert heading continued.

Taking the average values of the strain rate, that is $\{-7.4; -10.4\}$ (in micrometre per metre and hour) on the compression side (cf. legend text for compression in Fig. 8.15), and multiply them with 192 hours (= 8 days; period used to calculate the statistical values), then compressive strain of $\{-1.42; -2.00\}$ (in millimetre per metre) result. Those values match with the evolution of strain of some DFOS points plotted in Fig. 8.13a (p. 192). Thus, maxima in Fig. 8.15 must be short-living. Anyway, strain rates are higher at the cable 'long', both on the compression and on the tension side. Most segments of the cable 'long' are located farther ahead in the DOD. Note that such maxima are probably very local features. Some may be due to the fixation or other unfavourable factors.

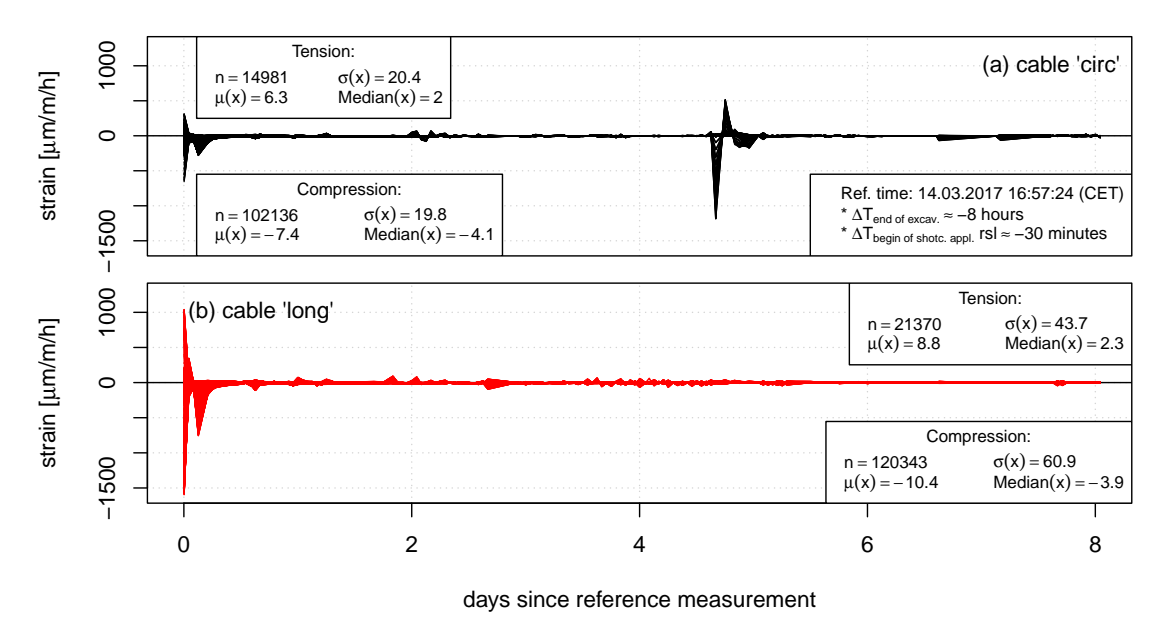


Figure 8.15: DFOS section | top heading | rock-side layer (rsl): Evolution of the strain rate within eight days after the reference measurement of all DFOS points of the cable 'circ' (a) and cable 'long' (b). For the location of the cables, refer to the left developed top view in Fig. 8.6 (p. 181).

At the cavity side (cf. Fig. 8.16), the reasons for peaks are similar. Approx. two hours after the reference measurement at the cavity side, top-heading round i+1 is excavated. The latter

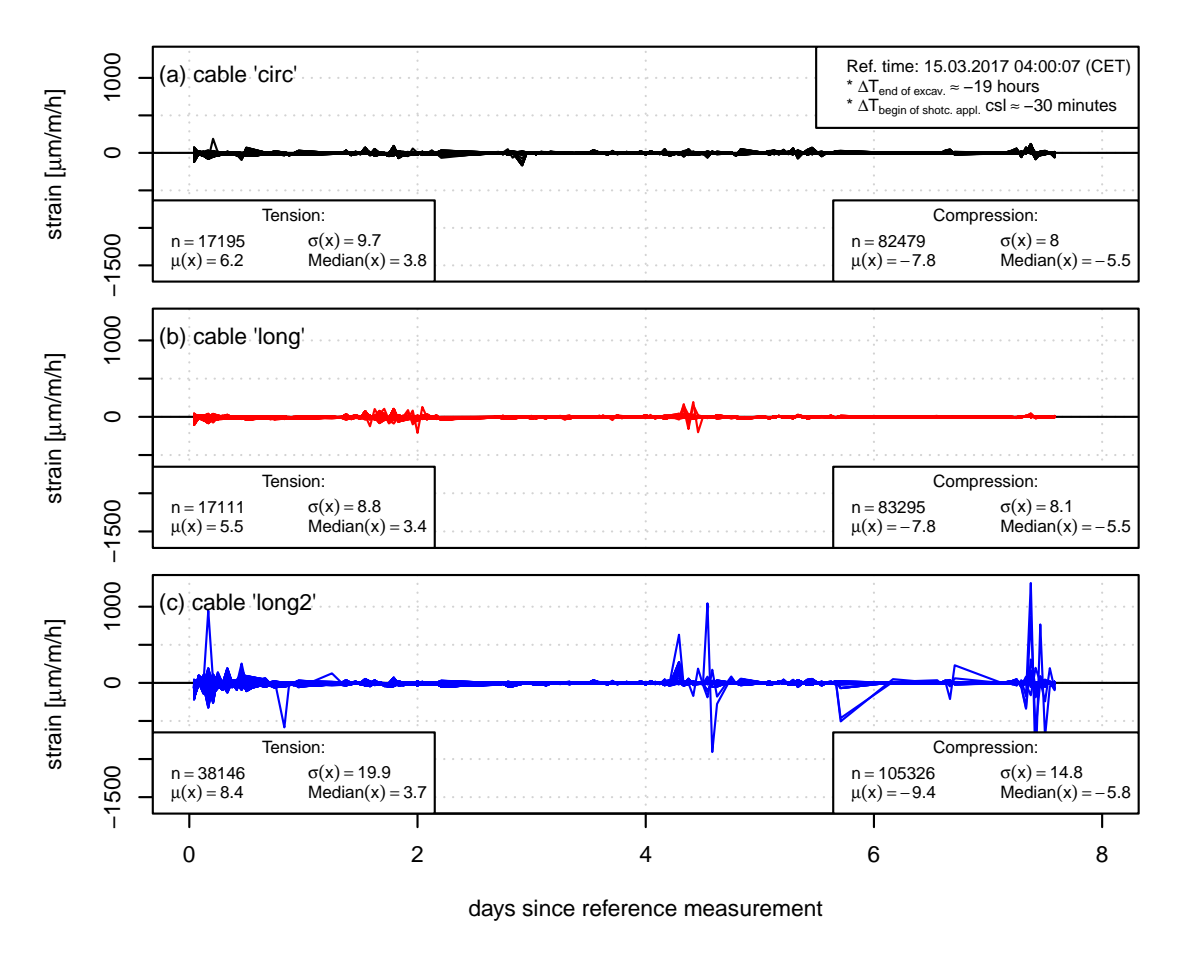


Figure 8.16: DFOS section | top heading | cavity-side layer (csl): Evolution of the strain rate within eight days after the reference measurement of all DFOS points of the cable 'circ' (a), cable 'long' (b), and cable 'long2' (c). For the location of the cables, refer to the right developed top view in Fig. 8.6 (p. 181).

causes peaks at the cavity side but not at the rock side (cf. previous paragraphs). Peaks are largest at the cable 'long2' which is located farthest ahead in the DOD (cf. Fig. 8.6 on p. 181). No event relates to the small peaks before and at day 2. The peaks after day 4 relate to the bench/invert heading. Again, no event relates to any of the peaks after day 5. Like at the rock side, cable 'long2' being farther ahead in the DOD shows higher average strain rate values. Average strain rates at the rock side and at the cavity side are similar in magnitude.

For some more detailed plots showing strain rate changes, refer to [416, Fig. 5 and 6, p. 6].

8.9 Observed system behaviour: Temperature

The strain gauges installed are of the type *GEOKON* 4200-7 (vibrating wire strain gauge). They are equipped with a thermistor for reading temperature ([126]). Fig. 8.17 plots the temporal evolution of the temperature within the top-heading shotcrete lining and the temperature in the tunnel at some moments. Some data from the strain gauges are missing at the beginning because of erroneous readings. Anyway, the curves of all strain gauges match well. The temperature of the first available readings ranges from 34 °C to 44 °C. Note that in the laboratory, the fresh shotcrete temperature is approx. 25 °C ([409]). Within approx. 10 days after the application of the individual shotcrete layer, the temperature decreases to the level of the ambient temperature of approx. 20 °C present in the tunnel.

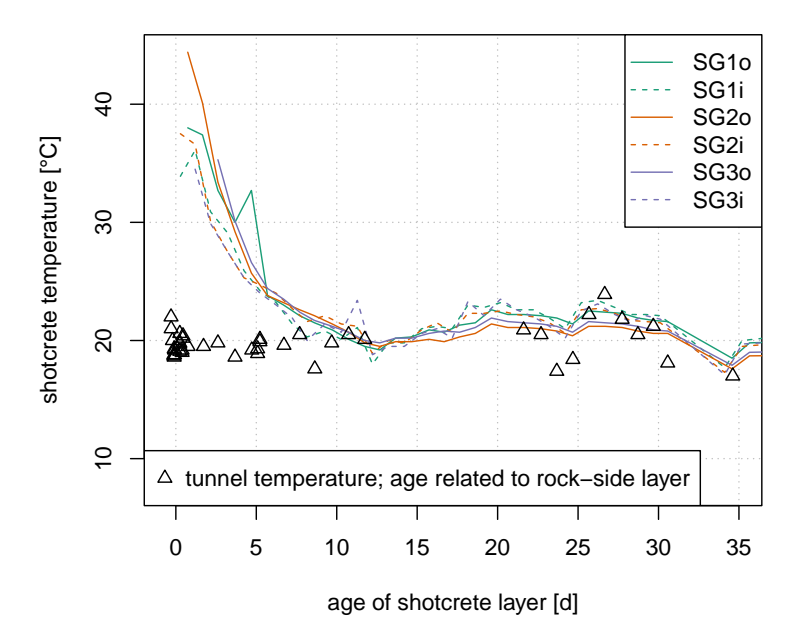


Figure 8.17: DFOS section | top heading: Evolution of temperature within the shotcrete lining with time. Shotcrete temperature data from strain gauges (SGix: o ... outer = rock-side layer, i ... inner = cavity-side layer). For the positioning of the strain gauges, refer to Fig. 8.6 (p. 181) and Fig. 8.5 (p. 180). Tunnel temperature data from hand-held meter.

This suggests that the development of hydration heat abates significantly within this period. From that moment on, the shotcrete temperature is determined mostly by the temperature of the surrounding media (cf. relation between tunnel temperature and shotcrete temperature in Fig. 8.17). Note that the cavity-side layer responds more and probably also faster to changes in the tunnel temperature. The cavity-side layer is kind of a thermal barrier for the rock-side layer.

Most times, also in the long term (not shown), the temperature in the cavity-side layer is higher than in the rock-side layer. Accordingly, the temperature of the rock mass (including pore water and circulating water) must be lower than the tunnel temperature. Note that at the beginning, the cavity-side layer helps the rock-side layer to keep the hydration heat and, thus, the overall temperature in the latter is higher. Because the rock-side layer is almost fully enclosed by either the rock mass or the cavity-side layer, it takes longer to balance the temperature. The decrease in the shotcrete temperature to less than 20 °C after 30 days is because of a construction stop for four days during Easter holidays (April 14th to April 18th).

The temperature evolution recorded with the thermistors in the strain gauges fits well with the temperature evolution from a DFOS system installed in a test slab made of shotcrete (cf. Fig. 8.18). This shotcrete slab with a thickness of 25 cm was made to test the applicability of the DFOS system, the same which was to be installed in the DFOS section in track 1 of the tunnel Gloggnitz. For details, refer to [415, Chapter 4, p. 12ff]. During the hardening of the shotcrete, the slab has not been loaded except for the temperature changes because of the hardening processes and changes in the tunnel temperature. The graphs in Fig. 8.18 suggest that the temperature in the shotcrete reaches its maximum in the top layer within one to four hours after shotcrete application, and in the bottom layer after approx. 10 hours. This complies with the statement by [368, p. 842f] that the maximum increase in hydration temperature occurs between nine and 12 hours after shotcrete application. They analysed data from [173] who investigated on single shotcrete samples. [85] (cited in [205, p. 42]) named a similar range of 10 to 15 hours for wet-mix shotcrete. The discontinuity in the bottom layer after approx. 2.8 hours is because of

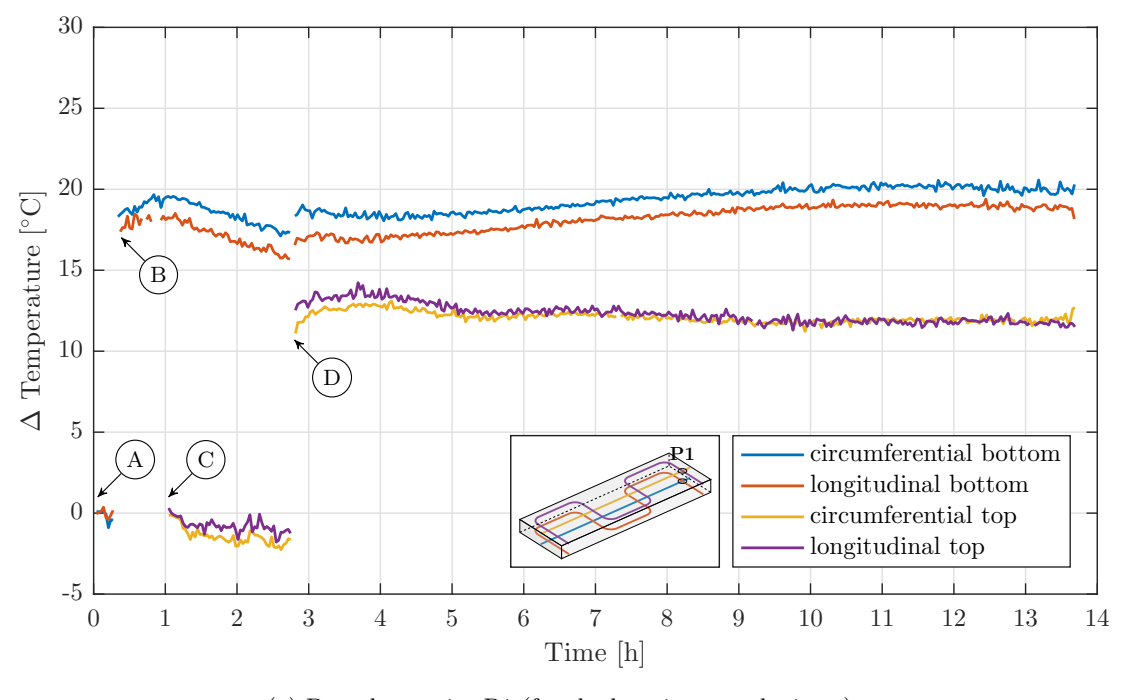
the application of the top layer. The latter applies heat to the former.

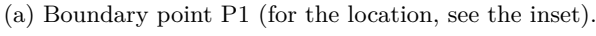
Like at the DFOS section within the first 10 days, at the test slab, the temperature in the rock-side (i.e., bottom) layer is higher than in the cavity-side (i.e., top) layer. P1 (Fig. 8.18a) is closer to another free slab surface than P2 (Fig. 8.18b). Thus, the temperatures at P1 are lower than at P2. The slab was manufactured on November 17th, 2016. On that day, the average temperature outside ranged from 3 °C to 5 °C ([425]). Consider that the slab was stored in the tunnel but close to its portal. So, one can assume that the tunnel temperature equals the outside temperature. The tunnel temperature in the DFOS section is approx. 15 °C higher than where the test slab was stored. Thus, relative to the temperature in the test slab, the maximum relative temperature in the shotcrete at the DFOS section must be also approx. 15 °C higher: maximum relative temperature of approx. 25 °C at P2 plus 15 °C yields 40 °C. This matches well with the first readings by the thermistors in the strain gauges plotted in Fig. 8.17. Hence, the recordings from the strain gauges and from the DFOS system seem to accord. The resulting values also match well with [388, p. 39] who states that during initial hydration, the temperature is typically between 30 and 45 °C. A maximum increase in the temperature of 25 °C is also reported by [205] (cited in [388, Tab. 2.7, p. 42]) for a 30 cm thick lining.

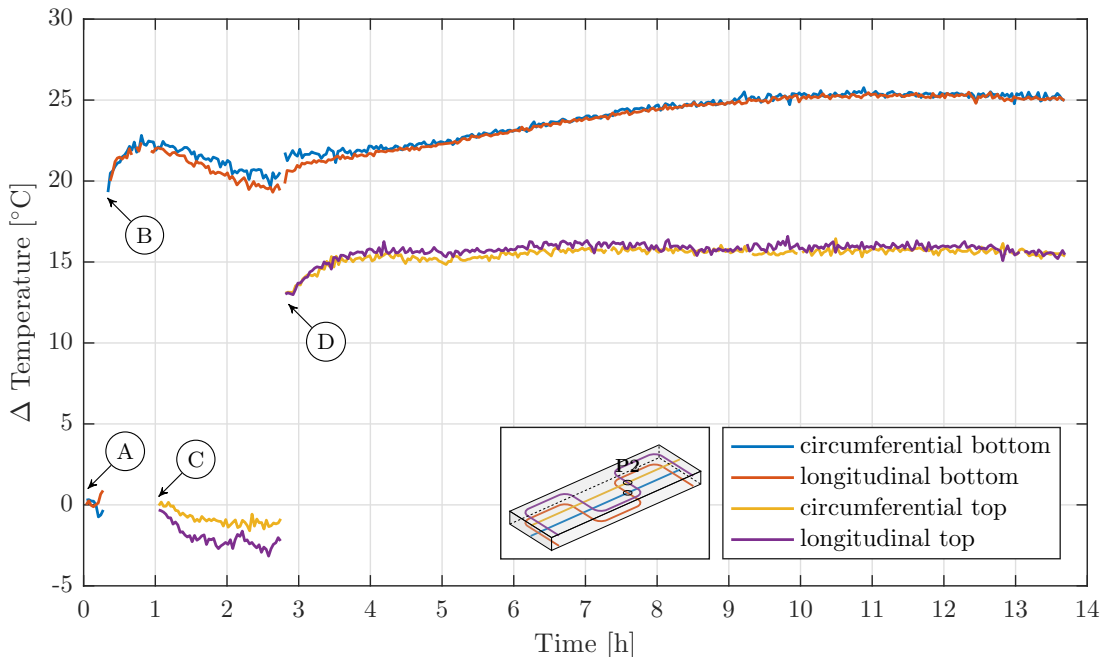
Existing differences in the relative temperature change between the test slab and the DFOS section are probably because of differences in the shotcrete mixture (test slab: SpC 25/30/J2/-XC4/RV0.7)⁶ and because the test slab features more free surfaces than lining segments in the tunnel.

Temperature data from a DFOS system installed in another shotcrete lining at the same construction lot the DFOS section is part of confirm the validity of the temperature data of the thermistors at the DFOS section. For details, refer to [159, 224].

⁶Minimum characteristic compressive strength $f_{ck,min}=25$ MPa for cores with h/d=1, early strength class J2, XC4 ... water penetration depth of <35 mm, RV ... reduced leaching behaviour. [289, p. 26ff]







(b) Central point P2 (for the location, see the inset).

Figure 8.18: Evolution of temperature with time during the hardening of a slab made of shotcrete (from [415, Fig. 4.6 and 4.8, p. 19f]). Moment ②: system check after the installation of the DFOS cables of the bottom (i.e., rock-side) shotcrete layer; moment ③: system check after the application of the bottom shotcrete layer; moment ③: system check after the installation of the DFOS cables of the top (i.e., cavity-side) shotcrete layer; moment ①: system check after the application of the top shotcrete layer, then start of continuous monitoring period.

Bibliography

- [1] Abler, P. Einflüsse auf das Verformungsverhalten von jungem Spritzbeton im Tunnelbau. Diploma thesis, University of Innsbruck, Innsbruck, Austria, 1992.
- [2] ACI. ACI Manual of Concrete Practice. Technical report, American Concrete Institute (ACI), 1978.
- [3] ACI Committee 209. 209R-92. Prediction of Creep, Shrinkage, and Temperature Effects in Concrete Structures. Technical report, American Concrete Institute (ACI), March 1992. Reapproved 1997.
- [4] ACI Committee 209. 209.1R-05. Report on Factors Affecting Shrinkage and Creep of Hardened Concrete. Technical report, American Concrete Institute (ACI), July 2005.
- [5] ACI Committee 209. 209.2R-08. Guide for Modeling and Calculating Shrinkage and Creep in Hardened Concrete. Technical report, American Concrete Institute (ACI), May 2008.
- [6] Acker, P. Comportement mécanique du béton: Apports de l'approche physico-chimique (Mechanical behavior of concrete: A physico-chemical approach). PhD thesis, Ecole Nationale des Ponts et Chaussées, Paris, France, 1988.
- [7] Acker, P. Micromechanical Analysis of Creep and Shrinkage Mechanisms. In Ulm, F.-J., Bažant, Z. P., and Wittmann, F. H., editors, Creep, Shrinkage and Durability Mechanics of Concrete and other Quasi-brittle Materials. Proceedings of the 6th International Conference CONCREEP@MIT, pages 15–26, Cambridge, USA, August 2001. Elsevier: Amsterdam.
- [8] Adhikary, D. P. Shortcomings in the standard continuum based implicit joint model of layered rocks. *Journal of Geology and Mining Research*, 2(2):23–28, May 2010.
- [9] Alber, M. and Kahraman, S. Predicting the uniaxial compressive strength and elastic modulus of a fault breccia from texture coefficient. *Rock Mechanics and Rock Engineering*, 42(1):117–127, January 2009.
- [10] Aldrian, W. Beitrag zum Materialverhalten von früh belastetem Spritzbeton. PhD thesis, Montanuniversität Leoben, Leoben, Austria, May 1991.
- [11] Allaby, M., editor. A Dictionary of Geology and Earth Sciences. Oxford University Press, 4th edition, January 2013.
- [12] Allmendinger, R. W. Stereonet, September 2020. URL https://www.rickallmendinger.net/stereonet. Last access: 26.09.2020.
- [13] Allmendinger, R. W., Cardozo, N., and Fisher, D. M. Structural Geology Algorithms: Vectors and Tensors. Cambridge University Press, December 2011.

BIBLIOGRAPHY 288 of 498

[14] ASTM. D5607-02. Standard Test Method for Performing Laboratory Direct Shear Strength Tests of Rock Specimens Under Constant Normal Force. Standard, 2002.

- [15] ASTM. D7012-10. Test Methods for Compressive Strength and Elastic Moduli of Intact Rock Core Specimens under Varying States of Stress and Temperatures. Standard, 2010.
- [16] Atkins, P., Jones, L., and Laverman, L. Chemical principles. W. H. Freeman and Company, 6th edition, 2013.
- [17] Atzl, G., Brandtner, M., Selan, V., and Moritz, B. Numerical analyses of deep tunnels driven through massive faults. In Schubert, W. and Kluckner, A., editors, *Proceedings of the ISRM Regional Symposium EUROCK 2015 & 64th Geomechanics Colloquium–Future Development of Rock Mechanics*, pages 877–882, Salzburg, Austria, October 2015. Austrian Society for Geomechanics.
- [18] Austin, S. A. and Robins, P. J., editors. Sprayed Concrete: Properties, Design and Application. Whittles Publishing, 1995.
- [19] Austrian Standards Institute. ÖNORM EN 14487-1-1:2006. Spritzbeton: Teil 1: Begriffe, Festlegungen und Konformität. Standard, May 2006.
- [20] Austrian Standards Institute. ÖNORM EN 1992-1-1:2015. Eurocode 2: Bemessung und Konstruktion von Stahlbeton- und Spannbetontragwerken Teil 1-1: Allgemeine Bemessungsregeln und Regeln für den Hochbau (konsolidierte Fassung). Standard, February 2015.
- [21] Aydan, O., Sezaki, M., and Kawamoto, T. Mechanical and numerical modelling of shotcrete. In Pande, G. N. and Pietruszczak, S., editors, Proceedings of the Fourth International Symposium on Numerical Models in Geomechanics (NUMOG IV), pages 757–764, Swansea, Wales, August 1992. Taylor & Francis, London.
- [22] Bandis, S. C., Lumsden, A. C., and Barton, N. R. Fundamentals of rock joint deformation. International Journal of Rock Mechanics and Mining Sciences & Geomechanics Abstracts, 20(6):249–268, December 1983.
- [23] Barbero, M., Bonini, M., and Borri-Brunetto, M. Numerical modelling of the mechanical behaviour of bimrock. In Ribeiro e Sousa, L., Olalla, C., and Grossmann, N., editors, Proceedings of the 11th Congress of the International Society for Rock Mechanics—The Second Half Century of Rock Mechanics, volume 1 & 2, pages 377–380, Lisbon, Portugal, July 2007. Taylor & Francis Group, London.
- [24] Barbero, M., Bonini, M., and Borri-Brunetto, M. Three-Dimensional Finite Element Simulations of Compression Tests on Bimrock. In Proceedings of the 12th International Conference of International Association for Computer Methods and Advances in Geomechanics (IACMAG), pages 631–637, Goa, India, October 2008.
- [25] Bažant, Z. P., editor. Mathematical Modelling of Creep and Shrinkage in Concrete. Wiley & Sons Ltd, New York, 1988.
- [26] Bažant, Z. P. Creep and thermal effects in concrete structures: a conceptus of some new developments. In Mang, H. A., Bicanic, N., and de Borst, R., editors, *Proceedings of the* Int. Conf. EURO-C "Computational Modelling of Concrete Structures", pages 461–480, Swansea, Wales, 1994. Pineridge Press.

BIBLIOGRAPHY 289 of 498

[27] Bažant, Z. P. Materials Science of Concrete IV, chapter Creep and Damage in Concrete, pages 335–389. American Ceramic Society, Westerville, USA, 1995.

- [28] Bažant, Z. P. and Panula, L. Practical prediction of time-dependent deformations of concrete. *Matériaux et Constructions*, 11(5):317–328, September 1978.
- [29] Bažant, Z. P. and Prasannan, S. Solidification Theory for Concrete Creep. I: Formulation. Journal of Engineering Mechanics, 115(8):1691–1703, 1989.
- [30] Bažant, Z. P. and Wittmann, F. H., editors. *Creep and Shrinkage in Concrete Structures*. John Wiley & Sons Ltd, Chichester, 1982.
- [31] Bažant, Z. P., Hauggaard, A. B., and Baweja, S. Microprestress solidification theory for concrete creep. II: Algorithm and verification. *Journal of Engineering Mechanics*, 123(11): 1195–1201, November 1997.
- [32] Bažant, Z. P., Hauggaard, A. B., Baweja, S., and Ulm, F.-J. Microprestress solidification theory for concrete creep. I: Aging and drying effects. *Journal of Engineering Mechanics*, 123(11):1188–1194, 1997.
- [33] Bell, F. G. Engineering Properties of Soils and Rocks. Butterworth-Heinemann Ltd: Oxford, 3rd edition, 1992.
- [34] Benz, T., Vermeer, P. A., and Schwab, R. A small-strain overlay model. International Journal for Numerical and Analytical Methods in Geomechanics, 33(1):25–44, January 2009.
- [35] Benz, T. Small-strain stiffness of soils and its numerical consequences. PhD thesis, University of Stuttgart, 2007.
- [36] Bergmair, M., Harer, G., Riedmüller, G., and Stadlmann, T. Die Baugeologie des Galgenbergtunnels. Felsbau, 14(1):15–21, 1996.
- [37] Biscoping, M. and Kampen, R. Zusammensetzung von Normalbeton Mischungsberechnung, February 2017. URL https://mitglieder.vdz-online.de/fileadmin/gruppen/vdz/3LiteraturRecherche/Zementmerkblaetter/ZM_B20_2017_2.pdf. Zement-Merkblatt Betontechnik B 20; last access: December 16th, 2022.
- [38] Bjureland, W., Johansson, F., Sjölander, A., Spross, J., and Larsson, S. Probability distributions of shotcrete parameters for reliability-based analyses of rock tunnel support. *Tunnelling and Underground Space Technology*, 87:15–26, May 2019.
- [39] Bjurström, S. Shear strength of hard rock joints reinforced by grouted untensioned bolts. In Proceedings of the 3rd Congress of the International Society for Rock Mechanics (ISRM), pages 1194–1199, Denver, Colorado, USA, September 1974.
- [40] Blair, T. C. and McPherson, J. G. Grain-size and textural classification of coarse sedimentary particles. *Journal of Sedimentary Research*, 69(1):6–19, January 1999.
- [41] Blümel, M. Personal communication, November 2020.
- [42] Boos, P. and Dietermann, M. Wet Shotcrete Performance—Laboratory Test Methods and influencing Factors in Practice. *Tunnel*, 29(6):31–41, 2010.

BIBLIOGRAPHY 290 of 498

[43] Bossart, P., Meier, P. M., Moeri, A., Trick, T., and Mayor, J.-C. Geological and hydraulic characterisation of the excavation disturbed zone in the Opalinus Clay of the Mont Terri Rock Laboratory. *Engineering Geology*, 66(1–2):19–38, October 2002.

- [44] Boumiz, A., Vernet, C., and Tenoudji, F. C. Mechanical properties of cement pastes and mortars at early ages. *Advanced Cement Based Materials*, 3(3-4):94–106, April 1996.
- [45] Brady, B. H. G. and Brown, E. T. Rock Mechanics for underground mining. Springer Netherlands, 3rd edition, 2004.
- [46] Brandtner, M. Numerical Analysis of Fault Zones—Coming Closer to a Solution. In Schubert, W., Kluckner, A., and Pilgerstorfer, T., editors, *Proceedings of the Workshop "Characterization of Fault Zones" as part of the 62nd Geomechanics Colloquium*, pages 60–63, Salzburg, Austria, October 2013. Austrian Society for Geomechanics.
- [47] Brandtner, M. Personal communication, June 2020.
- [48] Brandtner, M. Personal communication, April 2022.
- [49] Brandtner, M. Personal communication, May 2022.
- [50] Brandtner, M. and Lenz, G. Checking the system behaviour using a numerical model. Geomechanics and Tunnelling, 10(4):353–365, August 2017.
- [51] Bray, J. W. Unpublished note. 1977.
- [52] BRITE-EURAM. BRE-CT92-0231. new Materials, Design and Construction Techniques for Underground Structures in Soft Rock and Clay Media. Technical report, Mott MacDonald Ltd (project coordinator), 1998. Research project funded by EU (programme: FP3-BRITE/EURAM 2).
- [53] Brodie, K., Fettes, D., Harte, B., and Schmid, R. Towards a unified nomenclature of metamorphic petrology: 5. structural terms including fault rock terms. PDF, November 2004. URL https://www.ugr.es/~agcasco/personal/IUGS/pdf-IUGS/scmr_struc2_structuraltermsincludingfaultrockterms.pdf. Recommendations by the IUGS Subcommission on the Systematics of Metamorphic Rocks. Last access: 07.01.2023.
- [54] Brosch, F.-J. and Pischinger, G. Small- to meso-scale brittle rock structures and the estimation of "paleostress" axes—A case study from the Koralm region (Styria/Carinthia). Austrian Journal of Earth Sciences, 107(2):37–59, 2014.
- [55] Brown, E. T. and Gonano, L. P. Improved compression test technique for soft rock. *Journal of the Geotechnical Engineering Division*, 100(2):196–199, 1974.
- [56] Brugg Kabel AG. Datasheet: BRUsens strain V3 (LLK-BSST V3 7.2 mm). Version: 2012/09/12 Rev. 02 TH. Technical report, Brugg, Switzerland, 2012.
- [57] Bryne, L. E. Time Dependent Material Properties of Shotcrete for Hard Rock Tunnelling. PhD thesis, KTH Royal Institute of Technology, Stockholm, Sweden, May 2014.
- [58] Buchmayer, F., Monsberger, C. M., and Lienhart, W. Advantages of tunnel monitoring using distributed fibre optic sensing. *Journal of Applied Geodesy*, 15(1):1–12, December 2020.

BIBLIOGRAPHY 291 of 498

[59] Budil, A. Längsverschiebungen beim Tunnelvortrieb. PhD thesis, Graz University of Technology, Graz, Austria, May 1996.

- [60] Bürgi, C. Cataclastic fault rocks in underground excavations A geological characterisation. Phd thesis, École Polytechnique Fédérale de Lausanne, Lausanne, Switzerland, 1999.
- [61] Burgstaller, M., Goricki, A., and Vanek, R. Semmering Base Tunnel new—Tender documents: Report on the geotechnical ground characterisation. Project document (in german), Austrian Federal Railways, April 2014.
- [62] Button, E. A. A Contribution to the Characterization of Phyllitic and Schistose Rock Masses for Tunnelling. PhD thesis, Graz University of Technology, Graz, Austria, 2004.
- [63] Byfors, J. Plain concrete at early ages. Technical report, Swedish Cement and Concrete Research Institute, Stockholm, Sweden, 1980.
- [64] Candappa, D. C., Sanjayan, J. G., and Setunge, S. Complete Triaxial Stress-Strain Curves of High-Strength Concrete. *Journal of Materials in Civil Engineering*, 13(3):209–215, June 2001.
- [65] Cardozo, N. and Allmendinger, R. W. Spherical projections with OSXStereonet. Computers & Geosciences, 51:193–205, February 2013.
- [66] Çengel, Y. A., Boles, M. A., and Kanoğlu, M. Thermodynamics: an engineering approach. McGraw-Hill Education, New York, USA, 9th edition, 2019.
- [67] CEB. International System of Unified Standard Codes of Practice for Structures—Volume 2: CEB-FIP Model Code for Concrete Structures. In CEB Bulletins d'information, number 124. Comité Euro-International du Béton (CEB), 1978.
- [68] CEB. CEB-FIP Model Code 90: Design Code. Technical report, Comité Euro-International du Béton (CEB), 1993.
- [69] Cervera, M., Oliver, J., and Prato, T. Thermo-Chemo-Mechanical Model for Concrete. I: Hydration and Aging. *Journal of Engineering Mechanics*, 125(9):1018–1027, September 1999.
- [70] Cervera, M., Oliver, J., and Prato, T. Thermo-Chemo-Mechanical Model for Concrete. II: Damage and Creep. Journal of Engineering Mechanics, 125(9):1028–1039, September 1999.
- [71] Chang, Y. Tunnel support with shotcrete in weak rock—a rock mechanics study. PhD thesis, KTH Royal Institute of Technology, Stockholm, Sweden, 1994.
- [72] Chen, A. C. T. and Chen, W.-F. Constitutive Relations for Concrete. *Journal of the Engineering Mechanics Division*, 101(4):465–481, August 1975.
- [73] Chen, G., Kemeny, J. M., and Harpalani, S. Fracture propagation and coalescence in marble plates with pre-cut notches under compression. In Myer, L. R., Cook, N. G. W., Goodman, R. E., and Tsang, S. F., editors, *Proceedings of the International Symposium on Fractured and Jointed Rock Masses*, pages 443–448, Lake Tahoe, California, USA, June 1992. A.A. Balkema.
- [74] Chen, W.-F. Plasticity in Reinforced Concrete. McGraw-Hill, New York, 1982.

BIBLIOGRAPHY 292 of 498

[75] Cheng, C. Influence of discontinuities on post-peak behavior of rock in uniaxial compressive test by numerical study. In Farag, A. A., editor, *Proceedings of the 2nd International Conference on Multimedia Technology (ICMT 2011)*, pages 6406–6409, Hangzhou, China, July 2011. Institute of Electrical and Electronics Engineers.

- [76] Cheng, Z. and Detournay, C. Plastic hardening model I: Implementation in FLAC3D. In Gómez, P., Detournay, C., Hart, R., and Nelson, M., editors, *Proceedings of the 4th Itasca Symposium on Applied Numerical Modeling*, pages 267–276, Lima, Perú, March 2016. Itasca International Inc., Minneapolis.
- [77] Cheng, Z. and Lucarelli, A. Plastic hardening model II: Calibration and validation. In Gómez, P., Detournay, C., Hart, R., and Nelson, M., editors, *Proceedings of the 4th Itasca Symposium on Applied Numerical Modeling*, pages 393–402, Lima, Perú, March 2016. Itasca International Inc., Minneapolis.
- [78] Codegone, G., Festa, A., and Dilek, Y. Formation of Taconic mélanges and broken formations in the Hamburg Klippe, Central Appalachian Orogenic Belt, Eastern Pennsylvania. Tectonophysics, 568-569:215–229, September 2012.
- [79] Coli, N., Berry, P., and Boldini, D. Analysis of the block-size distribution in the Shale-Limestone Chaotic Complex (Tuscany, Italy). In Wilson, S., Ewy, R., and Tutuncu, A., editors, Proceedings of the 42nd US Rock Mechanics Symposium and 2nd U.S.-Canada Rock Mechanics Symposium, pages 1–7, San Francisco, California, 29 June–2 July, 2008. American Rock Mechanics Association (ARMA): Alexandria. ARMA 08-233.
- [80] Coli, N., Boldini, D., and Bandini, A. Modeling of complex geological rock mixtures under triaxial testing conditions. In *Proceedings of the 2012 Regional Symposium of the International Society for Rock Mechanics (EUROCK 2012)—Rock Engineering and Technology for Sustainable Underground Construction*, pages 1–12, Stockholm, Sweden, May 2012.
- [81] Cook, N. G. W. The application of seismic techniques to problems in rock mechanics. International Journal of Rock Mechanics and Mining Sciences & Geomechanics Abstracts, 1(2):169–179, March 1964.
- [82] Cook, N. G. W. An experiment proving that dilatancy is a pervasive volumetric property of brittle rock loaded to failure. *Rock Mechanics*, 2(4):181–188, December 1970.
- [83] Cook, N. G. W., Hoek, E., Pretorius, J. P. G., Ortlepp, W. D., and Salamon, M. D. G. Rock mechanics applied to the study of rockbursts. *Journal of the South African Institute* of Mining and Metallurgy, 66:436–528, 1966.
- [84] Cordes, T., Weifner, T., Unteregger, D., and Bergmeister, K. Interaction between deep tunnel drives and an existing tunnel in fault zones-Modelling against reality. *Geomechanics* and Tunnelling, 12(6):641-650, December 2019.
- [85] Cornejo-Malm, G. Schwinden von Spritzbeton. Research report, ETH Zurich, 1995.
- [86] Coussy, O. Mechanics of Porous Continua. Wiley: Chichester, United Kingdom, 1995.
- [87] Coussy, O. Mechanics and physics of porous solids. John Wiley & Sons, Ltd: Chichester, United Kingdom, 1st edition, 2010.

BIBLIOGRAPHY 293 of 498

[88] Cowan, D. S. Structural styles in Mesozoic and Cenozoic mélanges in the western Cordillera of North America. *GSA Bulletin*, 96(4):451–462, April 1985.

- [89] Cudny, M. and Truty, A. Refinement of the Hardening Soil model within the small strain range. *Acta Geotechnica*, 15(8):2031–2051, March 2020.
- [90] Daller, J., Atzl, G., and Blümel, M. Festschrift zum 60. Geburtstag von Wulf Schubert, chapter Bestimmung von Gesteinskennwerten an Störungsmaterial, pages 50–58. Institute of Rock Mechanics and Tunnelling, Graz University of Technology, Graz, Austria, 2010.
- [91] Dassault Systèmes Simulia Corp. Abaqus/CAE 2017 documentation.
- [92] Davila Mendez, J. M. Displacements Analysis in Layered Rock Masses. PhD thesis, Graz University of Technology, Graz, Austria, January 2016.
- [93] Deere, D. U. Rock Mechanics in Engineering Practice, chapter Geological considerations, pages 1–20. Wiley, New York, 1968. Chapter 1.
- [94] Deere, D. U. and Miller, R. P. Engineering classification and index properties for intact rock. Technical report AFWL-TR-65-116, Air Force Weapons Laboratory, Kirtland Air Force Base, New Mexico, USA, December 1966.
- [95] Deutsche Gesellschaft für Geotechnik e.V. (DGGT). Empfehlungen des Arbeitskreises "Numerik in der Geotechnik"–EANG. Wilhelm Ernst & Sohn, Verlag für Architektur und technische Wissenschaften GmbH & Co. KG, Berlin, Germany, February 2014.
- [96] Dickmann, T. Personal communication, July 2021.
- [97] Diederichs, M. S., Carvalho, J. L., and Carter, T. G. A Modified Approach For Prediction of Strength And Post Yield Behaviour For High GSI Rockmasses In Strong, Brittle Ground. In Eberhardt, E., Stead, D., and Morrison, T., editors, Proceedings of the 1st Canada-US Rock Mechanics Symposium: Rock Mechanics: Meeting Society's Challenges and Demands, pages 249–257, Vancouver, Canada, April 2007. ARMA-07-031.
- [98] Ding, Y. Technologische Eigenschaften von jungem Stahlfaserbeton und Stahlfaserspritzbeton. PhD thesis, University of Innsbruck, Innsbruck, Austria, 1998.
- [99] Dorfmann, E. M. Zugkriechen von Beton in Abhängigkeit der Spannungsgeschichte. Master's thesis, Graz University of Technology, Graz, Austria, June 2017.
- [100] Eberhardt, E. Numerical modelling of three-dimension stress rotation ahead of an advancing tunnel face. *International Journal of Rock Mechanics and Mining Sciences*, 38(4):499–518, June 2001.
- [101] Eberly, D. Approximating an Ellipse by Circular Arcs, April 2016. URL https://www.geometrictools.com/Documentation/ApproximateEllipse.pdf. Last access: 26.09.2020.
- [102] Egger, P. Einfluss des Post-Failure Verhaltens von Fels auf den Tunnelausbau unter besonderer Berücksichtigung des Ankerausbaus. PhD thesis, Universität Karlsruhe, Karlsruhe, Germany, 1973.
- [103] Ekici, Z. Semmering Base Tunnel, construction lot SBT 1.1, tunnel Gloggnitz—Tender documents: Calculation values. Project document (in german), Austrian Federal Railways, 2014.

BIBLIOGRAPHY 294 of 498

[104] Engels, S., Wieselthaler, F., Pischinger, G., and Holzer, R. Semmering Base Tunnel, construction lot SBT 1.1, tunnel Gloggnitz, track 1—Engineering geological documentation. Project document (in german), Austrian Federal Railways, 2016.

- [105] Engels, S., Wieselthaler, F., and Holzer, R. Semmering Base Tunnel, construction lot SBT 1.1, tunnel Gloggnitz, track 1—Geotechnical horizontal and longitudinal section. Project document (in german), Austrian Federal Railways, 2017.
- [106] Engl, D. A., Fellin, W., and Zangerl, C. Scherfestigkeiten von Scherzonengesteinen—Ein Beitrag zur geotechnischen Bewertung von tektonischen Störungszonen und Gleitzonen von Massenbewegungen. Bulletin für Angewandte Geologie, 13(2):63–81, 2008.
- [107] England, G. L. and Illston, J. M. Methods of computing stress in concrete from a history of measured strain. *Civil Engineering and Public Works Review*, 60(1–3):513–517, 692–694, 846–847, April, May, June 1965.
- [108] Entfellner, M. Prediction of Displacements and Shotcrete Lining Utilization—Decision strategy for a timely application of ductile support systems in conventional tunnelling. Master's thesis, Graz University of Technology, Graz, Austria, August 2017.
- [109] Entfellner, M., Schubert, W., and Moritz, B. A. Early warning of overbreaks in tunnels. In Proceedings of the 2022 Regional Symposium of the International Society for Rock Mechanics (EUROCK 2022)–Rock and Fracture Mechanics in Rock Engineering and Mining, pages 1–8, Espoo, Finland, September 2022.
- [110] European Committee for Standardization. EN 1992-1-1:2004. Eurocode 2: Design of concrete structures Part 1-1: General rules and rules for buildings. Standard, December 2004.
- [111] Fairhurst, C. E. and Hudson, J. Draft ISRM suggested method for the complete stress-strain curve for intact rock in uniaxial compression. *International Journal of Rock Mechanics and Mining Sciences & Geomechanics Abstracts*, 36:279–289, 1999.
- [112] Farmer, I. W. Stress distribution along a resin grouted rock anchor. *International Journal of Rock Mechanics and Mining Sciences & Geomechanics Abstracts*, 12(11):347–351, November 1975.
- [113] Farmer, I. W. Engineering Behaviour of Rocks. Springer Netherlands, 1st edition, 1983.
- [114] Fasching, F. and Vanek, R. Engineering geological characterisation of fault rocks and fault zones. *Geomechanics and Tunnelling*, 4(3):181–194, June 2011.
- [115] Faulkner, D. R., Lewis, A. C., and Rutter, E. H. On the internal structure and mechanics of large strike-slip fault zones: field observations of the Carboneras fault in southeastern Spain. *Tectonophysics*, 367(3-4):235–251, June 2003.
- [116] Faulkner, D. R., Jackson, C. A. L., Lunn, R. J., Schlische, R. W., Shipton, Z. K., Wibberley, C. A. J., and Withjack, M. O. A review of recent developments concerning the structure, mechanics and fluid flow properties of fault zones. *Journal of Structural Geology*, 32(11): 1557–1575, November 2010.
- [117] Feder, G. and Arwanitakis, M. Zur Gebirgsmechanik ausbruchsnaher Bereiche tiefliegender Hohlraumbauten (unter zentralsymmetrischer Belastung). Berg- und Hüttenmännische Monatshefte, 121(4):103–117, 1976.

BIBLIOGRAPHY 295 of 498

[118] Feenstra, P. H. and de Borst, R. Aspects of Robust Computational Models for Plain and Reinforced Concrete. *HERON*, 38(4):1–76, 1993.

- [119] Feynman, R. P., Leighton, R. B., and Sands, M. The Feynman Lectures on Physics, volume I: Mainly Mechanics, Radiation, and Heat. Basic Books, 2010.
- [120] fib. Structural Concrete: Textbook on Behaviour, Design and Performance: Updated knowledge of the CEB/FIP Model Code 1990. Technical report, fédération internationale du béton (fib), Lausanne, Switzerland, July 2000.
- [121] fib. CEB-FIP Model Code for Concrete Structures 2010. Technical report, fédération internationale du béton (fib), 2013.
- [122] Fischnaller, G. Untersuchungen zum Verformungsverhalten von jungem Spritzbeton im Tunnelbau—Grundlagen und Versuche. Master's thesis, University of Innsbruck, Innsbruck, Austria, 1992.
- [123] Fjellström, P. Measurement and Modelling of Young Concrete Properties. Licentiate thesis, Luleå University of Technology, Luleå, Sweden, 2013.
- [124] Forth, J. P. Predicting the tensile creep of concrete. Cement and Concrete Composites, 55: 70–80, January 2015.
- [125] Fossen, H. Structural Geology. Cambridge University Press, 2nd edition, 2016.
- [126] GEOKON. Instruction Manual: Model 4200 Series, Vibrating Wire Strain Gauges. Version: 11/08/2019 (revision DD). Technical report, Lebanon, New Hampshire, USA, 2019.
- [127] Glawe, U. and Upreti, B. N. Better Understanding the Strengths of Serpentinite Bimrock and Homogeneous Serpentinite. *Felsbau*, 22(5):53–60, 2004.
- [128] Golser, J., Schubert, P., and Rabensteiner, K. A new concept for evaluation of loading in shotcrete linings. In *Proceedings of the International Congress on Progress and Innovation* in *Tunnelling*, volume I, pages 79–85, Toronto, Canada, September 1989.
- [129] Golser, J., Rabensteiner, K., Sigl, O., Aldrian, W., Wedenig, H., Brandl, J., and Maier, C. Materialgesetz für Spritzbeton. Technical report, Bundesministerium für wirtschaftliche Angelegenheiten: Straßenforschung, 1990.
- [130] Goodman, R. E. Introduction to Rock Mechanics. John Wiley & Sons, 2nd edition, 1989.
- [131] Goodman, R. E. Engineering geology: rock in engineering construction. John Wiley & Sons, Inc., 1993.
- [132] Goricki, A. and Pimentel, E. Triaxial Tests on Cataclasites. Rock Mechanics and Rock Engineering, 48(5):2167–2171, November 2014.
- [133] Granet, I., Alvarado, J. L., and Bluestein, M. Thermodynamics and Heat Power. CRC Press, Boca Raton, USA, 9th edition, 2021.
- [134] Grassl, P. and Jirásek, M. Damage-plastic model for concrete failure. *International Journal of Solids and Structures*, 43(22-23):7166–7196, November 2006.
- [135] Graziani, A., Boldini, D., and Ribacchi, R. Practical Estimate of Deformations and Stress Relief Factors for Deep Tunnels Supported by Shotcrete. *Rock Mechanics and Rock Engineering*, 38(5):345–372, June 2005.

BIBLIOGRAPHY 296 of 498

[136] Green, S. J. and Swanson, S. R. Static constitutive relations for concrete. Technical report AFWL-TR-72-244, Air Force Weapons Laboratory, Kirtland Air Force Base, New Mexico, USA, April 1973.

- [137] Groshong, R. H. j. Low-temperature deformation mechanisms and their interpretation. Geological Society of America Bulletin, 100(9):1329–1360, September 1988.
- [138] Gross, D., Hauger, W., and Wriggers, P. Technische Mechanik 4: Hydromechanik, Elemente der Höheren Mechanik, Numerische Methoden. Springer Berlin Heidelberg, 7th edition, 2009.
- [139] Großauer, K. Tunnelling in Heterogeneous Ground—Numerical Investigation of Stresses and Displacements. Diploma thesis, Graz University of Technology, Graz, Austria, October 2001.
- [140] Großauer, K. Expert System Development for the Evaluation and Interpretation of Displacement Monitoring Data in Tunnelling. PhD thesis, Graz University of Technology, Graz, Austria, February 2009.
- [141] Grübl, P., Weigler, H., and Karl, S. Beton—Arten, Herstellung und Eigenschaften. Ernst & Sohn Verlag, Berlin, 2nd edition, 2001.
- [142] Gruppe TUNNEL:Monitor. TUNNEL:monitor (v2021.1.4). URL https://igt-engineering.com/de/forschung-und-entwicklung/tunnelmonitor/. Last access: 15.11.2022.
- [143] Gschwandtner, G. G. Analytische Berechnungsansätze zum Kennlinienverfahren. Master's thesis, Montanuniversität Leoben, Leoben, Austria, January 2010.
- [144] Gudmundsson, A., Simmenes, T. H., Larsen, B., and Philipp, S. L. Effects of internal structure and local stresses on fracture propagation, deflection, and arrest in fault zones. *Journal of Structural Geology*, 32(11):1643–1655, November 2010.
- [145] Guntli, P., Keller, F., Lucchini, R., and Rust, S. Gotthard-Basistunnel: Geologie, Geotechnik, Hydrologie zusammenfassender Schlussbericht. Technical report 7, Landesgeologie, 2016.
- [146] Guo, P. and Su, X. Shear strength, interparticle locking, and dilatancy of granular materials. Canadian Geotechnical Journal, 44(5):579–591, May 2007.
- [147] Harer, G., Prein, R., Schwab, P., and Wehr, H. Tunnelling in Poor Ground Conditions Case History Galgenbergtunnel. *Felsbau*, 14(2):82–86, 1996.
- [148] Hartog, A. H. An Introduction to Distributed Optical Fibre Sensors. CRC Press, May 2017.
- [149] Hauggaard-Nielsen, A. B. Mathematical Modelling and Experimental Analysis of Early Age Concrete. PhD thesis, Technical University of Denmark, Lyngby, Denmark, October 1997.
- [150] Havlásek, P., Šmilauer, V., Hájková, K., and Baquerizo, L. Thermo-mechanical simulations of early-age concrete cracking with durability predictions. In *IOP Conference Series:*Materials Science and Engineering, volume 236, pages 1–7. IOP Publishing, September 2017.
- [151] Heinisch, M., Mayr, B., Millen, B., and Holzer, R. Semmering Base Tunnel, construction lot SBT 1.1, access tunnel Göstritz—Geotechnical horizontal and longitudinal section. Project document (in german), 2016.

BIBLIOGRAPHY 297 of 498

[152] Heinisch, M., Mayr, B., Millen, B., and Holzer, R. Semmering Base Tunnel, construction lot SBT 1.1, access tunnel Göstritz—Engineering geological documentation. Project document (in german), Austrian Federal Railways, 2016.

- [153] Heinrich, P. J. Effiziente Erfassung viskoelastischer Eigenschaften bei der Spannungsermittlung von gezwängten Betonbauteilen. PhD thesis, Graz University of Technology, Graz, Austria, November 2018.
- [154] Hellmich, C. Shotcrete as part of the New Austrian Tunneling Method: From Thermochemomechanical Material Modeling to Structural Analysis and Safety Assessment of Tunnels. PhD thesis, Vienna University of Technology, Vienna, Austria, 1999.
- [155] Hellmich, C., Ulm, F.-J., and Mang, H. A. Multisurface Chemoplasticity. I: Material Model for Shotcrete. *Journal of Engineering Mechanics*, 125(6):692–701, 1999.
- [156] Hellmich, C., Ulm, F.-J., and Mang, H. A. Multisurface Chemoplasticity. II: Numerical Studies on NATM Tunneling. *Journal of Engineering Mechanics*, 125(6):702–713, 1999.
- [157] Hellmich, C., Sercombe, J., Ulm, F.-J., and Mang, H. A. Modeling of Early-Age Creep of Shotcrete. II: Application to Tunneling. *Journal of Engineering Mechanics*, 126(3):292–299, 2000.
- [158] Hellmich, C., Mang, H. A., and Ulm, F.-J. Hybrid method for quantification of stress states in shotcrete tunnel shells: combination of 3D in situ displacement measurements and thermochemoplastic material law. *Computers & Structures*, 79(22):2103–2115, 2001.
- [159] Henzinger, M. R., Schachinger, T., Lienhart, W., Buchmayer, F., Weilinger, W., Stefaner, R., Haberler-Weber, M., Haller, E.-M., Steiner, M., and Schubert, W. Fibre-optic supported measurement methods for monitoring rock pressure. *Geomechanics and Tunnelling*, 11(3): 251–263, June 2018.
- [160] Hettler, A. and Vardoulakis, I. Behaviour of dry sand tested in a large triaxial apparatus. Géotechnique, 34(2):183–197, June 1984.
- [161] Hill, R. The mathematical theory of plasticity. The Clarendon Press, Oxford, 1951.
- [162] Hodgson, K. and Cook, N. G. W. The effects of size and stress gradient on the strength of rock. In Proceedings of the 2nd Congress of the International Society for Rock Mechanics, volume 2, pages 31–34, Belgrade, Serbia, September 1970.
- [163] Hoek, E. and Brown, E. T. Practical estimates of rock mass strength. *International Journal of Rock Mechanics and Mining Sciences*, 34(8):1165–1186, December 1997.
- [164] Hoek, E. and Diederichs, M. S. Empirical estimation of rock mass modulus. *International Journal of Rock Mechanics and Mining Sciences*, 43(2):203–215, February 2006.
- [165] Hoek, E. Brittle failure of rock. Rock Mechanics in Engineering Practice. Wiley: New York, 1968.
- [166] Hoek, E. and Brown, E. T. *Underground Excavations in Rock*. CRC Press, 1st edition, 1980.
- [167] Hoek, E. and Brown, E. T. Empirical Strength Criterion for Rock Masses. *Journal of the Geotechnical Engineering Division*, 106(9):1013–1035, September 1980.

BIBLIOGRAPHY 298 of 498

[168] Holt, E. E. Early age autogeneous shrinkage of concrete. Vtt publications 446, Technical Research Centre of Finland, Espoo, Finland, 2001.

- [169] Holter, K. G. Properties of waterproof sprayed concrete tunnel linings: A study of EVAbased sprayed membranes for waterproofing of rail and road tunnels in hard rock and cold climate. PhD thesis, Norwegian University of Science and Technology, Trondheim, Norway, December 2015.
- [170] Holzer, R. Personal communication, September 2022.
- [171] Holzer, R., Prall, K., Wagner, O. K., and Gobiet, G. Semmering Base Tunnel Tunnelling in challenging geotechnical and geological conditions in major fault zones. *Geomechanics and Tunnelling*, 13(5):509–518, October 2020.
- [172] Hösthagen, A. Thermal Crack Risk Estimation and Material Properties of Young Concrete. Licentiate thesis, Luleå University of Technology, Luleå, Sweden, 2017.
- [173] Huber, H. Untersuchungen zum Verformungsverhalten von jungem Spritzbeton im Tunnelbau. Master's thesis, University of Innsbruck, Innsbruck, Austria, 1991.
- [174] Ikumi, T., Salvador, R. P., and Aguado, A. Mix proportioning of sprayed concrete: A systematic literature review. *Tunnelling and Underground Space Technology*, 124(104456): 12, June 2022.
- [175] Itasca Consultants S.A.S. Dynamic Analysis in FLAC3D. Electronical, 2020. URL https://www.itasca.fr/software/dynamic-analysis-in-flac3d. Last access: 23.12.2020.
- [176] Itasca Consulting Group, Inc. UDEC 5.0 documentation, 2011.
- [177] Itasca Consulting Group, Inc. FLAC3D 6.0 documentation, 2017.
- [178] Itasca Consulting Group, Inc. FLAC3D 7.0 documentation, 2019.
- [179] Itasca Consulting Group, Inc. Learning Itasca Educational Partnership. Electronical, 2023. URL https://www.itascainternational.com/learning/iep/iep-research-program. Last access: 05.01.2023.
- [180] Jaeger, J. C. and Cook, N. G. W. Fundamentals of Rock Mechanics. Chapman & Hall: London, 3rd edition, 1979.
- [181] Jaeger, J. C., Cook, N. G. W., and Zimmerman, R. W. Fundamentals of Rock Mechanics. Blackwell Publishing, 4th edition, 2007.
- [182] Johnson, R. B. and DeGraff, J. V. Principles of Engineering Geology. John Wiley & Sons, Inc., 1988.
- [183] Johnston, I. W. Strength of Intact Geomechanical Materials. *Journal of Geotechnical Engineering*, 111(6):730–749, June 1985.
- [184] Kahraman, S. and Alber, M. Estimating unconfined compressive strength and elastic modulus of a fault breccia mixture of weak blocks and strong matrix. *International Journal of Rock Mechanics and Mining Sciences*, 43(8):1277–1287, December 2006.

BIBLIOGRAPHY 299 of 498

[185] Kahraman, S., Alber, M., Fener, M., and Gunaydin, O. Evaluating the geomechanical properties of Misis fault breccia (Turkey). *International Journal of Rock Mechanics and Mining Sciences*, 45(8):1469–1479, December 2008.

- [186] Kahraman, S., Gunaydin, O., Alber, M., and Fener, M. Evaluating the strength and deformability properties of Misis fault breccia using artificial neural networks. *Expert Systems with Applications*, 36(3):6874–6878, April 2009.
- [187] Kainrath-Reumayer, S., Gschwandtner, G., Schuller, E., and Galler, R. Beitrag zur Anwendung des Kennlinienverfahrens. *Berg- und Hüttenmännische Monatshefte*, 155(2): 83–89, February 2010.
- [188] Kainrath-Reumayer, S., Neugebauer, E., Charette, F., Plouffe, M., and Galler, R. Ankerung im Untertagebau - Entwicklungen in Theorie und Praxis. Geomechanik und Tunnelbau, 1 (5):345–351, October 2008.
- [189] Kaiser, P. K. and Kim, B. H. Rock mechanics challenges of underground constructions and mining. In *Proceedings of the Korean Rock Mechanics Symposium*, pages 1–16, Seoul, South Korea, 2008. Korean Society for Rock Mechanics.
- [190] Kaiser, P. K. and Tannant, D. D. The Role of Shotcrete in Hard Rock Mines. In Hustrulid, W. A. and Bullock, R. L., editors, *Underground Mining Methods—Engineering Fundamentals* and International Case Studies, chapter 67, pages 579–592. Society for Mining, Metallurgy, and Exploration, Inc. (SME), 2001.
- [191] Kaiser, P. K., Diederichs, M. S., Martin, C. D., Sharp, J., and Steiner, W. Underground Works In Hard Rock Tunnelling And Mining. In *Proceedings of the International Conference on Geotechnical & Geological Engineering (GeoEng2000)*, ISRM International Symposium, pages 841–926, Melbourne, Australia, November 2000. Technomic Publishing Co.
- [192] Kaiser, P. K., Amann, F., and Steiner, W. How Highly Stressed Brittle Rock Failure Impacts Tunnel Design. In Proceedings of the 2010 Regional Symposium of the International Society for Rock Mechanics (EUROCK 2010), pages 1–12, Lausanne, Switzerland, June 2010. ISRM-EUROCK-2010-003.
- [193] Kalender, A., Sönmez, H., Medley, E. W., Tunusluoglu, C., and Kasapoglu, K. E. An approach to predicting the overall strengths of unwelded bimrocks and bimsoils. *Engineering Geology*, 183:65–79, December 2014.
- [194] Kastner, H. Statik des Tunnel- und Stollenbaues: auf der Grundlage geomechanischer Erkenntnisse. Springer Berlin Heidelberg, 1962.
- [195] Kettunen Linder, M. and Kilic, O. En studie av sprutbetongförstärkningen i Citybanan -Norrströmstunneln. Master's thesis, KTH Royal Insitute of Technology, Stockholm, Sweden, March 2011. Examensarbete 326.
- [196] Kim, Y.-S., Peacock, D. C. P., and Sanderson, D. J. Fault damage zones. *Journal of Structural Geology*, 26(3):503–517, March 2004.
- [197] Kirsch, G. Die Theorie der Elastizität und die Bedürfnisse der Festigkeitslehre. Zeitschrift des Vereines Deutscher Ingenieure, 42(29):797–807, 1898.

BIBLIOGRAPHY 300 of 498

[198] Klein, C. and Philpotts, A. R. Earth materials: introduction to mineralogy and petrology. Cambridge University Press, 1st edition, 2013.

- [199] Kluckner, A. Aspekte der Gebirgscharakterisierung im Tunnelbau. Master's thesis, Graz University of Technology, Graz, Austria, October 2012.
- [200] Kluckner, A. and Schubert, W. Study on the Anisotropic Displacement Pattern at a Conventional Tunnel Drive. In *Proceedings of the 5th ISRM Young Scholars' Symposium on Rock Mechanics and International Symposiumon Rock Engineering for Innovative Future (YSRM2019 & REIF2019)*, pages 1–6, Okinawa, Japan, December 2019.
- [201] Knipe, R. J. Deformation mechanism path diagrams for sediments undergoing lithification. Structural Fabric in Deep Sea Drilling Project Cores From Forearcs, Memoir 166:151–160, 1986.
- [202] Kovler, K. Why sealed concrete swells. ACI Materials Journal, 93(4):334-340, 1996.
- [203] Kropik, C. and Mang, H. A. Computational mechanics of the excavation of tunnels. Engineering Computations, 13(7):49–69, November 1996.
- [204] Kulhawy, F. H. Stress deformation properties of rock and rock discontinuities. *Engineering Geology*, 9(4):327–350, December 1975.
- [205] Kusterle, W. Qualitätsverbesserungen beim Spritzbeton durch technologische Massnahmen, durch den Einsatz neuer Materialien und auf Grund der Erfassung von Spritzbetoneigenschaften. Habilitation dissertation, University of Innsbruck, Innsbruck, Austria, 1992.
- [206] Kusterle, W. Comparison of shrinkage behaviour and creep properties under different compressive stress levels for wet-mix sprayed concrete from ten hours up to two weeks. Technical report, Morgan Tunnelling, 1999.
- [207] Kusterle, W. and Lukas, W. Spritzbeton hoher Güte für die einschalige Spritzbetonbauweise. In Tagungsband der 3. Internationalen Fachtagung Spritzbeton-Technologie, Innsbruck, Austria, pages 29–40, 1990.
- [208] Kusterle, W., Jäger, J., John, M., Neumann, C., and Röck, R. Spritzbeton im Tunnelbau. In Bergmeister, K., Fingerloos, F., and Wörner, J.-D., editors, Beton-Kalender 2014: Unterirdisches Bauen, Grundbau, Eurocode 7, chapter IX, pages 303–390. Ernst & Sohn GmbH & Co. KG., 2014.
- [209] Kuwajima, F. M. Early Age Properties of Shotcrete. In Celestino, T. B. and Parker, H. W., editors, Proceedings of the Eighth International Conference on Shotcrete for Underground Support, São Paulo, Brazil, April 1999. American Society of Civil Engineers.
- [210] Lackner, R. and Mang, H. A. Cracking in shotcrete tunnel shells. *Engineering Fracture Mechanics*, 70(7–8):1047–1068, May 2003.
- [211] Lackner, R., Hellmich, C., and Mang, H. A. Constitutive modeling of cementitious materials in the framework of chemoplasticity. *International Journal for Numerical Methods in Engineering*, 53(10):2357–2388, 2002.
- [212] Lackner, R., Macht, J., Hellmich, C., and Mang, H. A. Hybrid Method for Analysis of Segmented Shotcrete Tunnel Linings. *Journal of Geotechnical and Geoenvironmental Engineering*, 128(4):298–308, April 2002.

BIBLIOGRAPHY 301 of 498

[213] Lama, R. D. and Vutukuri, V. S. *Handbook on Mechanical Properties of Rocks*, volume 2 of *Series on Rock and Soil Mechanics*. Trans Tech Publications, Clausthal, Germany, 1978.

- [214] Laplante, P. Propriétés mécaniques des bétons durcissants: analyse comparée des bétons classiques et à très hautes performances [Mechanical properties of hardening concrete: a comparative analysis of classical and high strength concretes]. PhD thesis, Ecole Nationale des Ponts et Chaussées, Paris, France, 1993.
- [215] Laplante, P. and Boulay, C. Evolution du coefficient de dilatation thermique du béton en fonction de sa maturité aux tout premiers âges. *Materials and Structures*, 27(10):596–605, December 1994.
- [216] Leber, C. Einfluss der Primärspannungsorientierung auf die Verschiebungscharakteristik. Master's thesis, Graz University of Technology, Graz, Austria, March 2009.
- [217] Lebschy, D. Investigation of the influence of the tunnel lining on the displacement development. Master's thesis, Graz University of Technology, Graz, Austria, September 2014.
- [218] Lenz, G. Displacement monitoring data in tunnelling—Development of a semiautomatic evaluation system. Diploma thesis, Graz University of Technology, Graz, Austria, April 2007.
- [219] Lenz, G. Characterization of ground and system behaviour in water-bearing fault zones. PhD thesis, Graz University of Technology, Graz, Austria, July 2020.
- [220] Lenz, G. Personal communication, May 2022.
- [221] Lenz, G. Personal communication, July 2022.
- [222] Lenz, G. Personal communication, November 2022.
- [223] Lepique, M. Empfehlung Nr. 10 des Arbeitskreises 3.3 "Versuchstechnik Fels" der Deutschen Gesellschaft für Geotechnik e. V.: Indirekter Zugversuch an Gesteinsproben Spaltzugversuch. *Bautechnik*, 85(9):623–627, September 2008.
- [224] Lienhart, W., Schubert, W., Henzinger, M. R., Buchmayer, F., Weilinger, W., and Stefaner, R. Faseroptisch unterstützte Messmethoden zur Beobachtung von Gebirgsdruck. Research report, Federal Ministry Republic of Austria, Climate Action, Environment, Energy, Mobility, Innovation and Technology, Vienna, Austria, October 2018.
- [225] Lindlar, B., Jahn, M., and Schlumpf, J. Sika Sprayed Concrete Handbook. Sika AG, 2020. URL https://www.sika.com/content/dam/dms/corporate/n/glo-sprayed-concrete-handbook-2021.pdf. Last access: 14.01.2023.
- [226] Lindquist, E. S. and Goodman, R. E. Strength and deformation properties of a physical model melange. In Nelson, P. P. and Laubach, S. E., editors, Rock Mechanics - Models and Measurements - Challenges from Industry: Proceedings of the 1st North American Rock Mechanics Symposium (NARMS), pages 843–850. The University of Texas at Austin, A.A. Balkema: Rotterdam, June 1994.
- [227] Lindquist, E. S. The Strength and Deformation Properties of Melange. PhD thesis, University of California, Berkeley, California, USA, 1994.

BIBLIOGRAPHY 302 of 498

[228] Lockner, D. A. Rock Physics and Phase Relations: A Handbook of Physical Constants, volume 3 of AGU Reference Shelf, chapter Rock Failure, pages 127–147. American Geophysical Union, Washington, D.C., USA, 1st edition, January 1995.

- [229] Logan, J. M., Friedmann, M., Higgs, N., Dengo, C., and Shimamoto, T. Experimental studies of simulated gouge and their application to studies of natural fault zones. In Proceedings of Conference VIII—Analysis of Actual Fault Zones in Bedrock, pages 305—343, Menlo Park, California, USA, April 1979. United States Department of the Interior, Geological Survey, Office of Earthquake Studies. Open-file report 79-1239.
- [230] Lu, T. Autogenous shrinkage of early age cement paste and mortar. PhD thesis, Delft University of Technology, Delft, Netherlands, 2019.
- [231] Lucarelli, A. Personal communication, June 2022.
- [232] Luna Innovations Inc. Datasheet: Luna Optical Backscatter Reflectometer (OBR) Model 4600. Version: LTOBR4600 REV. 004 02/13/2014. Technical report, Blacksburg, Virginia, USA, 2014.
- [233] Luna Innovations Inc. Datasheet: Luna Optical Backscatter Reflectometer (OBR) Model 4600. Version: LTOBR4600 REV. 006 03/09/2018. Technical report, Blacksburg, Virginia, USA, 2018.
- [234] Lupini, J. F., Skinner, A. E., and Vaughan, P. R. The drained residual strength of cohesive soils. *Géotechnique*, 31(2):181–213, June 1981.
- [235] Ma, J. Faserfreier Ultrahochfester Beton—Entwicklung und Materialeigenschaften. PhD thesis, Leipzig University, Leipzig, Germany, 2010.
- [236] Macht, J. Hybrid Analysis of Shotcrete Tunnel Linings: Assessment and Online Monitoring of the Level of Loading. PhD thesis, Vienna University of Technology, Vienna, Austria, 2002.
- [237] Mair, K., Frye, K. M., and Marone, C. Influence of grain characteristics on the friction of granular shear zones. *Journal of Geophysical Research: Solid Earth*, 107(B10):ECV 4–1–ECV 4–9, October 2002.
- [238] Małkowski, P., Ostrowski, L., and Brodny, J. Analysis of Young's modulus for Carboniferous sedimentary rocks and its relationship with uniaxial compressive strength using different methods of modulus determination. *Journal of Sustainable Mining*, 17(3):145–157, 2018.
- [239] Mandl, G. Discontinuous fault zones. *Journal of Structural Geology*, 9(1):105–110, January 1987.
- [240] Mandl, G. Mechanics of Tectonic Faulting: Models and Basic Concepts. Developments in Structural Geology, 1. Elsevier Science Publishers B.V.: Amsterdam, 1988.
- [241] Mandl, G. Faulting in Brittle Rocks: An Introduction to the Mechanics of Tectonic Faults. Springer Berlin Heidelberg, 1st edition, 2000.
- [242] Mang, H. A. and Hofstetter, G. Festigkeitslehre. Springer Berlin Heidelberg, 5th edition, 2018.

BIBLIOGRAPHY 303 of 498

[243] Manton, N. and Mee, N. *The Physical World*. Oxford University Press, 1st edition, April 2017.

- [244] Marcher, T. Personal communication, January 2021.
- [245] Marinos, P. V. and Tsiambaos, G. Strength and Deformability of Specific Sedimentary and Ophiolithic Rocks. *Bulletin of the Geological Society of Greece*, 43(3):1259–1266, January 2010.
- [246] Marshak, S. Earth: portrait of a planet. New York: W.W. Norton & Company, 6th edition, 2019.
- [247] Martin, J. Back-analysis of rock mass parameters at the Semmering Base Tunnel based on the convergence confinement method. Master's thesis, Graz University of Technology, Graz, Austria, December 2022.
- [248] Medley, E. W. Using stereological methods to estimate the volumetric proportions of blocks in melanges and similar block-in-matrix rocks (bimrocks). In Oliveira, R., Rodrigues, L. F., Coelho, A. G., and Cunha, A. P., editors, *Proceedings of the 7th International Congress of the International Association of Engineering Geology (IAEG)*, pages 1031–1040. A.A. Balkema: Rotterdam, September 1994.
- [249] Medley, E. W. Systematic Characterization of Melange Bimrocks and Other Chaotic Soil/Rock Mixtures. Felsbau, 17(3):152–162, 1999.
- [250] Medley, E. W. Orderly Characterization of Chaotic Franciscan Melanges. *Felsbau*, 19(4): 20–33, 2001.
- [251] Medley, E. W. Observations on Tortuous Failure Surfaces in Bimrocks. *Felsbau*, 22(5): 35–43, 2004.
- [252] Medley, E. Tunneling Through Fault Zones and Melanges. Lecture slides of lecture 4 of the short course "Anticipating and addressing the characterization, design and construction problems of fault rocks, melanges and other bimrocks", Geological Engineering Department, Hacettepe University, Ankara, Turkey, June 2004.
- [253] Medley, E. W. Estimating Block Size Distributions of Melanges and Similar Block-in-Matrix Rocks (Bimrocks). In Hammah, R., Bawden, W., Curran, J., and Telesnicki, M., editors, Proceedings of 5th North American Rock Mechanics Symposium (NARMS), pages 599–606, Toronto, Canada, July 2002. University of Toronto Press.
- [254] Medley, E. W. and Zekkos, D. Geopractitioner approaches to working with antisocial mélanges. In Mélanges: Processes of Formation and Societal Significance, number 480, pages 261–277. The Geological Society of America, 2011.
- [255] Medley, E. W. The Engineering Characterization of Melanges and Similar Block-in-Matrix Rocks (Bimrocks). PhD thesis, University of California, Berkeley, California, USA, 1994.
- [256] Medley, E. W. and Lindquist, E. S. The engineering significance of the scale-independence of some Franciscan melanges in California, USA. In Daemen, J. J. K. and Schultz, R. A., editors, *Proceedings of the 35th U.S. Symposium on Rock Mechanics*, pages 907–914. A.A. Balkema, Rotterdam, 1995.

BIBLIOGRAPHY 304 of 498

[257] Meixner, T. Trigger Values for tunnel monitoring in SCL shallow tunnels. Master's thesis, Graz University of Technology, Graz, Austria, September 2016.

- [258] Menétrey, P. and Willam, K. J. Triaxial Failure Criterion for Concrete and its Generalization. ACI Structural Journal, 92(3):311–318, 1995.
- [259] Merriam-Webster, Inc. Dictionary: Autogenous. Electronical, 2020. URL https://www.merriam-webster.com/dictionary/autogenous. Last access: 23.06.2020.
- [260] Meschke, G. Consideration of aging of shotcrete in the context of a 3-D viscoplastic material model. *International Journal for Numerical Methods in Engineering*, 39:3123–3143, 1996.
- [261] Meschke, G., Kropik, C., and Mang, H. A. Numerical analyses of tunnel linings by means of a viscoplastic material model for shotcrete. *International Journal for Numerical Methods* in Engineering, 39:3145–3162, 1996.
- [262] Michelis, P. N. Work-softening and hardening behaviour of granular rocks. *Rock Mechanics*, 14(3):187–200, December 1981.
- [263] Mindess, S., Young, J. F., and Lawrence, F. V. Creep and drying shrinkage of calcium silicate pastes I. Specimen preparation and mechanical properties. *Cement and Concrete Research*, 8(5):591–600, 1978.
- [264] Mitchell, T. M. and Faulkner, D. R. The nature and origin of off-fault damage surrounding strike-slip fault zones with a wide range of displacements: A field study from the Atacama fault system, northern Chile. *Journal of Structural Geology*, 31(8):802–816, August 2009.
- [265] Mödlhammer, H. *Spritzbeton: In situ Versuche*. Bachelor's thesis, Montanuniversität Leoben, Leoben, Austria, April 2008.
- [266] Monsberger, C. M., Lienhart, W., Kluckner, A., Wagner, L., and Schubert, W. Continuous strain measurements in a shotcrete tunnel lining using distributed fibre optic sensing. In *Proceedings of the 9th European Workshop on Structural Health Monitoring*, pages 1–13, Manchester, United Kingdom, July 2018.
- [267] Monsberger, C. M., Lienhart, W., Kluckner, A., and Schubert, W. In-situ assessment of distributed strain and curvature characteristics in shotcrete tunnel linings based on fiber optic strain sensing. In *Proceedings of the 14th International Congress on Rock Mechanics* and Rock Engineering, pages 1–8, Foz do Iguassu, Brazil, September 2019.
- [268] Monsberger, C. M. and Lienhart, W. Distributed fiber optic shape sensing along shotcrete tunnel linings: Methodology, field applications, and monitoring results. *Journal of Civil Structural Health Monitoring*, 11(2):337–350, January 2021.
- [269] Monsberger, C. M., Bauer, P., Buchmayer, F., and Lienhart, W. Large-scale distributed fiber optic sensing network for short and long-term integrity monitoring of tunnel linings. *Journal of Civil Structural Health Monitoring*, 12(6):1317–1327, March 2022.
- [270] Moritz, B., Grossauer, K., and Schubert, W. Short Term Prediction of System Behaviour of Shallow Tunnels in Heterogeneous Ground. *Felsbau*, 22(5):44–52, 2004.
- [271] Müller, M. Kriechversuche an jungen Spritzbetonen zur Ermittlung der Parameter für Materialgesetze. mathesis, Montanuniversität Leoben, Leoben, Austria, October 2001.

BIBLIOGRAPHY 305 of 498

[272] Mutschler, T. Neufassung der Empfehlung Nr. 1 des Arbeitskreises "Versuchstechnik Fels" der Deutschen Gesellschaft für Geotechnik e. V.: Einaxiale Druckversuche an zylindrischen Gesteinsprüfkörpern. *Bautechnik*, 81(10):825–834, October 2004.

- [273] Naylor, M. A., Mandl, G., and Supesteijn, C. H. K. Fault geometries in basement-induced wrench faulting under different initial stress states. *Journal of Structural Geology*, 8(7): 737–752, January 1986.
- [274] Nefeslioglu, H. A. Evaluation of geo-mechanical properties of very weak and weak rock materials by using non-destructive techniques: Ultrasonic pulse velocity measurements and reflectance spectroscopy. *Engineering Geology*, 160:8–20, June 2013.
- [275] Neuner, M., Cordes, T., Drexel, M., and Hofstetter, G. Time-Dependent Material Properties of Shotcrete: Experimental and Numerical Study. *Materials*, 10(9):1067, September 2017.
- [276] Neuner, M., Gamnitzer, P., and Hofstetter, G. An Extended Damage Plasticity Model for Shotcrete: Formulation and Comparison with Other Shotcrete Models. *Materials*, 10(1): 1–22, January 2017.
- [277] Neuner, M., Schreter, M., Unteregger, D., and Hofstetter, G. Influence of the Constitutive Model for Shotcrete on the Predicted Structural Behavior of the Shotcrete Shell of a Deep Tunnel. *Materials*, 10(6):1–17, May 2017.
- [278] Neuner, M., Gamnitzer, P., and Hofstetter, G. Correction: An Extended Damage Plasticity Model for Shotcrete: Formulation and Comparison with Other Shotcrete Models. *Materials*, 11(1):135, January 2018.
- [279] Neville, A. M. Properties of Concrete. Prentice Hall, 4th edition, 1995.
- [280] Neville, A. M., Dilger, W. H., and Brooks, J. J. Creep of plain and structural concrete. Construction Press (Longman), Harlow, UK, 1983.
- [281] Nielsen, L. F. Composite creep analysis of concrete: A rational, incremental stress-strain approach. Byg Rapport R-178, Technical University of Denmark, Lyngby, Denmark, 2007.
- [282] Nilsson, M. Restraint Forces and Partial Coefficients for Crack Risk Analyses of Early Age Concrete Structures. PhD thesis, Luleå University of Technology, Luleå, Sweden, 2003.
- [283] Nübel, K. and Huang, W. A study of localized deformation pattern in granular media. Computer Methods in Applied Mechanics and Engineering, 193(27-29):2719–2743, July 2004.
- [284] Oberdörfer, W. Auswirkung von unterschiedlichen Betonnachbehandlungsmassnahmen auf die Qualit\u00e4t des Nassspritzbetons. Master's thesis, University of Innsbruck, Innsbruck, Austria, 1996.
- [285] Obert, L. and Duvall, W. I. Rock Mechanics and the Design of Structures in Rock. John Wiley & Sons, New York, 1967.
- [286] Obert, L., Windes, S. L., and Duvall, W. I. Standardized tests for determining the physical properties of mine rock. Report of Investigations 3891, United States Department of the Interior-Bureau of Mines, August 1946.

BIBLIOGRAPHY 306 of 498

[287] Obrzud, R. F. and Truty, A. The Hardening Soil Model-A practical guidebook (Z_Soil.PC 100701 report, revised 21.10.2018). Zace Services Ltd, October 2018.

- [288] ÖBV. Spritzbeton: Teil 1—Anwendung. Guideline, Österreichischer Betonverein (ÖBV), 1989.
- [289] ÖBV. Sprayed Concrete. Guideline, Österreichische Bautechnik Vereinigung (ÖBV), April 2013.
- [290] ÖGG. Guideline for the Geotechnical Design of Underground Structures with Conventional Excavation. Guideline, Austrian Society for Geomechanics (ÖGG), Salzburg, Austria, 2010. Translated from German version 2.1.
- [291] ÖGG. Geotechnical Monitoring in Conventional Tunnelling. Austrian Society for Geomechanics (ÖGG), Salzburg, Austria, 2014.
- [292] Oluokun, F. A., Burdette, E. G., and Deatherage, J. H. Splitting Tensile Strength and Compressive Strength Relationships at Early Ages. ACI Materials Journal, 88(2):115–121, 1991.
- [293] Ord, A. Deformation of rock: A pressure-sensitive, dilatant material. *Pure and Applied Geophysics (PAGEOPH)*, 137(4):337–366, 1991.
- [294] Oreste, P. P. A Procedure for Determining the Reaction Curve of Shotcrete Lining Considering Transient Conditions. Rock Mechanics and Rock Engineering, 36(3):209–236, June 2003.
- [295] Oreste, P., Spagnoli, G., and Ceravolo, L. A. A numerical model to assess the creep of shotcrete linings. Proceedings of the Institution of Civil Engineers - Geotechnical Engineering, 172(4):344–354, August 2019.
- [296] Palkovic, S. D., Brommer, D. B., Kupwade-Patil, K., Masic, A., Buehler, M. J., and
 Büyüköztürk, O. Roadmap across the mesoscale for durable and sustainable cement paste
 A bioinspired approach. Construction and Building Materials, 115:13-31, July 2016.
- [297] Palmström, A. and Singh, R. The deformation modulus of rock masses comparisons between in situ tests and indirect estimates. *Tunnelling and Underground Space Technology*, 16(2):115–131, April 2001.
- [298] Parent, T., Domede, N., Sellier, A., and Mouatt, L. Mechanical characterization of limestone from sound velocity measurement. *International Journal of Rock Mechanics and Mining* Sciences, 79:149–156, October 2015.
- [299] Passchier, C. W. and Trouw, R. A. J. Microtectonics. Springer Verlag, Berlin, 1996.
- [300] Paulini, P. Reaction mechanisms of concrete admixtures. Cement and Concrete Research, 20(6):910–918, November 1990.
- [301] Peacock, D. C. P., Dimmen, V., Rotevatn, A., and Sanderson, D. J. A broader classification of damage zones. *Journal of Structural Geology*, 102:179–192, 2017.
- [302] Pichler, B. and Hellmich, C. Hybrid methods for shotcrete and segmental linings tunnel shells Combining displacement and rotation measurements with computational multiscale mechanics. *Geomechanics and Tunnelling*, 11(3):226–235, June 2018.

BIBLIOGRAPHY 307 of 498

[303] Pichler, B., Hellmich, C., and Eberhardsteiner, J. Spherical and acicular representation of hydrates in a micromechanical model for cement paste: prediction of early-age elasticity and strength. *Acta Mechanica*, 203(3-4):137–162, June 2008.

- [304] Pichler, B., Hellmich, C., and Eberhardsteiner, J. Reaktionskinetik und Kriecheigenschaften des Spritzbetons, der im Zuge des Vortriebs des Koralmtunnels (Baulos KAT2) verwendet wird. Technical report (preliminary), Institute for Mechanics of Materials and Struttures, Vienna University of Technology, Vienna, Austria, December 2011.
- [305] Pilgerstorfer, T. Prediction of displacement development using closed form solutions. Diploma thesis, Graz University of Technology, Graz, Austria, May 2008.
- [306] Pilgerstorfer, T. Mechanical Characterization of Fault Zones. PhD thesis, Graz University of Technology, Graz, Austria, 2014.
- [307] Pilgerstorfer, T. Personal communication, January 2022.
- [308] Pilgerstorfer, T., Radončić, N., Moritz, B., and Goricki, A. Evaluation and interpretation of monitoring data in the test adit EKT Paierdorf. Geomechanics and Tunnelling, 4(5): 423–434, October 2011.
- [309] Pittino, G., Galler, R., Bonin, K., and Bezler, J. Experiences with polymer-modified shotcrete. In Amberg, F. and Knut, F. G., editors, *Proceedings of the 11th Conference on Shotcrete for Underground Support*, pages 1–18, Davos, Switzerland, June 2009. Engineering Conferences International (ECI).
- [310] Pötsch, M. The analysis of rotational and sliding modes of failure for slopes, foundations, and underground structures in blocky, hard rock. PhD thesis, Graz University of Technology, Graz, Austria, March 2011.
- [311] Potts, D. M. and Zdravković, L. Finite element analysis in geotechnical engineering: theory. Thomas Telford Ltd, London, 1999.
- [312] Poturovic, S., Schubert, W., and Blümel, M. Comparison of Constant Normal Load (CNL) and Constant Normal Stiffness (CNS) Direct Shear Tests. In Schubert, W. and Kluckner, A., editors, *Proceedings of the ISRM Regional Symposium EUROCK 2015 & 64th Geomechanics Colloquium—Future Development of Rock Mechanics*, pages 1–6, Salzburg, Austria, October 2015. Austrian Society for Geomechanics.
- [313] Powers, T. C. Causes and Control of Volume Change. *Journal of the PCA Research and Development Laboratories*, pages 30–39, January 1959. Portland Cement Association (PCA).
- [314] Powers, T. C. and Brownyard, T. L. Studies of the Physical Properties of Hardened Portland Cement Paste. In *Bulletin No. 22*, pages 1–342. Portland Cement Association (PCA), March 1948.
- [315] Probst, B. Entwicklung einer Langzeitdruckversuchsanlage für den Baustellenbetrieb zur Bestimmung des Materialverhaltens von jungem Spritzbeton. Diploma thesis, Montanuniversität Leoben, Leoben, Austria, 1999.
- [316] Pusch, R. Alteration of the Hydraulic Conductivity of Rock by Tunnel Excavation.

 International Journal of Rock Mechanics and Mining Sciences & Geomechanics Abstracts,
 26(1):79–83, January 1989.

BIBLIOGRAPHY 308 of 498

[317] Püstow, H. Tunnelling in a tectonic melange of high structural complexity. mathesis, Aachen University of Technology, Aachen, Germany, 2001.

- [318] R Core Team. R: A Language and Environment for Statistical Computing. R Foundation for Statistical Computing, Vienna, Austria, 2022. URL https://www.R-project.org/. Last access: 14.01.2023.
- [319] Radončić, N. Tunnel design and prediction of systembehaviour in weak ground. PhD thesis, Graz University of Technology, Graz, Austria, March 2011.
- [320] Rastrup, E. Heat of hydration in concrete. *Magazine of Concrete Research*, 6(17):79–92, September 1954.
- [321] Raymond, L. A. Classification of melanges. In Raymond, L. A., editor, *Melanges: Their Nature, Origin, and Significance*, pages 7–20. The Geological Society of America, 1984.
- [322] Reyes, O. and Einstein, H. H. Failure Mechanisms of Fractured Rock—A Fracture Coalescence Model. In Wittke, W., editor, *Proceedings of the 7th International ISRM Congress*, pages 333–339, Aachen, Germany, September 1991. A.A. Balkema.
- [323] Riedmüller, G. and Schubert, W. Tunnelling in Fault Zones Innovative Approaches. In Proceedings of the 4th North American Rock Mechanics Symposium (NARMS 2000): Rock Around The Rim, pages 1–12, Seattle, Washington, USA, July 2000. Balkema: Rotterdam. ARMA-2000-0113.
- [324] Riedmüller, G., Brosch, F. J., Klima, K., and Medley, E. W. Engineering Geological Characterization of Brittle Faults and Classification of Fault Rocks. *Felsbau*, 19(4):13–19, 2001.
- [325] Rokahr, R. B. and Lux, K. H. Einfluß des rheologischen Verhaltens des Spritzbetons auf den Ausbauwiderstand. *Felsbau*, 5(1):11–18, 1987.
- [326] Rombach, G. Spannbetonbau. Wiley-VCH Verlag GmbH, April 2010.
- [327] Roscoe, K. H. The Influence of Strains in Soil Mechanics. *Géotechnique*, 20(2):129–170, June 1970.
- [328] Rosso, R. S. A comparison of joint stiffness measurements in direct shear, triaxial compression, and In Situ. *International Journal of Rock Mechanics and Mining Sciences & Geomechanics Abstracts*, 13(6):167–172, June 1976.
- [329] Rostami, J., Kahraman, S., Yu, X., Copur, H., Balci, C., Bamford, W., and Asbury, B. The relation between uniaxial compressive and Brazilian tensile strength. In Ulusay, R., Aydan, O., Gercek, H., and Hindistan, M. A., editors, Proceedings of the 2016 Regional Symposium of the International Society for Rock Mechanics (EUROCK 2016)—Rock Mechanics and Rock Engineering: From the Past to the Future, volume 1, pages 147–152, Ürgüp, Cappadocia Region, Turkey, August 2016. Turkish National Society for Rock Mechanics, CRC Press.
- [330] Rowe, P. W. The stress-dilatancy relation for static equilibrium of an assembly of particles in contact. *Proceedings of the Royal Society of London. Series A. Mathematical and Physical Sciences*, 269(1339):500–527, October 1962.
- [331] Rowe, R. K., editor. Geotechnical and geoenvironmental engineering handbook. Springer US, 2001.

BIBLIOGRAPHY 309 of 498

[332] Ruetz, W. Das Kriechen des Zementsteins im Beton und seine Beeinflussung durch gleichzeitiges Schwinden. In *Deutscher Ausschuss für Stahlbeton*, number 183. Wilhelm Ernst & Sohn, Berlin, 1966.

- [333] Rust, W. Nichtlineare Finite-Elemente-Berechnungen. Springer Fachmedien Wiesbaden, 3rd edition, 2016.
- [334] Sadd, M. Elasticity. Academic Press, 3rd edition, 2014.
- [335] Sainsbury, B. L. and Sainsbury, D. P. Practical Use of the Ubiquitous-Joint Constitutive Model for the Simulation of Anisotropic Rock Masses. Rock Mechanics and Rock Engineering, 50(6):1507–1528, February 2017.
- [336] Salamon, M. D. G. Energy considerations in rock mechanics: fundamental results. *Journal of the South African Institute of Mining and Metallurgy*, 84:233–246, 1984.
- [337] Saldivar, G. G. and Sánchez, F. A. Tunnels and Underground Cities: Engineering and Innovation meet Archaeology, Architecture and Art, chapter Comparative study on shotcrete performance in tunnels based on different constitutive approaches, pages 1–10. CRC Press, 1st edition, April 2019.
- [338] Sammis, C. G. and Biegel, R. L. Fractals, fault-gouge, and friction. *Pure and Applied Geophysics PAGEOPH*, 131(1-2):255–271, 1989.
- [339] Sausgruber, T. and Brandner, R. The Relevance of Brittle Fault Zones in Tunnel Construction—Lower Inn Valley Feeder Line North of the Brenner Base Tunnel, Tyrol, Austria. *Mitteilungen der Österreichischen Geologischen Gesellschaft*, 94:157–172, August 2003.
- [340] Saw, H. A., Villaescusa, E., Windsor, C. R., and Thompson, A. G. Non-linear, elastic-plastic response of steel fibre reinforced shotcrete to uniaxial and triaxial compression testing. In Amberg, F. and Garshol, K. F., editors, *Shotcrete for Underground Support XI*, ECI Symposium Series, pages 1–18, June 2009.
- [341] SBT 1.1 Tunnel Gloggnitz: ARGE. Semmering Base Tunnel, construction lot SBT 1.1, tunnel Gloggnitz—Daily construction records. Project document (in german), Joint venture (ARGE): Implenia Österreich GmbH, HOCHTIEF Infrastructure GmbH, THYSSEN SCHACHTBAU GMBH, 2016.
- [342] SBT 1.1 Tunnel Gloggnitz: ARGE. Semmering Base Tunnel, construction lot SBT 1.1, tunnel Gloggnitz—Daily construction records. Project document (in german), Joint venture (ARGE): Implenia Österreich GmbH, HOCHTIEF Infrastructure GmbH, THYSSEN SCHACHTBAU GMBH, 2017.
- [343] SBT 1.1 Tunnel Gloggnitz: PGST. Semmering Base Tunnel, construction lot SBT 1.1, tunnel Gloggnitz—Tender documents: Geotechnical prognosis underground. Project document (in german), Austrian Federal Railways, 2014. Planungsgemeinschaft Semmering-Basistunnel neu Tunnelbau (PGST).
- [344] SBT 1.1 Tunnel Gloggnitz: site team. Semmering Base Tunnel, construction lot SBT 1.1, tunnel Gloggnitz—Presentation for the 13th meeting on the geotechnical conditions. Project document (in german), 2016.

BIBLIOGRAPHY 310 of 498

[345] SBT 1.1 Tunnel Gloggnitz: site team. Semmering Base Tunnel, construction lot SBT 1.1, tunnel Gloggnitz—Report on the site decisions on support. Project document (in german), 2016.

- [346] SBT 1.1 Tunnel Gloggnitz: site team. Semmering Base Tunnel, construction lot SBT 1.1, tunnel Gloggnitz—Report on the site decisions on support. Project document (in german), 2017.
- [347] Schädlich, B. and Schweiger, H. F. Shotcrete Model: Implementation, validation and application. Internal technical report, Graz University of Technology, Graz, Austria, October 2016.
- [348] Schädlich, B. and Schweiger, H. F. A new constitutive model for shotcrete. In Hicks, M. A., Brinkgreve, R. B. J., and Rohe, A., editors, Numerical Methods in Geotechnical Engineering Proceedings of the 8th European Conference on Numerical Methods in Geotechnical Engineering, NUMGE 2014, volume 1, pages 103–108, Delft, Netherlands, June 2014. Taylor & Francis Group, London, UK.
- [349] Schädlich, B., Schweiger, H. F., Marcher, T., and Saurer, E. Application of a novel constitutive shotcrete model to tunnelling. In *Rock Engineering and Rock Mechanics:* Structures in and on Rock Masses, pages 799–804. CRC Press, May 2014.
- [350] Schanz, T., Vermeer, P. A., and Bonnier, P. G. The hardening soil model: Formulation and verification. In *Proceedings of the 1st PLAXIS symposium: Beyond 2000 in Computational Geotechnics-10 Years of PLAXIS*, pages 1–16. Balkema: Rotterdam, 1999.
- [351] Scheiner, S. and Hellmich, C. Continuum Microviscoelasticity Model for Aging Basic Creep of Early-Age Concrete. *Journal of Engineering Mechanics*, 135(4):307–323, April 2009.
- [352] Scheydt, J. C. Influence of the reactive Components on Shotcrete Performance. *Tunnel*, (3):22–27, 2015.
- [353] Schlicke, D. Mindestbewehrung für zwangbeanspruchten Beton: Festlegung unter Berücksichtigung der erhärtungsbedingten Spannungsgeschichte und der Bauteilgeometrie. In Monographic Series TU Graz, Schriftenreihe des Instituts für Betonbau, volume 4. Verlag der Technischen Universität Graz, Graz, Austria, 2nd edition, 2016.
- [354] Schlicke, D. Personal communication, February 2018.
- [355] Schlicke, D. Personal communication, June 2020.
- [356] Schmid, S. M. and Handy, M. R. Controversies in Modern Geology. Evolution of Geological Theories in Sedimentology, Earth History and Tectonics., chapter 16. Towards a Genetic Classification of Fault Rocks: Geological Usage and Tectonophysical Implications, pages 339–361. Academic Press Limited, London, 1991.
- [357] Schön, J. H. Developments in Petroleum Science. In Physical Properties of Rocks-Fundamentals and Principles of Petrophysics, volume 65. Elsevier B.V., 2nd edition, December 2015.
- [358] Schubert, P. Beitrag zum rheologischen Verhalten von Spritzbeton. Felsbau, 6(3):150–153, 1988.

BIBLIOGRAPHY 311 of 498

[359] Schubert, P., Hölzl, H., Sellner, P., and Fasching, F. Geomechanical knowledge gained from the Paierdorf investigation tunnel in the section through the Lavanttal main fault zone. *Geomechanics and Tunnelling*, 3(2):163–173, April 2010.

- [360] Schubert, W. Erfahrungen bei der Durchörterung von Störzonen bei österreichischen Tunneln. In Proceedings of the "Nachdiplomkurs in angewandten Erdwissenschaften: Herausforderung Geologie im Untertagebau", pages 1–10, CSF Monte Veritá, Ascona, Switzerland, May 1996. ETH Zurich.
- [361] Schubert, W. Experience of tunnel construction in weak ground. Geomechanics and Tunnelling, 4(3):211–220, June 2011.
- [362] Schubert, W. and Riedmüller, G. Geotechnisches Gutachten zum Verbruch Galgenbergtunnel / Vortrieb Leoben Ost Sta. 1326 bis 1333,6. Technical report, The Austrian Federal Railways, Graz, Austria, April 1995. Unpublished.
- [363] Schubert, W. and Riedmüller, G. Geotechnische Nachlese eines Verbruches Erkenntnisse und Impulse. In Semprich, S., editor, *Proceedings of the 10th Christian Veder Colloquium: Innovation in der Geotechnik Entwicklungen der letzten Jahre*, number 13 in Mitteilungshefte, pages 59–68, Graz, Austria, 1995. Institute of Soil Mechanics and Foundation Engineering, Graz University of Technology.
- [364] Schubert, W. and Riedmüller, G. Tunnelling in Fault Zones State of the Art in Investigation and Construction. Felsbau, 18(2):7–15, 2000.
- [365] Schubert, W., Brandtner, M., Schweiger, H. F., Helmberger, A., Marcher, T., and Radončić, N. Proposed design strategy for tunnels. In Schubert, W. and Kluckner, A., editors, Proceedings of the ISRM Regional Symposium EUROCK 2015 & 64th Geomechanics Colloquium— Future Development of Rock Mechanics, pages 37–47, Salzburg, Austria, October 2015. Austrian Society for Geomechanics.
- [366] Schubert, W., Blümel, M., Brunnegger, S., Staudacher, R., and Sellner, P. J. Aspekte des Ausbaus. In Schubert, W. and Kluckner, A., editors, *Proceedings of the Workshop on Tunnelbau in Störungszonen—Eine Herausforderung*, pages 49–62, Graz, Austria, November 2016. Institute of Rock Mechanics and Tunnelling, Graz University of Technology.
- [367] Schubert, W., Blümel, M., Staudacher, R., and Brunnegger, S. Support aspects of tunnels in fault zones. *Geomechanics and Tunnelling*, 10(4):342–352, August 2017.
- [368] Schütz, R., Potts, D. M., and Zdravković, L. Advanced constitutive modelling of shotcrete: Model formulation and calibration. *Computers and Geotechnics*, 38(6):834–845, September 2011.
- [369] Schütz, R. Numerical Modelling of Shotcrete for Tunnelling. PhD thesis, Imperial College London, London, UK, February 2010.
- [370] Sercombe, J., Hellmich, C., Ulm, F.-J., and Mang, H. A. Modeling of early-age creep of shotcrete. I: Model and model parameters. *Journal of Engineering Mechanics*, 126(3): 284–291, 2000.
- [371] Sezaki, M., Kibe, T., Ichikawa, Y., and Kawamoto, T. An experimental study on the mechanical properties of shotcrete. *Journal of the Society of Materials Science*, 38(434): 1336–1340, 1989.

BIBLIOGRAPHY 312 of 498

[372] Sibson, R. H. Fault rocks and fault mechanisms. *Journal of the Geological Society*, 133(3): 191–213, March 1977.

- [373] Sibson, R. H. Structural permeability of fluid-driven fault-fracture meshes. *Journal of Structural Geology*, 18(8):1031–1042, August 1996.
- [374] Simo, J. C., Kennedy, J. G., and Govindjee, S. Non-smooth multisurface plasticity and viscoplasticity. Loading/unloading conditions and numerical algorithms. *International Journal for Numerical Methods in Engineering*, 26(10):2161–2185, October 1988.
- [375] Skempton, A. W. Residual strength of clays in landslides, folded strata and the laboratory. *Géotechnique*, 35(1):3–18, March 1985.
- [376] Sönmez, H., Gokceoglu, C., Tuncay, E., Medley, E. W., and Nefeslioglu, H. A. Relationships between Volumetric Block Proportions and Overall UCS of a Volcanic Bimrock. *Felsbau*, 22(5):27–34, 2004.
- [377] Sönmez, H., Tuncay, E., and Gokceoglu, C. Models to predict the uniaxial compressive strength and the modulus of elasticity for Ankara Agglomerate. *International Journal of Rock Mechanics and Mining Sciences*, 41(5):717–729, July 2004.
- [378] Sönmez, H., Gokceoglu, C., Medley, E. W., Tuncay, E., and Nefeslioglu, H. A. Estimating the uniaxial compressive strength of a volcanic bimrock. *International Journal of Rock Mechanics and Mining Sciences*, 43(4):554–561, June 2006.
- [379] Sönmez, H., Kasapoglu, K. E., Coskun, A., Tunusluoglu, C., Medley, E. W., and Zimmerman, R. W. A conceptual empirical approach for the overall strength of unwelded bimrocks. In Vrkljan, I., editor, Proceedings of the 2009 Regional Symposium of the International Society for Rock Mechanics (EUROCK 2009)—Rock Engineering in Difficult Ground Conditions Soft Rocks and Karst, pages 357–360, Dubrovnik, Croatia, October 2010. Taylor & Francis: London.
- [380] Stadlmann, T., Vanek, R., and Goricki, A. Semmering Base Tunnel, construction lot SBT 1.1, tunnel Gloggnitz—Tender documents: Rock mass types. Project document (in german), Austrian Federal Railways, 2014.
- [381] Staudacher, R. F. Anschlüsse für Arbeitsfugen bei Spritzbetonauskleidungen. Master's thesis, Graz University of Technology, Graz, Austria, November 2016.
- [382] Steindorfer, A. F. Short Term Prediction of Rock Mass Behaviour in Tunnelling by Advanced Analysis of Displacement Monitoring Data. PhD thesis, Graz University of Technology, Graz, Austria, November 1997.
- [383] Stini, J. Tunnelbaugeologie Die geologischen Grundlagen des Stollen- und Tunnelbaues. Springer Vienna, 1st edition, 1950.
- [384] Swanson, M. T. Late Paleozoic strike-slip faults and related vein arrays of Cape Elizabeth, Maine. *Journal of Structural Geology*, 28(3):456–473, March 2006.
- [385] Tazawa, E.-i., editor. Autogenous Shrinkage of Concrete: Proceedings of the International Workshop, organized by the JCI (Japan Concrete Institute), Hiroshima, Japan, June 1999. Taylor & Francis.
- [386] Terzaghi, K. Theoretical Soil Mechanics. John Wiley & Sons, Inc.: New York, 1943.

BIBLIOGRAPHY 313 of 498

[387] Thomas, A. Numerical modelling of sprayed concrete lined (SCL) tunnels. PhD thesis, University of Southampton, Southampton, United Kingdom, 2003.

- [388] Thomas, A. Sprayed Concrete Lined Tunnels—An introduction. Taylor & Francis, 2009.
- [389] Thomas, A. Sprayed Concrete Lined Tunnels—second edition. CRC Press, 2020.
- [390] Thomée, B. *Physikalisch nichtlineare Berechnung von Stahlfaserbetonkonstruktionen*. PhD thesis, Technical University Munich, Munich, Germany, 2005.
- [391] Thornton, C. Numerical simulations of deviatoric shear deformation of granular media. *Géotechnique*, 50(1):43–53, February 2000.
- [392] Thuro, K., Plinninger, R. J., Zäh, S., and Schütz, S. Scale effects in rock strength properties. Part 1: Unconfined compressive test and Brazilian test. In Särkkä and Eloranta, editors, Proceedings of the 2001 Regional Symposium of the International Society for Rock Mechanics (EUROCK 2001)—Rock Mechanics A Challenge for Society, pages 169–174. Swets & Zeitlinger Lisse, 2001.
- [393] Tigges, V. E. Die Hydratation von Hüttensanden und Möglichkeiten ihrer Beeinflussung zur Optimierung von Hochofenzementeigenschaften. PhD thesis, Clausthal University of Technology, Clausthal-Zellerfeld, Germany, 2009.
- [394] Tourenq, C. and Denis, A. La resistance a la traction des roches. Rapport de Recherches 4A, Laboratoire Central des Ponts et Chaussées, Paris, France, 1970.
- [395] Traina, L. A. Experimental stress-strain behaviour of a low strength concrete under multiaxial states of stress. Technical report AFWL-TR-82-92, Air Force Weapons Laboratory, Kirtland Air Force Base, New Mexico, USA, 1983.
- [396] Tsesarsky, M., Hazan, M., and Gal, E. Estimating the elastic moduli and isotropy of block in matrix (bim) rocks by computational homogenization. *Engineering Geology*, 200:58–65, January 2016.
- [397] Twiss, R. J. and Moores, E. M. Structural Geology. W. H. Freeman and Company, New York, USA, 2nd edition, 2007.
- [398] Tziallas, G. P., Tsiambaos, G., and Saroglou, H. Determination of Rock Strength and Deformability of Intact Rocks. *Electronic Journal of Geotechnical Engineering (EJGE)*, 14 (G):1–12, 2009.
- [399] Ulm, F.-J. Couplages thermochémomécaniques dans les bétons: Un premier bilan. Monograph LCPC OA31, Laboratoire Central des Ponts et Chaussées, Paris, France, 1998.
- [400] Ulm, F.-J. and Acker, P. Le point sur le fluage et la recouvrance des bétons. *Bulletin Liaison des Laboratoires des Ponts et Chaussées*, (XX):73–82, 1998. Special issue.
- [401] Ulm, F.-J. and Coussy, O. Modeling of Thermochemomechanical Couplings of Concrete at Early Ages. *Journal of Engineering Mechanics*, 121(7):785–794, 1995.
- [402] Ulm, F.-J. and Coussy, O. Strength Growth as Chemo-Plastic Hardening in Early Age Concrete. *Journal of Engineering Mechanics*, 122(12):1123–1132, 1996.

BIBLIOGRAPHY 314 of 498

[403] Ulusay, R., Türeli, K., and Ider, M. H. Prediction of engineering properties of a selected litharenite sandstone from its petrographic characteristics using correlation and multivariate statistical techniques. *Engineering Geology*, 38(1-2):135–157, December 1994.

- [404] U.S. Department of the Interior Bureau of Reclamation. *Engineering geology field manual*, volume I. U.S. Government Printing Office, 2nd edition, 1998.
- [405] U.S. Department of the Interior Bureau of Reclamation. Glossary of commonly used terms by the Bureau of Reclamation. Electronical, 2016. URL https://www.usbr.gov/library/glossary/index.html. Last access: 20.12.2016.
- [406] van der Pluijm, B. A. and Marshak, S. Earth structure: an introduction to structural geology and tectonics. W. W. Norton & Company, Inc.: New York, 2nd edition, 2004.
- [407] Vanek, R. and Stadlmann, T. Semmering Base Tunnel new—Legal railway approval procedure documents: Report on the construction geology. Project document (in german), Austrian Federal Railways, May 2010.
- [408] Vanek, R., Fasching, F., and Fasching, A. Ingenieurgeologische Charakterisierung von Störungszonen. In Schubert, W. and Kluckner, A., editors, *Proceedings of the Workshop on Tunnelbau in Störungszonen—Eine Herausforderung*, pages 1–11, Graz, Austria, November 2016. Institute of Rock Mechanics and Tunnelling, Graz University of Technology.
- [409] VBE. Semmering Base Tunnel, construction lot SBT 1.1, tunnel Gloggnitz—Concrete test report. Project document (in german), Verein für Baustoffprüfung und -entwicklung (VBE), 2016.
- [410] Vermeer, P. A. and de Borst, R. Non-associated plasticity for soils, concrete and rock. HERON, 29(3):1–64, 1984.
- [411] Vlachopoulos, N. and Diederichs, M. S. Improved Longitudinal Displacement Profiles for Convergence Confinement Analysis of Deep Tunnels. Rock Mechanics and Rock Engineering, 42(2):131–146, April 2009.
- [412] Volpe, R., Ahlgren, C., and Goodman, R. Selection of engineering properties for geologically variable foundations. In *Proceedings of the 17th International Congress on Large Dams*, *Vienna:Paris*, pages 1087–1101. International Commission on Large Dams, 1991.
- [413] von Rabcewicz, L. Die Ankerung im Tunnelbau ersetzt bisher gebräuchliche Einbaumethoden. Schweizerische Bauzeitung, 75(9):123–131, March 1957.
- [414] von Terzaghi, K. *Ingenieurgeologie*, chapter Tunnelgeologie, pages 365–407. Julius Springer: Vienna, 1st edition, 1929.
- [415] Wagner, L. Concept and realisation of a distributed fibre-optic sensing system for direct and continuous strain measurement in a shotcrete lining. Master's thesis, Graz University of Technology, Graz, Austria, September 2017.
- [416] Wagner, L., Kluckner, A., Monsberger, C. M., Wolf, P., Prall, K., Schubert, W., and Lienhart, W. Direct and Distributed Strain Measurements Inside a Shotcrete Lining: Concept and Realisation. *Rock Mechanics and Rock Engineering*, 53(2):641–652, August 2019.

BIBLIOGRAPHY 315 of 498

[417] Wen-jie, X., Zhong-qi, Y., and Rui-lin, H. Study on the mesostructure and mesomechanical characteristics of the soil—rock mixture using digital image processing based finite element method. *International Journal of Rock Mechanics and Mining Sciences*, 45(5):749–762, July 2008.

- [418] Wen-Jie, X., Qiang, X., and Rui-Lin, H. Study on the shear strength of soil—rock mixture by large scale direct shear test. *International Journal of Rock Mechanics and Mining Sciences*, 48(8):1235–1247, December 2011.
- [419] Wesche, K. Baustoffe für tragende Bauteile—Band 2: Beton, Mauerwerk. Bauverlag GmbH: Wiesbaden, Berlin, 3rd edition, 1993.
- [420] Wibberley, C. A. J., Yielding, G., and Toro, G. D. Recent advances in the understanding of fault zone internal structure: a review. *Geological Society, London, Special Publications*, 299(1):5–33, 2008.
- [421] Wittmann, F. Bestimmung physikalischer Eigenschaften des Zementsteins. In *Deutscher Ausschuss für Stahlbeton*, number 232. Wilhelm Ernst & Sohn, Berlin, 1974.
- [422] Wuilpart, M. Advanced Fiber Optics: Concepts and Technology, chapter Rayleigh scattering in optical fibers and applications to distributed measurements, pages 1–56. EPFL Press, Lausanne, Switzerland, 1st edition, 2011.
- [423] Wullschläger, D. Ein Verbundwerkstoffmodell für die Systemankerung im Tunnelbau. PhD thesis, Universität Karlsruhe, Karlsruhe, Germany, 1988.
- [424] Yin, J. Untersuchungen zum zeitabhängigen Tragverhalten von tiefliegenden Hohlräumen im Fels mit Spritzbetonausbau. PhD thesis, Technische Universität Clausthal, Clausthal-Zellerfeld, Germany, February 1996.
- [425] ZAMG. Zentralanstalt für Meteorologie und Geodynamik: Klimamonitoring. Electronical, 2021. URL https://www.zamg.ac.at/cms/de/klima/klima-aktuell/klimamonitoring/?view=fullscreen¶m=t&period=period-ymd-2016-11-17&ref=3. Last access: 02.12.2021.
- [426] Zhang, H.-Y., Xu, W.-J., and Yu, Y.-Z. Triaxial tests of soil—rock mixtures with different rock block distributions. *Soils and Foundations*, 56(1):44–56, February 2016.
- [427] Zhao, X. G. and Cai, M. A mobilized dilation angle model for rocks. *International Journal of Rock Mechanics and Mining Sciences*, 47(3):368–384, April 2010.
- [428] Zi, G. and Bažant, Z. P. Continuous Relaxation Spectrum for Concrete Creep and its Incorporation into Microplane Model M4. *Journal of Engineering Mechanics*, 128(12): 1331–1336, December 2002.

Appendix D: Fibre optic monitoring section: Data evaluation

The following paragraph and figures verify the positioning of the DFOS cables (cf. Fig 8.6 on p. 181 in the main part of this thesis).

Fig. D.1 and Fig. D.2 show the strain in the circumferential direction (i.e., perpendicular to the tunnel axis) of cable segments that are very close to each other. The graphs plot the strain for four distinct moments after the reference measurement. Because the cable segments are next to each other within the shotcrete lining, the strain values must be similar. They are for most parts of the cable segments. Thus, it is assumed that the alignment of the cables shown in Fig. 8.6 (p. 181) is close to being correct. The largest differences exist at ends of cable segments aligned in the circumferential direction. There, cables are often fixed to the wire mesh and the cables 'long' and 'long2' are bent to align in the longitudinal direction (i.e., parallel to the tunnel axis).

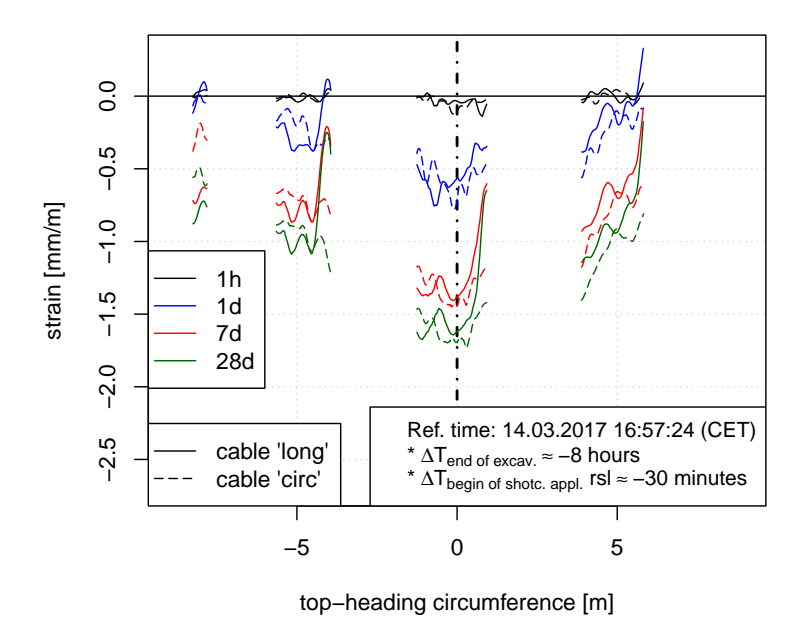


Figure D.1: DFOS section | top heading | rock-side layer (rsl): Comparison of the strain in the circumferential direction of DFOS cable segments which align next to each other (cf. left developed top view in Fig. 8.6 on p. 181).

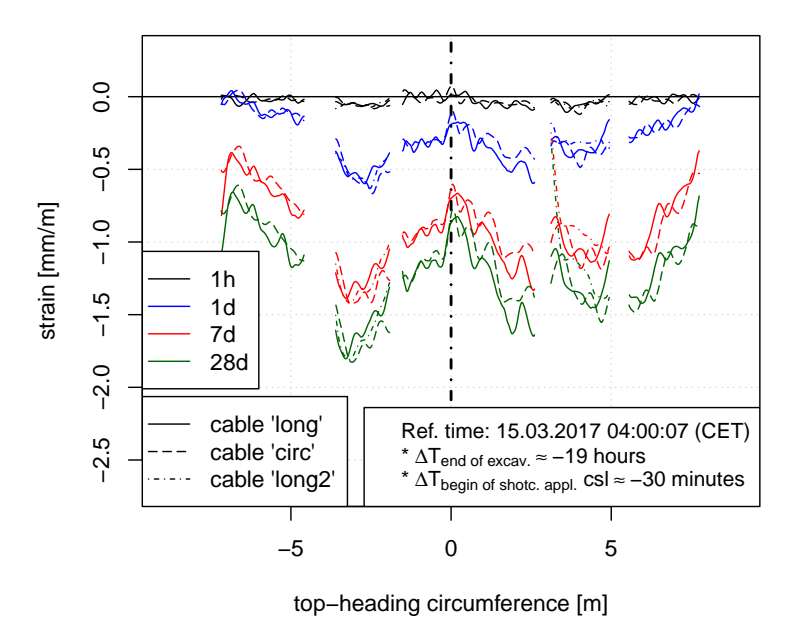


Figure D.2: DFOS section | top heading | cavity-side layer (csl): Comparison of the strain in the circumferential direction of DFOS cable segments which align next to each other (cf. right developed top view in Fig. 8.6 on p. 181).